

1-1-2010

# Cyclic Deformation of Semi-solid Processed Magnesium Alloys

Himesh Patel  
*Ryerson University*

Follow this and additional works at: <http://digitalcommons.ryerson.ca/dissertations>

 Part of the [Mechanical Engineering Commons](#)

---

## Recommended Citation

Patel, Himesh, "Cyclic Deformation of Semi-solid Processed Magnesium Alloys" (2010). *Theses and dissertations*. Paper 1471.

This Thesis is brought to you for free and open access by Digital Commons @ Ryerson. It has been accepted for inclusion in Theses and dissertations by an authorized administrator of Digital Commons @ Ryerson. For more information, please contact [bcameron@ryerson.ca](mailto:bcameron@ryerson.ca).

# **CYCLIC DEFORMATION OF SEMI-SOLID PROCESSED MAGNESIUM ALLOYS**

By

**HIMESH PATEL**

Bachelor of Engineering (Mechanical)

Sardar Vallabhbhai National Institute of Technology (SVNIT), Surat, India, 2006

A thesis

presented to Ryerson University

in partial fulfillment of the

requirements for the degree of

Master of Applied Science

in the Program of

Mechanical Engineering

Toronto, Ontario, Canada, 2010

© Himesh Patel 2010

## **AUTHOR'S DECLARATION**

I hereby declare that I am the sole author of this thesis.

I authorize Ryerson University to lend this thesis to other institution or other individuals for the purpose of scholarly research.

Himesh Patel: \_\_\_\_\_

I further authorize Ryerson University to reproduce this thesis by photocopying or by other means, in total or in part, at the request of other institutions or individuals for the purpose of scholarly research.

Himesh Patel: \_\_\_\_\_

## **BORROWER'S PAGE**

Ryerson University requires the signature of all persons using or photocopying this thesis.

Please sign below provide address and date.

Name	Signature	Address	Date

# **CYCLIC DEFORMATION OF SEMI-SOLID PROCESSED MAGNESIUM ALLOYS**

© Himesh Patel, 2010

Master of Applied Science

Department of Mechanical Engineering

Ryerson University

## **ABSTRACT**

To improve fuel economy and reduce greenhouse gas emissions, magnesium alloys are being considered for automotive and aerospace applications because of their high strength-to-weight ratio. The objective of this thesis was to study monotonic and cyclic deformation behavior of two semi-solid processed (thixomolded) magnesium alloys, AZ91D and AM60B. The fatigue life of these thixomolded alloys was observed to be higher than that of their die cast counterparts. As the total strain amplitude increased, the stress amplitude and plastic strain amplitude increased, while the pseudoelastic modulus decreased. The change in the modulus was attributed to the nonlinear (pseudoelastic) behavior caused by twinning-detwinning during cyclic deformation. The fatigue life increased with decreasing strain ratio, and partial mean stress relaxation occurred mainly in the initial 10-20% of the fatigue life. The fatigue life of the AM60B alloy improved after solution or solution-aging treatment, and the monotonic strength increased by aging, while the thixomolded condition itself exhibited moderate monotonic strength and fatigue life.

## **ACKNOWLEDGEMENTS**

I would like to thank my supervisors Dr. D.L. Chen and Dr. S.D. Bhole for their guidance, support and encouragement during my studies at Ryerson University. I would also like to thank Dr. K. Sadayappan from CANMET-Materials Technology Laboratory, Natural Resources, Ottawa, Ontario, Canada for his helpful discussion.

I would also like to thank the Natural Sciences and Engineering Research Council of Canada (NSERC) and AUTO21 for providing financial support. This investigation involves part of the Canada-China-USA Collaborative Research Project on the Magnesium Front End Research and Development (MFERD), and financial support from CANMET-MTL is also acknowledged.

I would like to extend my thanks to all my friends and colleagues at Ryerson University for helping me and keeping my spirits up. Special thanks are owed to A. Machin, J. Amankrah, Q. Li and R. Churaman for their strong support in providing easy access to the facilities.

Words cannot express my deepest gratitude towards my parents and towards my siblings. Last but not least, I would also like to thank my loving wife for her persistent encouragement, emotional support, and great patience during my graduate study.

*To*

*My wife Ruchika, and our daughter Jiya*

# TABLE OF CONTENTS

AUTHOR’S DECLARATION.....	ii
BORROWER’S PAGE.....	iii
ABSTRACT.....	iv
ACKNOWLEDGEMENTS.....	v
TABLE OF CONTENTS.....	vii
LIST OF TABLES.....	xi
LIST OF FIGURES.....	xii
NOMENCLATURE.....	xix
<b>CHAPTER 1: INTRODUCTION.....</b>	<b>1</b>
<b>CHAPTER 2: LITERATURE SURVEY.....</b>	<b>4</b>
<b>2.1 Trend of Research and Development for Magnesium Alloys .....</b>	<b>4</b>
<b>2.2 Process Improvements in Cast Magnesium Alloys.....</b>	<b>5</b>
<b>2.2.1 Thixomolding.....</b>	<b>6</b>
<b>2.3 Heat Treatment.....</b>	<b>9</b>
<b>2.4 Mechanical Properties.....</b>	<b>10</b>
<b>2.4.1 Tensile properties.....</b>	<b>10</b>
<b>2.4.2 Fatigue behavior.....</b>	<b>11</b>
<b>2.4.2.1 Stress-controlled high cycle fatigue .....</b>	<b>13</b>
<b>2.4.2.2 Strain-controlled low cycle fatigue.....</b>	<b>15</b>



(a) Cyclic stress-strain curve.....	17
(b) Fatigue life and strain-life equation.....	18
(c) Fatigue fracture surface.....	21
<b>2.5 Problem Statement and Objectives.....</b>	<b>23</b>
 <b>CHAPTER 3: EXPERIMENTAL PROCEDURE.....</b>	 <b>24</b>
<b>3.1 Materials and Composition.....</b>	<b>24</b>
<b>3.2 Heat Treatment.....</b>	<b>25</b>
<b>3.3 Sample Preparation and Testing.....</b>	<b>26</b>
3.3.1 <i>Metallography</i> .....	26
3.3.2 <i>Quantitative image analysis</i> .....	27
3.3.3 <i>Hardness tests</i> .....	28
3.3.4 <i>Tensile tests</i> .....	28
3.3.5 <i>Fatigue tests</i> .....	29
 <b>CHAPTER 4: MECHANICAL PROPERTIES OF SEMI-SOLID                 PROCESSED MAGNESIUM ALLOYS .....</b>	 <b>31</b>
<b>4.1 Microstructure.....</b>	<b>31</b>
<b>4.2 Tensile Properties.....</b>	<b>36</b>
4.2.1 <i>Comparing tensile properties</i> .....	37
4.2.2 <i>Strain hardening and strain-rate sensitivity</i> .....	39
<b>4.3 Role of twinning in Strain Hardening .....</b>	<b>42</b>
<b>4.4 Tensile Fracture Surfaces.....</b>	<b>43</b>

<b>CHAPTER 5: CYCLIC DEFORMATION AND TWINNING IN SEMI-SOLID PROCESSED MAGNESIUM ALLOYS.....</b>	<b>47</b>
5.1 Cyclic Deformation Response.....	47
5.2 Hysteresis Loops.....	51
5.3 Change of Elastic Modulus during Cyclic Deformation.....	53
5.4 Pseudoelasticity.....	55
5.5 Fatigue Life and LCF Parameters.....	56
5.6 Effect of Strain Ratio.....	62
5.6.1 Effect on stress amplitudes.....	63
5.6.2 Effect on mean stress.....	64
5.6.3 Effect on hysteresis loops.....	65
5.7 Fractography.....	67
5.8 Formation of Twins during Fatigue.....	73
5.9 Comparison of Thixomolded and Extruded Mg Alloys.....	76
 <b>CHAPTER 6: EFFECT OF HEAT TREATMENT ON THE MECHANICAL BEHAVIOR OF SEMI-SOLID PROCESSED AM60B ALLOY.....</b>	 <b>79</b>
6.1 Effect of Heat Treatment on Microstructure.....	79
6.2 Effect of Heat Treatment on Tensile Properties.....	84
6.3 Effect of Heat Treatment on Fatigue Behavior.....	87
6.4 Summary on the Effect of Heat Treatment.....	93

<b>CHAPTER 7: SUMMARY, CONCLUSIONS AND FUTURE WORK.....</b>	<b>95</b>
<b>7.1 Summary and Conclusions.....</b>	<b>95</b>
<b>7.2 Recommendations for Future Work.....</b>	<b>99</b>
 <b>REFERENCES .....</b>	<b>101</b>

## LIST OF TABLES

<i>Table 2.1 Strain-controlled fatigue parameters obtained for various AZ91 alloy in different processing conditions .....</i>	<i>20</i>
<i>Table 3.1 Chemical composition (in wt%) of thixomolded AZ91D and AM60B .....</i>	<i>24</i>
<i>Table 4.1 Volume fraction of solid primary <math>\alpha</math>-Mg phase, porosity, and microhardness values in both thixomolded Mg alloys AZ91D and AM60B .....</i>	<i>32</i>
<i>Table 5.1 Strain-controlled fatigue parameters obtained for the present thixomolded Mg alloys AZ91D and AM60B .....</i>	<i>61</i>
<i>Table 6.1 Tensile properties for the heat treated and thixomolded AM60B alloy tested at a strain rate of <math>1 \times 10^{-3} \text{ s}^{-1}</math> at room temperature.....</i>	<i>85</i>
<i>Table 6.2 Fatigue parameters obtained from fully reversed strain-controlled tests for the heat treated and thixomolded AM60B samples.....</i>	<i>92</i>

## LIST OF FIGURES

<i>Figure 2.1</i>	<i>(a) Schematic of thixomolding machine, (b) typical alloy (AZ91) composition and associated temperature range, shown in the Mg-Al phase diagram for the thixomolding process, and (c) dendritic and globular grain formation of Mg alloy [40] .....</i>	<i>7</i>
<i>Figure 2.2</i>	<i>Fatigue data of (a) AZ91, and (b) AM60 produced by high-pressure die-casting. Solid circles refer to failure after surface or near surface crack initiation, and open circles indicate failure by cracks starting in the interior of the material. Open triangles refer to fatigue data of similar material tested at 50 Hz [20] .....</i>	<i>14</i>
<i>Figure 2.3</i>	<i>Stress-strain loop for constant strain cycling [66] .....</i>	<i>17</i>
<i>Figure 2.4</i>	<i>Fatigue life data of plastic, elastic, and total strain amplitudes vs. the number of reversals to failure [35].....</i>	<i>20</i>
<i>Figure 2.5</i>	<i>SEM images of fatigue fracture surface in a die cast AZ91E-T4 Mg alloy: (a) overall view, (b) crack formation site, (c) Region 1, (d) Region 2, and (e) Region 3 [33].....</i>	<i>22</i>
<i>Figure 3.1</i>	<i>Thixomolded plate used in the present investigation .....</i>	<i>24</i>
<i>Figure 3.2</i>	<i>Heat treatment procedure for the thixomolded AM60B alloy .....</i>	<i>26</i>
<i>Figure 3.3</i>	<i>Geometry of the sub-sized tensile test specimen according to ASTM E8M .....</i>	<i>29</i>

<i>Figure 3.4</i>	<i>Geometry of the sub-sized fatigue test specimen .....</i>	<i>30</i>
<i>Figure 4.1</i>	<i>Optical microscope images showing the microstructure of thixomolded magnesium alloy (a) AZ91D and (b) AM60B .....</i>	<i>31</i>
<i>Figure 4.2</i>	<i>EDS line scan across the eutectic structure in the thixomolded AZ91D alloy, (a) overall view, and (b) magnified view of the compositional variation .....</i>	<i>33</i>
<i>Figure 4.3</i>	<i>EDS point analysis in the AZ91D alloy, (a) SEM image showing the locations for the analysis, (b) EDS spectrum for an Al-Mn rich particle (spectrum 1 in (a)), (c) EDS spectrum for a primary <math>\alpha</math>-Mg grain (spectrum 2 in (a)), and (d) EDS spectrum for the eutectic structure containing intermetallic compound (spectrum 3 in (a)).....</i>	<i>34</i>
<i>Figure 4.4</i>	<i>EDS line scan across an Al-Mn particle in the thixomolded AM60B alloy, (a) overall view, and (b) magnified view of the compositional variation .....</i>	<i>35</i>
<i>Figure 4.5</i>	<i>EDS point analysis in the AM60B alloy, (a) SEM image showing the locations for the analysis, (b) EDS spectrum for an Al-Mn rich particle (spectrum 1 in (a)), (c) EDS spectrum for a primary <math>\alpha</math>-Mg matrix (spectrum 2 in (a)), and (d) EDS spectrum for the eutectic structure containing intermetallic compound (spectrum 3 in (a)).....</i>	<i>36</i>
<i>Figure 4.6</i>	<i>Typical engineering stress-strain curves obtained at different strain rates for thixomolded AZ91D and AM60B alloys.....</i>	<i>37</i>

<i>Figure 4.7 Effect of strain rate on (a) yield strength, (b) ultimate tensile strength, (c) % elongation, and (d) strain hardening exponent for thixomolded AZ91D and AM60B alloys.....</i>	<i>39</i>
<i>Figure 4.8 Strain hardening rate (<math>\theta</math>) as a function of true stress (<math>\sigma</math>) at varying strain rates for thixomolded AZ91D and AM60B alloys.....</i>	<i>41</i>
<i>Figure 4.9 Typical SEM images showing the occurrence of twinning near the fracture surface of thixomolded alloys (a) AZ91D and (b) AM60B.....</i>	<i>43</i>
<i>Figure 4.10 Typical SEM images showing the fracture surfaces of tensile tested (a) AZ91D alloy, (b) magnified view of the boxed region in (a), (c) AM60B alloy, and (d) magnified view of the boxed region in (c) .....</i>	<i>44</i>
<i>Figure 4.11 Typical SEM images showing the side surface of tensile tested (a) AZ91D alloy, and (b) AM60B alloy .....</i>	<i>46</i>
<i>Figure 5.1 Variation of (a) stress amplitude, and (b) plastic strain amplitude with the number of cycles at different total strain amplitudes for thixomolded AZ91D alloy .....</i>	<i>48</i>
<i>Figure 5.2 Variation of (a) stress amplitude, and (b) plastic strain amplitude with the number of cycles at different total strain amplitudes for thixomolded AM60B alloy.....</i>	<i>49</i>
<i>Figure 5.3 Typical hysteresis loops of the first and mid-life cycles at total strain amplitude of 1.2% for thixomolded Mg alloy (a) AZ91D and (b) AM60B .....</i>	<i>51</i>

<i>Figure 5.4</i>	<i>Typical hysteresis loops of the mid-life cycles at different total strain amplitudes for thixomolded Mg alloy (a) AZ91D and (b) AM60B .....</i>	<i>52</i>
<i>Figure 5.5</i>	<i>Variation of (a) loading modulus, and (b) unloading modulus with the number of cycles during cyclic deformation at different strain amplitudes for thixomolded AZ91D alloy .....</i>	<i>54</i>
<i>Figure 5.6</i>	<i>Variation of (a) loading modulus, and (b) unloading modulus with the number of cycles during cyclic deformation at different strain amplitudes for thixomolded AM60B alloy .....</i>	<i>55</i>
<i>Figure 5.7</i>	<i>Fatigue lifetime in comparison with that of die cast Mg alloys reported in the literature for the thixomolded Mg alloys (a) AZ91D and (b) AM60B.....</i>	<i>57</i>
<i>Figure 5.8</i>	<i>Various strain amplitudes vs. number of reversals to failure (a) thixomolded AZ91D alloy in comparison with that of vacuum die cast AZ91 alloy reported in [28], and (b) thixomolded AM60B alloy .....</i>	<i>60</i>
<i>Figure 5.9</i>	<i>Fatigue lifetime for the semi-solid thixomolded AZ91D and AM60B alloys .....</i>	<i>61</i>
<i>Figure 5.10</i>	<i>Number of cycles to failure vs. strain ratio for the thixomolded AZ91D and AM60B alloys tested at a total strain amplitude of 0.6% and strain rate of <math>1 \times 10^{-2} \text{ s}^{-1}</math> .....</i>	<i>62</i>



<i>Figure 5.11 Stress amplitude vs. number of cycles for thixomolded alloy (a) AZ91D and (b) AM60B, tested at a total strain amplitude of 0.6% and strain rate of <math>1 \times 10^{-2} \text{ s}^{-1}</math> .....</i>	<i>63</i>
<i>Figure 5.12 Mean stress vs. a normalized cycle ratio (<math>N/N_f</math>) at different strain ratios for thixomolded alloy (a) AZ91D and (b) AM60B, tested at total strain amplitude of 0.6% and strain rate of <math>1 \times 10^{-2} \text{ s}^{-1}</math> .....</i>	<i>65</i>
<i>Figure 5.13 First cycle hysteresis loops at different strain ratios for thixomolded alloys (a) AZ91D and (b) AM60B, tested at total strain amplitude of 0.6% and strain rate of <math>1 \times 10^{-2} \text{ s}^{-1}</math> .....</i>	<i>66</i>
<i>Figure 5.14 Mid-life hysteresis loops at different strain ratios for thixomolded alloys (a) AZ91D and (b) AM60B, tested at total strain amplitude of 0.6% and strain rate of <math>1 \times 10^{-2} \text{ s}^{-1}</math> .....</i>	<i>67</i>
<i>Figure 5.15 Typical SEM images showing the fatigue fracture surface of thixomolded AZ91D alloy obtained at a total strain amplitude of 0.3%; (a) overall view at a low magnification, (b) magnified view near the initiation site as marked in (a), (c) magnified view in the crack propagation area as marked in (a), and (d) further magnified view in the crack propagation area as marked in (a) .....</i>	<i>68</i>
<i>Figure 5.16 Typical SEM images showing fatigue fracture surfaces of thixomolded AM60B alloy; (a) overall view and (b) magnified view of the boxed region in (a) at a total strain amplitude of 0.3%, (c) overall view and</i>	

(d) magnified view of the boxed region in (c) at a total strain amplitude of 0.6% .....	70
---	----

Figure 5.17 Typical micrographs showing the side view near the fatigue fracture surface: (a) SEM image showing an Al-Mn particle acting as a barrier to the secondary crack propagation, (b) OM image showing a secondary crack propagating mainly along $\alpha$ - $\beta$ interfaces, (c) OM image in the rapid fracture area where the eutectic structure was dislodged from the $\alpha$ grains in thixomolded AZ91D alloy, and (d) OM image showing formation of wider secondary crack near fracture surface, (e) enlarged view of the wider crack in thixomolded AM60B alloy .....	72
--	----

Figure 5.18 Twinning in thixomolded AZ91D alloy: (a) Low magnification OM image showing twins near the fracture surface, (b) SEM image of the boxed region in (a) at a higher magnification showing wide lenticular extension twins, and (c) another SEM image at a higher magnification showing narrow contraction twins marked by arrows .....	75
--	----

Figure 5.19 Optical microscope images showing (a) the formation of twins near the fracture surface, and (b) a magnified view of the area enclosed by the dashed box in (a) of thixomolded AM60B alloy.....	76
--	----

Figure 5.20 Comparing the typical hysteresis loops at mid-life of various alloys with different crystal structures and processing conditions .....	77
--	----

<i>Figure 6.1</i>	<i>Microstructures of thixomolded AM60B alloy in different conditions:</i>	
	<i>(a) Tx, (b) T4, (c) T5, and (d) T6</i>	80
<i>Figure 6.2</i>	<i>SEM images of thixomolded AM60B alloy in different conditions: (a) Tx,</i>	
	<i>(b) T4, (c) T5, and (d) T6</i>	82
<i>Figure 6.3</i>	<i>Higher magnification SEM images showing intermetallic phase of</i>	
	<i>thixomolded AM60B alloy in two different conditions: (a) Tx, and (b) T5</i>	83
<i>Figure 6.4</i>	<i>Comparison of the engineering stress-strain curves for both thixomolded</i>	
	<i>and heat treated AM60B alloy in different conditions</i>	85
<i>Figure 6.5</i>	<i>Comparison of the strain hardening rates against true stress for the</i>	
	<i>thixomolded and heat treated AM60B alloy</i>	86
<i>Figure 6.6</i>	<i>(a) Cyclic stress amplitudes and (b) plastic strain amplitudes for</i>	
	<i>thixomolded and heat treated AM60B samples tested at a total strain</i>	
	<i>amplitude of 0.6%</i>	88
<i>Figure 6.7</i>	<i>Comparison of the fatigue lifetime curves for the thixomolded and heat</i>	
	<i>treated AM60B samples</i>	90
<i>Figure 6.8</i>	<i>Comparison of the cyclic stress-strain curves for thixomolded and heat</i>	
	<i>treated AM60B alloy</i>	91

# NOMENCLATURE

Acronym	Definition
%El	% Elongation
Al	Aluminum
ASTM	American Society for Testing of Materials
bcc	Body centered cubic
Cu	Copper
EDS	Energy dispersive X-ray spectroscopy
fcc	Face centered cubic
HCF	High cycle fatigue
hcp	Hexagonal closed packed
HPDC	High pressure die cast
HV	Vickers hardness
LCF	Low cycle fatigue
LPDC	Low pressure die cast
Mg	Magnesium
Mn	Manganese
Mo	Molybdenum
RT	Room temperature
SEM	Scanning electron microscope
T4	Solution heat treated

T5	Artificially aged
T6	Solution heat treated and artificially aged
Ti	Titanium
Tx	Thixomolded
USAMP	United states automotive materials partnership
UTS	Ultimate tensile strength
V	Vanadium
YS	Yield strength
Zn	Zinc

## Symbol

## Definition

$\alpha, \beta$	Phase designations
$\sigma$	Stress, MPa
$\varepsilon$	Strain
$\dot{\varepsilon}$	Strain rate, s <sup>-1</sup>
$n$	Strain hardening exponent
$K$	Strength coefficient, MPa
$E$	Young's modulus or modulus of elasticity, MPa
$\theta$	Strain or work hardening rate, MPa
$\left( \frac{\Delta \varepsilon_t}{2} \right)$	Total strain amplitude

$\left( \frac{\Delta \varepsilon_e}{2} \right)$	Elastic strain amplitude
$\left( \frac{\Delta \varepsilon_p}{2} \right)$	Plastic strain amplitude
$N$	Number of cycles
$N_f$	Number of cycles to failure
$n'$	Cyclic strain hardening exponent
$K'$	Cyclic strength coefficient, MPa
$\sigma_f'$	Fatigue strength coefficient, MPa
$b$	Fatigue strength exponent
$\varepsilon_f'$	Fatigue ductility coefficient, %
$c$	Fatigue ductility exponent
$R$	Stress ratio
$R_\varepsilon$	Strain ratio

# **CHAPTER 1**

## **INTRODUCTION**

Weight reduction of automobiles is one of most effective methods to improve fuel efficiency and reduce Greenhouse Gas (GHG) emissions [1-4]. Magnesium (Mg), as the lightest structural metal available, is a natural choice to be used in many applications. Its use in vehicles is increasing steadily because of its favorable combination of strength-to-weight ratio, high damping capacity, as well as light weight with a density of  $1.73 \text{ g/cm}^3$  - about 30% less than aluminum, one-quarter that of steel, and nearly the same as many polymers. It is estimated that 22.5 kg of mass reduction would increase fuel efficiency by 1%; thus, automotive manufacturers worldwide have the goal to increase Mg content of automobile between 45 to 160 kg [1, 5]. But most of the applications are restricted to internal nonstructural components. The perception of limited corrosion resistance and low mechanical strength is cited as the possible reason for lack of Mg's use in structural applications. Efforts are being made to develop processes to produce high integrity components from magnesium alloys (Mg alloys).

Currently, the majority of the Mg alloys used in car body are produced by high pressure die casting (HPDC). Casting imperfections such as gas porosity and inclusions are highly common in die castings due to the turbulent mold filling, which limits their use as highly stressed body components. These cast components cannot be heat treated or welded due to the formation of blisters which reduce properties. A lot of efforts have been made to develop casting processes for Mg alloys capable of producing castings which are heat treatable,

weldable and economical [6]. The latest technology which utilizes the phenomenon of thixotropy is thixomolding®. It combines die casting with plastic injection molding and has been increasingly used for making near-net-shape components of high integrity [7]. The present effort is focused on most widely used Mg alloys AZ91D and AM60B (high purity versions of AZ91 and AM60 alloys, respectively; by putting tight limits on copper, nickel, and iron impurities for better saltwater corrosion resistance).

Previous studies involving monotonic testing of thixomolded AZ91D [7-10] and AM60B [10-12] alloys showed comparatively higher tensile properties to die casting. With lesser porosity and oxides, the microstructure of thixomolded Mg alloy typically consists of primary solid fraction of  $\alpha$ -Mg globules (average size of 30–50  $\mu\text{m}$ ) with some equiaxed secondary  $\alpha$ -Mg grains (average size of 5–10  $\mu\text{m}$ ) surrounded by eutectic mixture consisting of  $\alpha$ -Mg and  $\beta$ - $\text{Mg}_{17}\text{Al}_{12}$  intermetallics (average size of 1–2  $\mu\text{m}$ ). Strain incompatibility between the intermetallic particles (bcc) and  $\alpha$ -phase (hcp) leads to brittleness of the interface between them [13]. Thus it is important to carry out heat treatment in order to change its microstructural constituents and their effect on mechanical properties, since very limited studies have been reported about the effect of heat treatment on the microstructure and mechanical properties of thixomolded AZ91 [14-17] and AM60 [13, 18] alloys.

Typical automotive applications of Mg alloys include camshaft covers, clutch and transmission housings, and intake manifolds, which are frequently subjected to cyclic stresses and strains greater than millions of cycles during automobile operation, indicating that evaluation in this cyclic stress/strain regime is necessary in order to produce durable



vehicle components. Several studies have been conducted with stress-controlled high cycle fatigue (HCF) of AZ91 [19-21] and AM60 [21-26] alloys produced by die casting or other processes. Some strain-controlled low cycle fatigue (LCF) of die casted AZ91 [27-29] and AM60 [27, 30-32] alloys was reported as well. Other LCF behavior on the heat treated AZ91 die cast alloy was also reported in [33-36]. Limited studies on the stress-controlled high cycle fatigue of thixomolded AZ91 alloy [37, 38] and other thixomolded Mg alloys [39] indicated that the fatigue limit was significantly higher than that of the die cast counterparts. To the author's knowledge, no strain-controlled low cycle fatigue (LCF) resistance of the thixomolded AZ91D and AM60B alloys has been reported so far. The objective of the present investigation was, therefore, to identify the monotonic strain hardening and deformation behavior, the strain-controlled low cycle fatigue behavior of thixomolded AZ91D and AM60B alloys and the effect of heat treatment on the mechanical properties of the AM60B alloy.

## **CHAPTER 2**

### **LITERATURE SURVEY**

#### **2.1 Trend of Research and Development for Magnesium Alloys**

In the past, the driving force behind the development of Mg alloys was the potential for the lightweight construction in military applications. Nowadays, the emphasis has shifted for saving weight in automobile applications to meet the demand for more economic use of fuel and lower emissions in a time of growing environmental impact [40]. These needs for lightweight, energy-efficient, environment-friendly systems develop the need of structural material and motivate wider spread use of the Mg alloys. Among the widely available metallic elements that form the basis of engineering materials, Mg is the most complex from the point of view of mechanical, chemical, and physical properties. Thus, its usage has been fairly limited. Interestingly, the current driving force for expanding use of Mg-based alloys occurs in an environment where the science of material design and processing can now address its complexities and open up new possibilities [1].

Magnesium Vision 2020 of USAMP (United States Automotive Materials Partnership) proposes to reduce the weight of an average North American vehicle by 290 lbs. using 340 lbs. of Mg to replace 630 lbs. of current aluminum, iron and steel. The main technical challenges that concern US automakers to use more Mg are: higher cost with variable quality of high pressure die casting (HPDC), fastening Mg components to ferrous structures, and general as well as galvanic corrosion [5]. Various USAMP programs such as Structural Cast

Magnesium Development (SCMD) and Magnesium Powertrain Cast Component (MPCC) [41, 42] use conventional casting processes such as die casting and sand casting, while the 'Ultra Large Casting' (ULC) project is aimed at developing casting technologies to manufacture thin walled large structural components using semi-solid casting processes. Thixomolding is one of the semi-solid casting processes, and two Mg alloys produced by thixomolding have been selected for investigation in this thesis.

## **2.2 Process Improvements in Cast Magnesium Alloys**

Another main emphasis of the research and development work towards Mg alloys is their production technology. Mg alloy components can be manufactured by all conventional techniques including casting, forging, extruding, joining, rolling and molding. The choice of a method depends upon factors such as configuration of the design, application, properties required, total number of parts and castability or formability of the alloy [43]. The most common production method for Mg alloys is die-casting. Casting defects have a great influence on the mechanical properties. Impurities and enclaves need to be prevented first, because these function as crack initiation points. The reduction of the gas content and porosity will add to the positive effects. A turbulent flow in the die casting process leads to the entrapment of air pockets that leads to possible appearance of porosity. The parts lose their ductility, and heat treatment and welding become almost impossible. The efforts are made to produce high integrity casting with process improvement [40].

In recent years, alternative techniques have been commercialized to improve the overall effectiveness of net shape forming. The most distinct one is semi-solid processing where net-shape components are manufactured at temperatures between solidus and liquidus [43]. This process also offers a number of advantages compared to other processes because it reduces cast defects such as large gas pores, hot cracks, oxide inclusions, microstructure non-uniformity and chemical segregation. Dendritic morphology, typical of conventional casting processes, can be completely eliminated [44]. Thixomolding®, as a developed technology in semi-solid metal processing and a revolutionary new process has received considerable interest in recent years [7, 8, 10]. Although there are many alloys which can potentially be thixomolded, the present effort is focused on a Mg based family, mainly AZ91D and AM60B.

### ***2.2.1 Thixomolding***

Thixomolding is the injection molding of a thixotropic, semi-solid Mg alloy. The process uses an as-cast particulate feedstock, with relatively coarse particle sizes of 2-6 mm. A thixomolding machine resembles an injection molding machine in physical appearance (Figure 2.1(a)) and operating characteristics. The particulate feedstock is conveyed from a storage silo to a volumetric feeder, which automatically controls the level of material in the barrel feed throat. Argon gas, introduced into the feed throat, displaces ambient air in the system and protects the Mg alloy from high-temperature oxidation during processing [45]. The reciprocating screw conveys the Mg alloy through the controlled profile-temperature-zone barrel into the shot accumulator via a non-return valve. The establishment of a preselected temperature profile permits heating the alloy to the desired temperature between

liquidus and solidus, while the screw rotation provides mechanical mixing and shear forces, which results in the formation of the classical thixotropic structure [45]. The area of the Mg-Al phase diagram in which a thixotropic alloy (AZ91) was processed is indicated in Figure 2.1(b) with its typical temperature range for semi-solid processing. Intense stirring prevents the usual formation of dendritic grains (as in the die casting) and instead forms globular grains as shown in Figure 2.1(c).

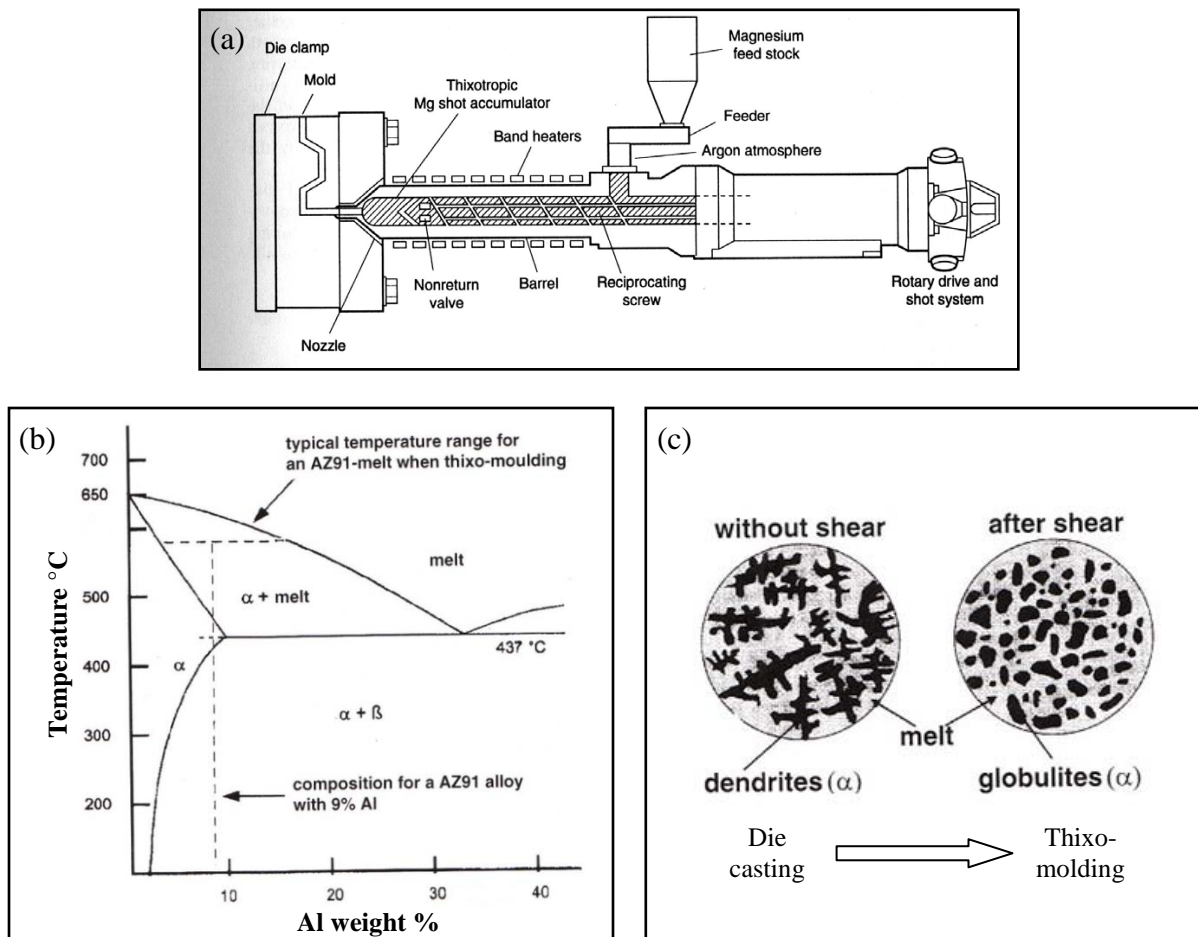


Figure 2.1: (a) Schematic of thixomolding machine, (b) typical alloy (AZ91) composition and associated temperature range, shown in the Mg-Al phase diagram for the thixomolding process, and (c) dendritic and globular grain formation of Mg alloy [40].

Care should be taken to flow argon during heating and after turning off, i.e., cooling down. This is necessary to prevent any contact with air, since the oxidation activity is high for the liquid Mg alloy [40]. Upon accumulating an appropriate thixotropic shot charge, the rotation and retraction of the screw is automatically interrupted and the screw is accelerated forward under a Programmable Logical Circuit (PLC), injecting the semi-solid processed charge into the cavity. The screw then resumes its previous action, preparing and accumulating the charge for the next shot as the die clamp is being opened and the molded part is being removed. Sustained production cycle rates of 23 s and less have been achieved, with the rate being dependent on the size of shot injected [45].

It is realized that the technique is competitive when the parts require high integrity and intricate design often combining thin and thick sections, or to eliminate machining to achieve the needed final dimensions and finishes. The benefits are associated, first, with the semi-solid state of the alloy during molding, having a high and controllable viscosity, which results in non-turbulent filling of the mold. Secondly, the molding facility is freed from having to deal with the transport of liquid metal. Then the mold design may be simplified which may allow using simpler mold materials and mold manufacturing processes. The closed processing environment provides better protection of the semi-solid alloy against oxidation; a factor for Mg alloys which are known for their high affinity to oxygen. The key advantage of this process, so far not entirely explored, is the opportunity of designing the microstructure of the final product. This factor will be of particular importance when applications of thixomolding will expand from market dominated by electronic housings to structural components of automotive industry [46, 47].

## 2.3 Heat Treatment

The structure of the thixomolded part still consists of the globules surrounded by an interglobular solid matrix that results from the rapid solidification of the liquid. This kind of structure is therefore somewhat different from that obtained by conventional casting. Owing to its hcp structure, Mg alloys exhibit generally low formability at room temperature and twinning is frequently activated during deformation. However, the effect of grain refinement on the mechanical properties, i.e., the yield stress, is more important than that for alloys with a fcc structure (like aluminium alloys) which justifies the development of thermo-mechanical treatments designed to refine the grain structure [14]. In the case of heat treatment, work has been carried out in the past on the mechanical properties at room temperature of the die cast AZ91 alloy [33-36] as well as AM60 alloy [48-50], but the effects of heat treatments on thixoformed Mg alloys and the resulting mechanical properties remain poorly documented despite some very recent studies [13-18]. Therefore, one of the aims of this work is to investigate the effect of heat treatments on the microstructure and mechanical properties of a thixomolded AM60B alloy.

Blandin *et al.* [14] studied the effect of heat treatments on the mechanical properties of a thixoformed AZ91 alloy at room and high temperature ( $T \approx 350^{\circ}\text{C}$ ). The temperatures for heat treatment were  $350^{\circ}\text{C}$  and  $415^{\circ}\text{C}$ , while various holding times (between 30 min to 96 h) were chosen for each selected temperature. Yang *et al.* [15] carried out solution treatment (T4) at  $415^{\circ}\text{C}$  for 24 h, and aging (T6) at  $216^{\circ}\text{C}$  ranging from 0 to 90 h and the microstructure was investigated by means of SEM, XRD, and Vickers hardness

measurements for thixomolded AZ91D alloy. The mechanical properties and the creep response of an AZ91 alloy produced by thixoforming [16] were investigated along with heat-treatment response at 415°C for 4 hrs (T4). Cabibbo *et al.* [17] studied various microstructures after solution treatment at 395°C, 415°C and 435°C for different times of exposure for thixocast AZ91 alloy. Mansoor *et al.* [13] carried out hot rolling, heat treatment at 400°C for 2 h, and friction stir welding on thixomolded AM60 alloy and studied the microstructure/porosity in those alloys as well as investigated possible changes in the alloy by applying severe deformation processing. Chen *et al.* [18] performed tensile and fatigue experiments at RT and 150°C on AM60 after three processing treatments: as-thixomolded, thixomolded then thermo-mechanically processed (TTMP), and thixomolded then TTMP then annealed (annealed). The TTMP procedure resulted in highest strength, the as-molded material exhibited the lowest strength, while the annealed material exhibited an intermediate strength but the highest ductility. The as-molded material exhibited the lowest fatigue resistance, while the annealed material exhibited the greatest fatigue resistance which was suggested as being related to its balance of tensile strength and ductility.

## **2.4 Mechanical Properties**

### ***2.4.1 Tensile properties***

The properties of thixomolded Mg alloys are strictly governed by the thixotropic microstructure which is unique and essentially different from die casting, although the alloy phase composition is similar [7]. Tensile properties of thixomolded AZ61A [51], AM50B [52]



and AZ91D [7-9, 52] Mg alloys have been studied and correlated with the processing conditions such as shot velocity, barrel temperature, injection pressure, etc. Some authors reported the creep strength of thixomolded AZ91 alloy [53, 54], while some reported microstructural evolution of friction stir welded, thixomolded Mg alloys AZ91 [55, 56] and AM60 [57]. Zhao *et al.* [58] investigated the relationship between microstructure and tensile properties on thixoformed AZ91D alloy with the addition of yttrium.

This study was aimed at evaluating tensile properties, strain hardening, strain rate sensitivity, and fracture mechanisms of thixomolded AZ91D and AM60B alloys in relation to the microstructural features. The energy absorption of Mg alloys during deformation is improved by the positive strain rate sensitivity in most cases [59]. The strain rate sensitivity for Mg alloys has been attributed to their hexagonal close packed (hcp) structure [60]. There are a few reports on the strain-rate sensitivity of die cast AZ91 and AM60 alloys, where the strain rate sensitivity decreases with increasing Al content for strain rates ranging between 0.012-1.2 s<sup>-1</sup> [61-63]. The tensile properties and fracture behavior of some wrought Mg alloys have also been reported to be strain rate sensitive during deformation [64, 65]. However, it is unclear how strong the strain rate sensitivity in the thixomolded Mg alloys would be, which will be explored in this thesis.

#### **2.4.2 Fatigue behavior**

It is recognized that a metal subjected to a repeated or fluctuating stress will fail at a stress much lower than that required to cause fracture on a single application of load. Such a failure

occurring under conditions of dynamic loading are called *fatigue failure*, that occurs only after a considerable period of service (time). It is often stated that fatigue accounts for about 90% of all service failures due to mechanical causes [66].

Fatigue can occur in many different forms. Fluctuations in externally applied stresses or strains result in mechanical fatigue. Cyclic loads acting in association with high temperatures cause creep-fatigue. When the temperature of the cyclically loaded component also fluctuates, thermo-mechanical fatigue is induced. Recurring loads imposed in the presence of a chemically aggressive embrittling environment give rise to corrosion fatigue. A fatigue failure is particularly harmful because it occurs without any obvious warning. On a macroscopic scale, the fracture surface in fatigue failure is usually normal to the direction of the principal stress. Three basic factors are necessary to cause fatigue failure. These are (1) a maximum tensile stress of sufficiently high value, (2) a large enough variation or fluctuation in the applied stress, and (3) a sufficiently large number of applied cycles [66].

The applications of Mg alloys in the transportation vehicles involve unavoidably the fatigue and cyclic deformation due to the fact that they are subjected to cyclic stresses and strains. Hence, it is necessary to evaluate the cyclic deformation resistance of these Mg alloys. A lot of investigations have been conducted on fatigue behaviors of Mg alloys in the last decade or so, included wrought alloys AZ31 [67-72], AM30 [73, 74], ZK60 [75, 76], and cast alloys AZ91 [28, 29, 33, 35], AM60 [22, 23, 27, 30], AM50 [36, 77, 78]. There are basically two types of fatigue, stress-controlled high cycle fatigue (HCF) and strain-controlled low cycle fatigue (LCF).

#### 2.4.2.1 Stress-controlled high cycle fatigue

The basic method of presenting stress-controlled fatigue data is by means of the  $S-N$  curve, a plot of stress  $S$  against the number of cycles to failure  $N$ . A log scale is always used for  $N$ . Generally the number of cycles to failure, in which a metal can endure before failure, increases with decreasing stress amplitude. For a few materials such as steel and titanium, the  $S-N$  curve becomes horizontal at a certain limiting stress, which is called the *fatigue or endurance limit* and the material presumably can endure an infinite number of cycles without failure. Most nonferrous metals, like aluminum, magnesium and copper alloys, have an  $S-N$  curve which slopes downward with increasing number of cycles. In such case it is common practice to characterize the fatigue properties of the material by specifying the fatigue strength at a given number of cycles. In the usual procedure if one or two specimens do not fail in the specified number of cycles (say  $10^7$ ), then the highest stress at which a runout (nonfailure) is obtained is taken as the *fatigue limit* [66]. Figure 2.2(a) and (b) shows the typical  $S-N$  curve for AZ91 and AM60 produced by HPDC. The fatigue limit for AZ91 and AM60 alloys are 45 MPa and 50 MPa, respectively, where runouts are seen after  $10^7$  cycles [20].

Previous work concerning fatigue behavior of AZ91 Mg alloy was mainly focused on the conventional or die cast alloys and stress-controlled  $S-N$  curves [19-21], coupled with the effect of friction stir welding and heat treatment [79-81] and AZ91 based metal matrix composite [82]. Recent studies focused on high cycle fatigue (HCF) of AM60 alloy produced

by die casting [21], extrusion [24-26], and equal channel angular pressing (ECAP) processes [22, 23].

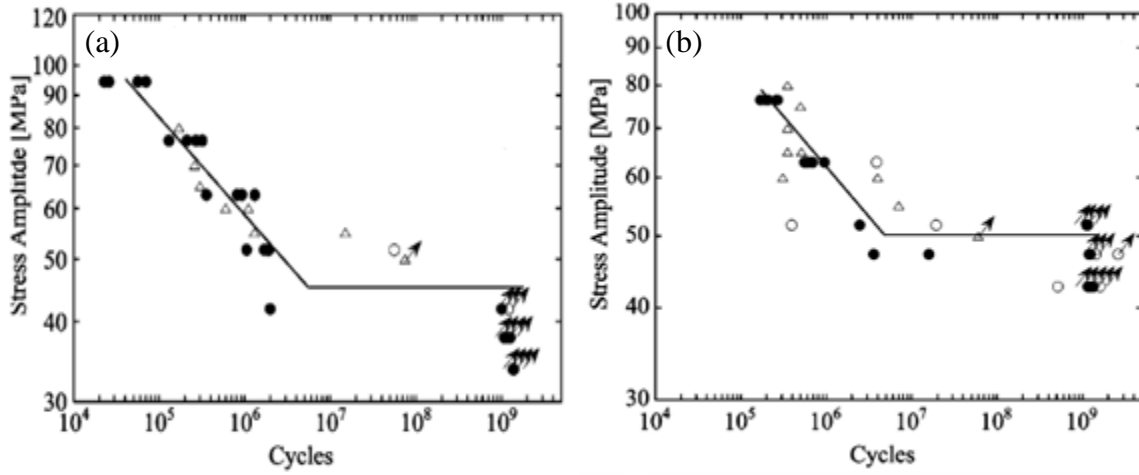


Figure 2.2: Fatigue data of (a) AZ91, and (b) AM60 produced by high-pressure die-casting. Solid circles refer to failure after surface or near surface crack initiation, and open circles indicate failure by cracks starting in the interior of the material. Open triangles refer to fatigue data of similar material tested at 50 Hz [20].

Potzies and Kainer [19] performed fatigue experiments on die cast AZ91 and modified AZ Mg alloys to analyze the effect of microstructural constituents such as porosity on the crack initiation and fatigue behavior. Similarly, Mayer *et al.* [20] evaluated the influence of porosity on stress-controlled high cycle fatigue properties of HPDC Mg alloys AZ91, AM60, AE42, AS21 and Al alloy AlSi9Cu3 using ultrasonic fatigue tests at a stress ratio of  $R = -1$  and a frequency of 20 kHz. Renner and Zenner [21] investigated the effect of different rib thicknesses and notch radii on the fatigue strength of die cast AZ91 and AM60 alloy under constant amplitude bending stresses at a stress ratio of  $R = 0$ . Kulyasova *et al.* [23] and

Islamgaliev *et al.* [22] reported the microstructures and fatigue properties of an ultrafine-grained AM60 Mg alloy processed by equal-channel angular pressing (ECAP) tested at constant stress amplitudes at  $R = 0.1$  and various temperatures. Gall *et al.* [83-85] examined the growth of microstructurally small fatigue crack in die cast AM60B alloy cycled under both high vacuum and water vapour environments. Zeng *et al.* [24, 26] studied constant load amplitude fatigue crack propagation of extruded and rolled AM60 alloy at a load ratio of  $R = 0$ . The effect of two different HPDC manufacturing processes on microstructure, tensile and fatigue properties of Mg alloy AM60 was investigated by Kang and Ostrom [86]. Some limited studies on fatigue behaviour of thixomolded AZ91 alloy [37, 38] has shown substantial higher fatigue of these alloys compared to its die cast counterparts.

#### 2.4.2.2 Strain-controlled low cycle fatigue

Low cycle fatigue conditions are frequently present where the repeated stresses are of thermal origin and at the notch root. Since thermal-stresses arise from the thermal expansion of the material, it is easy to see that in this case fatigue results from cyclic strain rather than from cyclic stress. The low cycle fatigue occurs at the high stress level and low numbers of cycles. Usually, nuclear pressure vessels, steam turbines, and most other type pressure vessels must be considered for low cycle fatigue [66]. Structural applications of Mg alloys in the transportation vehicles require low-cycle fatigue behavior, since cyclic loading or thermal stresses are frequently encountered and notches cannot be avoided. Fully reversed ( $R_\epsilon = -1$ ) strain-controlled fatigue tests were also reported for the die cast Mg alloys, including AZ91E-T4 [33], AM60B [30], and others such as AM50, AM60, AZ91 and AE44 [27].

These studies focused on the micro-mechanisms of fatigue crack nucleation and growth. Eisenmeier *et al.* [28] performed strain controlled fatigue tests at room temperature and at 130°C for investigating temperature effects on fatigue characteristics of Mg alloy AZ91. The test results were presented in terms of strain amplitudes versus the number of cycles to failure. Chen *et al.* [29] performed fully reversed total strain-controlled fatigue tests on conventional and die cast AZ91 alloys, while Li *et al.* [34] performed similar tests on die cast and solution treated (T4) AZ91 as well as AE42 alloys. They used Basquin and Coffin-Manson equations to evaluate fatigue life parameters. Lee *et al.* [31, 32] performed fatigue tests at total strain amplitudes ranging between 0.1% and 0.6% with  $R_\epsilon = -1$  on a HPDC AM60 alloy produced with different processing parameters to study the effects of macro-segregation on the fatigue behavior.

Liu *et al.* [35, 36] studied fatigue behavior of AZ91 in as high pressure die casting and subsequent heat treatments (T4 & T6). They showed all the specimens in different heat treatment histories exhibited cyclic strain hardening in different degrees, and found that T4 alloy showed longer fatigue life at high strain amplitudes and shorter fatigue life at low strain amplitudes than other two conditions. Goodenberger and Stephens [87] performed fatigue test of AZ91E-T6 cast Mg alloy with cylindrical specimens subjected to various strain ratios of  $R_\epsilon = 0, -1$  and  $-2$  and used different models to determine the mean stress effects on the fatigue life. Xu *et al.* [88] studied the cyclic stress-strain behavior using strain-controlled fatigue testing, where different  $R_\epsilon$ -ratios ranged from 0.1 to 0.7 at a strain amplitude of 0.3% was applied in order to examine the effect of  $R_\epsilon$ -ratio on the mean stress relaxation.

(a) Cyclic stress-strain curve

Figure 2.3 shows a schematic stress-strain loop under controlled constant strain cycling. O-A-B is the initial loading stress-strain curve. On unloading, yielding begins in compression at a lower stress C due to the Bauschinger effect. In reloading in tension, a hysteresis loop develops. The dimensions of the hysteresis loop are described by its width  $\Delta\epsilon$ , the total strain range, and its height  $\Delta\sigma$ , the stress range. The total strain range  $\Delta\epsilon$  consists of the elastic strain component  $\Delta\epsilon_e = \Delta\sigma/E$  plus the plastic strain component  $\Delta\epsilon_p$ . The width of the hysteresis loop will depend on the level of cyclic strain [66].

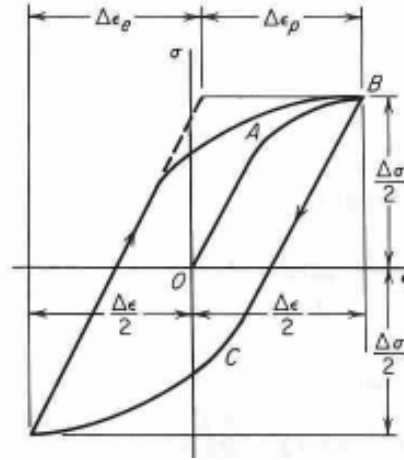


Figure 2.3: Stress-strain loop for constant strain cycling [66].

The cyclic stress-strain curve may be described by the following equation:

$$\frac{\Delta\sigma}{2} = K' \left( \frac{\Delta\epsilon_p}{2} \right)^{n'}, \quad (1)$$

where  $n'$  is the cyclic strain-hardening exponent and  $K'$  is the cyclic strength coefficient.

For metals  $n'$  varies between 0.10 and 0.20. Since plastic deformation is not completely reversible, modifications to the structure occur during cyclic straining and these can result in changes to the stress-strain response. Depending on the initial state a metal may undergo cyclic hardening, cyclic softening, or remain cyclically stable. It is not uncommon for all three characteristics to occur in a given material depending on the initial state of the material and test conditions. In general, metals with high monotonic strain-hardening exponents ( $n > 0.15$ ) undergo cyclic hardening; those with a low strain-hardening exponent ( $n < 0.15$ ) undergo cyclic softening. Cyclic hardening is expected when the ratio of the monotonic ultimate tensile strength to the 0.2 percent offset yield strength is greater than 1.4. When this ratio is less than 1.2, cyclic softening is to be expected. If the value is between 1.2-1.4, then no large changes in hardness are to be expected [66].

(b) Fatigue life and strain-life equation

The usual way of presenting low cycle fatigue test results is to plot the plastic strain range  $\Delta\epsilon_p$  against  $N$ . This type of behavior is known as the Coffin-Manson relation, which is best described by

$$\frac{\Delta\epsilon_p}{2} = \epsilon'_f (2N)^c, \quad (2)$$

where  $\Delta\epsilon_p/2$  = plastic strain amplitude,  $\epsilon'_f$  is the fatigue ductility coefficient,  $2N$  is number of strain reversals to failure (one cycle is two reversals) and  $c$  is the fatigue ductility exponent. Equation (2) becomes a straight line when plotted on log-log coordinates.



For the high cycle (low strain) regime, where the nominal strains are elastic, the following Basquin's equation would holds true,

$$\frac{\Delta \varepsilon_e}{2} = \frac{\sigma'_f (2N_f)^b}{E}, \quad (3)$$

where  $\Delta \varepsilon_e/2$  = elastic strain amplitude,  $E$  is the Young's modulus,  $\sigma'_f$  is the fatigue strength coefficient, and  $b$  is the fatigue strength exponent.

As described in the previous sub-section, the total strain amplitude could be expressed as elastic strain amplitude and plastic strain amplitude and an equation valid for the entire range of fatigue lives can then be obtained by superposition of Eqs. (2) and (3) [66],

$$\frac{\Delta \varepsilon_t}{2} = \frac{\Delta \varepsilon_e}{2} + \frac{\Delta \varepsilon_p}{2} = \frac{\sigma'_f (2N_f)^b}{E} + \varepsilon'_f (2N_f)^c. \quad (4)$$

Figure 2.4 shows the fatigue strain-life curve by plotting all three strain amplitudes (elastic, plastic and total) vs. the number of reversals to failure in log-log scale for HPDC AZ91 alloy published in [35]. The plastic and elastic strain amplitude and the corresponding stress amplitude in the stable condition or saturation should be used in the above equation. If no stable condition or saturation could be reached for some engineering materials, the mid-life stress and strain values are normally used. The curve tends toward the plastic curve at large total strain amplitudes and tends toward the elastic curve at small total strain amplitudes. The fatigue data based on above Eqs. (1-3) reported in the literature for AZ91 alloy in various processing conditions is also listed in Table 2.1.

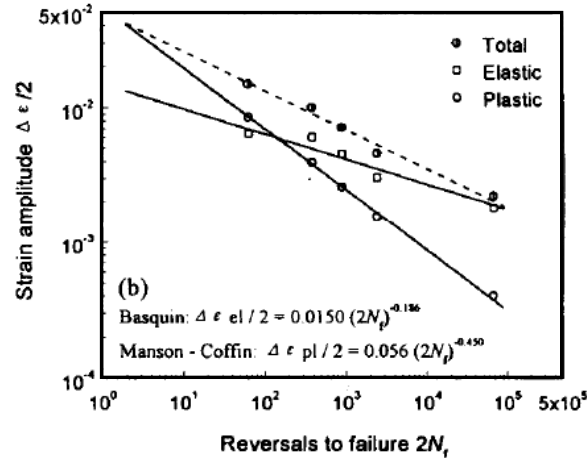


Figure 2.4: Fatigue life data of plastic, elastic, and total strain amplitudes vs. the number of reversals to failure [35].

Table 2.1: Strain-controlled fatigue parameters obtained for various AZ91 alloy in different processing conditions.

Processing conditions	$n'$	$K'$	$\sigma'_f$	$b$	$\epsilon'_f$	$c$	Reference
		(MPa)	(MPa)		(%)		
Vacuum die cast AZ91	-	-	630.0*	-0.143	4.3	-0.465	[28]
Conventional cast AZ91	0.185	402.8	399.9	-0.106	1.6	-0.289	[29]
Die cast AZ91	0.116	239.6	458.2	-0.135	3.6	-0.416	[29]
Die cast AZ91	-	-	480.7	-0.141	2.4	-0.365	[34]
Die cast AZ91-T4	-	-	491.9	-0.137	1.5	-0.209	[34]
Die cast AZ91	-	-	594.0*	-0.155	2.0	-0.360	[35,36]

\*The Young's modulus was assumed to be 45 GPa.

### (c) Fatigue fracture surface

The fatigue fracture process can be divided into following three stages: crack initiation, crack propagation and ultimate rapid failure. Basically about 10 percent of the fatigue life of metals elapsed before the initiation of a crack. In fact, the fatigue crack usually initiate at a free surface [66]. But significant experimental evidence shows that fatigue cracks initiates in cast Mg alloys [27, 30, 33] from shrinkage pores and/or inclusions. The porosity volume fraction, secondary dendrite arm spacing, grain size, etc., have a significant effect on the fatigue crack initiation. Fatigue crack propagation usually occurs in two stages. During stage I crack growth; the crack propagates along the persistent slip bands that involve the deepening of the initial crack on planes of high shear stress. Stage II crack growth involves well-defined crack growth in direction normal to maximum tensile stress [66].

To demonstrate the example of fatigue fracture surface, Figure 2.5 shows fatigue fracture surfaces in a die cast AZ91E-T4 Mg alloy [33]. Figure 2.5(a) shows the overall fracture surface indicating the different regions inspected with SEM. The small arrow in Figure 2.5(a) indicates the location of the fatigue crack nucleation site. In this sample the nucleation of the dominant fatigue crack formed at near-surface trapped oxide with a size of about 400  $\mu\text{m}$  (Figure 2.5(b)). Further three regions were marked in Figure 2.5(a) were examined with higher magnification SEM images. Close to the crack initiation site, the fracture surface Region 1 is characterized by an extremely flat region covered in fine fatigue striations (Figure 2.5(c)). In Region 2, the fatigue crack path changes to reveal more faceted and serrated fracture surface (Figure 2.5(d)), which is in contrast to continuous fatigue striations

as observed in Region 1. Even further from the fatigue crack nucleation site, in Region 3, the fracture surface has an extremely rough appearance with clear evidence of overload failure mechanisms on the microscale (Figure 2.5(e)).

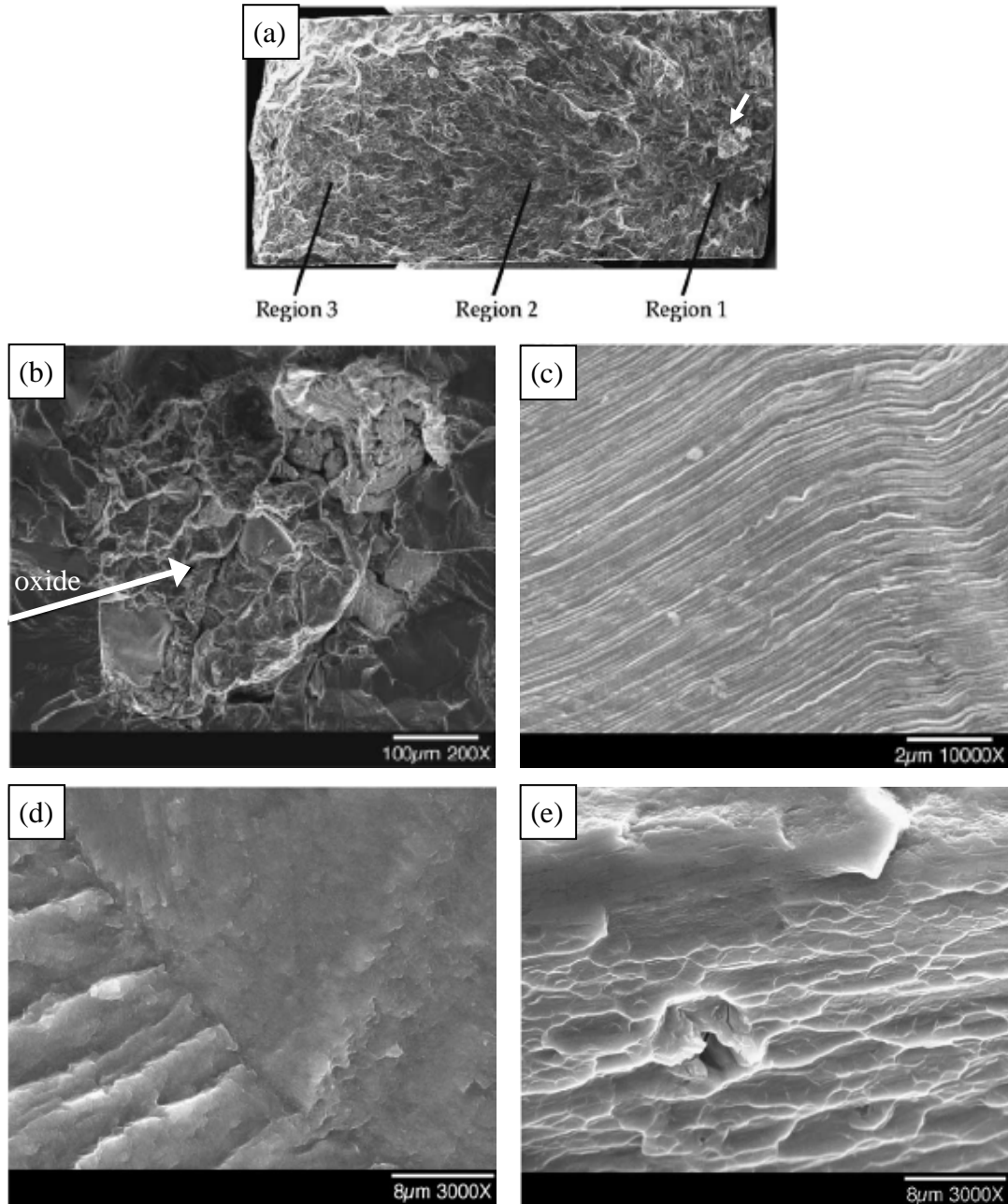


*Figure 2.5: SEM images of fatigue fracture surface in a die cast AZ91E-T4 Mg alloy: (a) overall view, (b) crack formation site, (c) Region 1, (d) Region 2, and (e) Region 3 [33].*

## 2.5 Problem Statement and Objectives

It is realized that in most Mg alloys some non-linear elastic behavior, also referred to as pseudoelasticity [67-70, 73, 75, 76, 89], was observed that led to hysteresis loops in the die cast Mg alloys [35, 78] being different from the typical hysteresis loops for most metals (Figure 2.3). Furthermore, the tension-compression asymmetry reflected directly by the hysteresis loops of wrought Mg alloys was associated with the presence of strong crystallographic texture and the resultant twinning-detwinning [68, 69, 73-75]. Currently more and more efforts are being made to reduce such asymmetry and understand the deformation mechanisms so as to expand the structural applications of Mg alloys. However, in these semi-solid processed Mg alloy, it remains unclear if the pseudoelastic behavior and twinning still occur during cyclic deformation, how the hysteresis loops are influenced by the strain ratio, and what the effects of the applied strain ratio on fatigue parameters are. Furthermore, it is unknown how strong the strain rate sensitivity in both AZ91D and AM60B thixomolded Mg alloys would be and what are the effect of heat treatment on the microstructure and mechanical properties of thixomolded AM60B alloy.

The objectives of the present investigation were, therefore, to identify the strain hardening and deformation behavior along with the effect of strain rate on the tensile properties, to evaluate LCF behavior, in conjunction with the influence of strain ratio in the thixomolded AZ91D and AM60B Mg alloys, and to study the effect of heat treatment on the mechanical properties of thixomolded AM60B alloy.

## CHAPTER 3

### EXPERIMENTAL PROCEDURE

#### 3.1 Materials and Composition

Two thixomolded Mg alloys, namely, AZ91D and AM60B in the form of 3.2 mm (0.125”) thick plates for the current investigation were produced by G-Mag International and received from CANMET-Materials Technology Laboratory (MTL), Ottawa, Canada. These plates with a size of 100 × 150 mm (4” × 6”) are shown in Figure 3.1. The chemical compositions for both alloys are listed in Table 3.1.



*Figure 3.1: Thixomolded plate used in the present investigation.*

*Table 3.1: Chemical composition (in wt%) of thixomolded AZ91D and AM60B.*

Alloy	Al	Zn	Mn	Mg
AZ91D	8.64	0.592	0.261	Balance
AM60B	5.89	0.0032	0.302	Balance

A Hymet 1000 thixomolding equipment supplied by Husky molds was used to produce the shotgun at G-Mag International. The specifications for the equipment are as follows:

- Clamp force: 1000 ton
- Injection pressure: 830 psi
- Injection speed: 6 m/s
- Barrel size: 85 mm
- Shot capacity: 3.2 kg
- Final weight: 2.87 kg

### **3.2 Heat treatment**

The heat treatment (HT) procedure used in the present investigation for AM60B alloy is shown in Figure 3.2. From the binary Mg-Al phase diagram, the dissolution of the  $\beta$  phase is expected to occur at a temperature of 400°C [13] in AM60 alloy. So the temperature above this solvus point was chosen for the solution treatment (T4). In the solution heat treatment (T4) the parts were loaded into the furnace at about 260°C and then raised to the solution treating temperature slowly, here 413°C, to avoid fusion of eutectic compounds and resultant formation of voids. The time is typically about 2 h. At this temperature the parts were held for 16 h, followed by the warm water (65°C) quenching. Aging treatment (T5) was carried out on thixomolded plates at 168°C, where the part was held for 16 h, followed by air cooling (slow) to room temperature. Precipitation heat treatment (T6) that combines both solution treatment and aging was also carried out. These T4, T5 and T6 heat treated plates were subsequently cut for metallographic, tensile and fatigue testing.

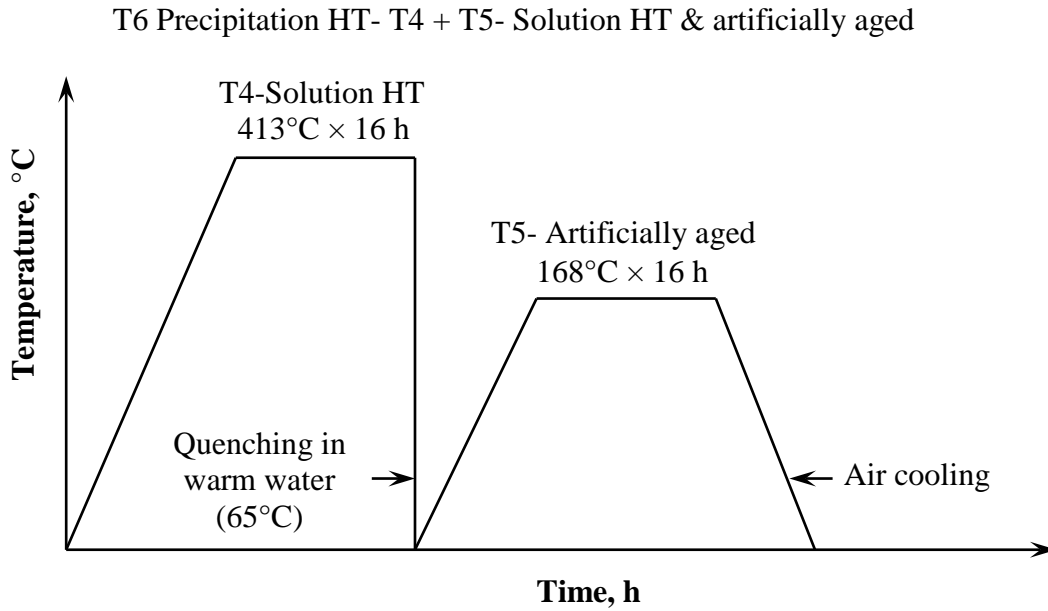


Figure 3.2: Heat treatment procedure for the thixomolded AM60B alloy.

### 3.3 Sample Preparation and Testing

The thixomolded, solution treated, artificially aged, and solution HT then artificially aged samples were designated as Tx, T4, T5, and T6, respectively. The metallographic and mechanical test samples are prepared according to the following procedures.

#### 3.3.1 Metallography

All metallographic samples (approx. 5 mm × 5 mm in the cross section) for the microstructural characterization were cut from both thixomolded and their heat treated plates. The samples were cold mounted using LECO 7007 resin powder and liquid (mixing ratio: 2 parts of resin added to 1 part of catalyst). Hot mounting was avoided to prevent any possible



microstructural change due to the effect of temperature during sample preparation. The mounted samples were manually ground with SiC sand papers with a grit number of 320, 600, 800, and 1200, respectively. Water was used as lubricant in each grinding steps. Polishing was carried out with 6  $\mu\text{m}$  and 1  $\mu\text{m}$  diamond paste using diamond extender (mixture of rust inhibiting solution and distilled water - 10% solution by volume) as lubricant. Cleaning of the mount after polishing involved dipping in and spraying ethanol, ultrasonically cleaning in ethanol, followed by drying with compressed air. After the final polishing with 0.05  $\mu\text{m}$  alumina paste, the polished samples were etched with Acetic-Picral (10 ml acetic acid, 4.2 g picric acid, 10 ml distilled water, and 70 ml ethanol) to reveal the macrostructure of the alloys. The microstructure was examined via light microscope equipped with a quantitative image analyzer, and scanning electron microscope (SEM) coupled with energy dispersive X-ray spectroscopy (EDS) analysis and 3D imaging system.

### 3.3.2 *Quantitative image analysis*

Microscopic images were taken using a light microscope and image analyses were subsequently performed using Clemex software to obtain the area fraction of various phases such as solid primary  $\alpha$ -Mg particles, and amount of porosity as well as to measure the grain size. Overall at least 15 locations for each sample were studied and the average values have been reported in this report. The Clemex image analysis system was comprised of a Clemex CMT software adaptable to ASTM standards, a Nikon optical microscope (10 $\times$  eye piece, five different object lenses with magnifications of 5 $\times$ , 10 $\times$ , 20 $\times$ , 40 $\times$ , and 100 $\times$ ), a high-resolution digital camera, and a high performance computer to carry out the detailed analysis.

### 3.3.3 *Hardness tests*

A computerized Buehler microhardness testing machine was used for the micro-indentation hardness tests of thixomolded Mg alloys in HV, where a load of 100 g and duration of 15 s were used. Micro-hardness tests were performed on the mounted sample after the microstructural characterization. To compare the effect of heat treatment, surface hardness testing was carried out on the flat panels of as-thixomolded and its heat treated AM60B samples. Hardness test was measured in HRC on Buehler hardness tester with diamond brale (indenter) and 150 kg load. Both types of hardness testers were calibrated using the reference blocks prior to the tests to verify the accuracy of the hardness values.

### 3.3.4 *Tensile tests*

The sub-sized tensile test samples were prepared according to the ASTM-E8M standard (with a gauge length of 25 mm), which were cut from the flat panels (Figure 3.1). The specimen geometry and dimensions are shown in Figure 3.3. The tests were carried out using a computerized United tensile testing machine at five different strain rates:  $1 \times 10^{-1} \text{ s}^{-1}$ ,  $1 \times 10^{-2} \text{ s}^{-1}$ ,  $1 \times 10^{-3} \text{ s}^{-1}$ ,  $1 \times 10^{-4} \text{ s}^{-1}$ , and  $1 \times 10^{-5} \text{ s}^{-1}$  for both thixomolded Mg alloys. To evaluate the effect of heat treatment, the heat-treated samples were tested at a strain rate of  $1 \times 10^{-3} \text{ s}^{-1}$ . At each strain rate minimum two samples were tested to ensure the repeatability and in case of unsatisfied results more samples were tested. The strain rates were controlled by 25 mm gauge length extensometer, and no further higher strain rates can be achieved due to the limitation of both extensometer and machine. All the tests were conducted at room

temperature. The fracture surfaces of tensile specimens were analyzed using a scanning electron microscope (SEM) equipped with an energy dispersive X-ray spectroscopy (EDS) system. The tensile properties, including 0.2% yield strength (YS), ultimate tensile strength (UTS) and percent elongation to failure (%El) were evaluated using engineering stress-strain curves. The strain (or work) hardening exponent ( $n$ ) and the strength coefficient ( $K$ ) were determined using the Hollomon equation ( $\sigma = K\epsilon^n$ ) by plotting  $\log \sigma$  vs.  $\log \epsilon$ . Strain hardening rate was presented in the form of Kocks-Mecking type plot to examine the strain hardening characteristics. The fracture surfaces of tensile specimens were analyzed via SEM to identify the fracture mechanisms.

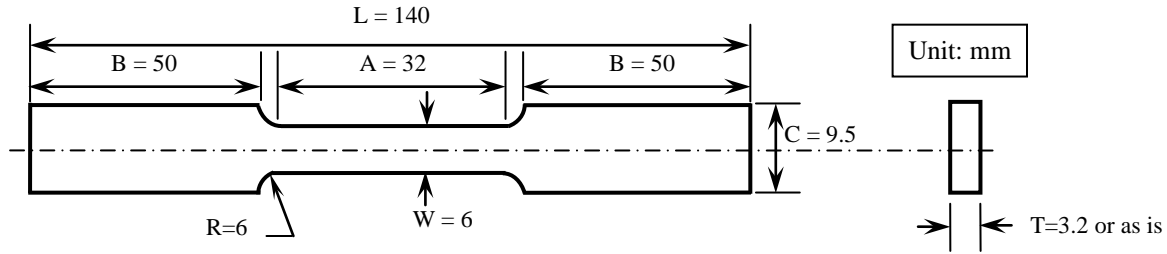


Figure 3.3: Geometry of the sub-sized tensile test specimen according to ASTM E8M.

### 3.3.5 Fatigue tests

Fatigue tests were performed using a fully computerized servo-hydraulic INSTRON 8801 fatigue testing system. The sample geometry for the fatigue test was shown in Figure 3.4. The gauge length was kept 12.5 mm and a cross section was 3.5 mm  $\times$  3.2 mm in the gauge section. The tests were conducted in a strain control mode according to ASTM E606 standard for both thixomolded and heat treated samples. The fatigue tests were carried out at

completely reversed strain cycle ( $R_\epsilon = -1$ ), a constant strain rate of  $1 \times 10^{-2} \text{ s}^{-1}$  and room temperature of  $25^\circ\text{C}$ . Triangular waveform loading was applied during the tests. The strain controlled tests at lower strain amplitude levels were continued up to  $10^4$  cycles, and then the tests were changed to load control tests with a frequency of 50 Hz, using sine waveform and maintaining the same stress amplitude and mean stress at  $10^4$  cycles. Low cycle fatigue tests were performed at total strain amplitudes of 0.2%, 0.3%, 0.4%, 0.6%, 0.8%, 1.0% and 1.2% with at least two samples tested at each level of the strain amplitudes. The calibration of both load and strain channels was performed for each individual sample prior to testing.

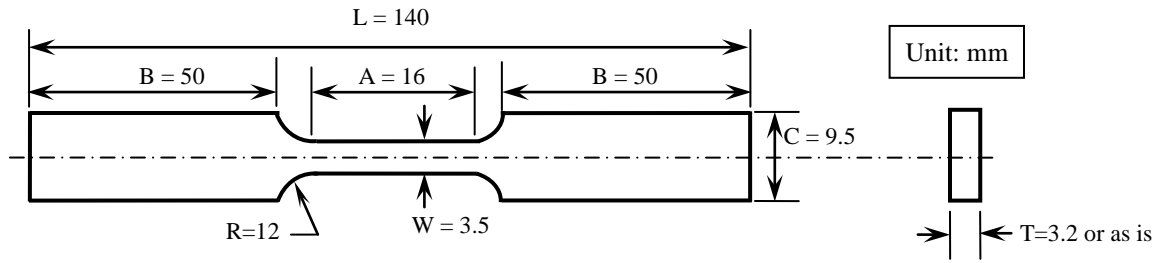


Figure 3.4: Geometry of the sub-sized fatigue test specimen.

To examine the effect of strain ratio on the fatigue behavior of the thixomolded AZ91D and AM60B alloy, four strain ratios,  $R_\epsilon = 0.5, 0, -1$ , and  $-2$ , were used at a given total strain amplitude of 0.6%. The varying strain ratio tests were performed in the same manner at a strain rate of  $1 \times 10^{-2} \text{ s}^{-1}$  and room temperature with triangular waveform loading as well. After fatigue tests, the SEM equipped with an energy dispersive X-ray spectroscopy (EDS) system was used to examine the fatigue crack initiation sites and identify the mechanism of fatigue crack propagation under the above applied conditions.

# CHAPTER 4

## MECHANICAL PROPERTIES OF SEMI-SOLID PROCESSED MAGNESIUM ALLOYS

### 4.1 Microstructure

The optical micrographs of the semi-solid processed (thixomolded) AZ91D and AM60B Mg alloys are shown in Figure 4.1(a) and (b), respectively. The microstructure in both alloys consisted basically of globular primary  $\alpha$ -Mg surrounded by the eutectic structure. Such a microstructure could be considered as suspension of solid primary  $\alpha$ -Mg particles dispersed in a liquid matrix in the absence of dendrites [8, 90]. The eutectic structure consisted of a mixture of eutectic  $\alpha$ -Mg and intermetallic compound  $\beta$ -Mg<sub>17</sub>Al<sub>12</sub>, which was also reported by Fan *et al.* [91] and Czerwinski *et al.* [7].

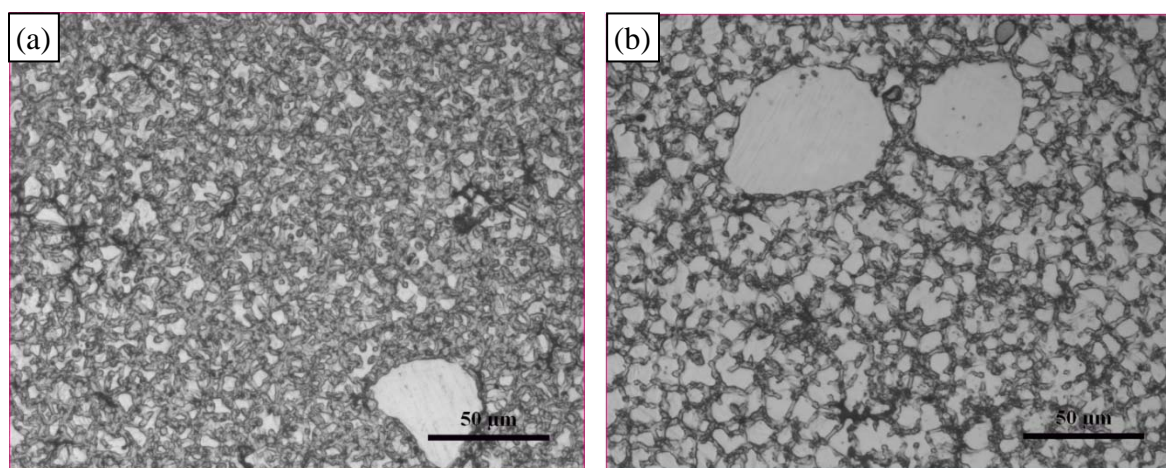


Figure 4.1: Optical microscope images showing the microstructure of thixomolded Mg alloy (a) AZ91D and (b) AM60B.

It is seen from Figure 4.1 that a larger amount of eutectic structure or a smaller amount of solid primary  $\alpha$ -Mg particles was present in the thixomolded AZ91D alloy than in the AM60B alloy mainly due to the difference in the Al content (8.64 wt% in the AZ91D alloy vs. 5.89 wt% in the AM60B alloy). Also, some pores in both thixomolded alloys could be seen in Figure 4.1. The volume fraction of solid primary  $\alpha$ -Mg particles and the amount of porosity, determined via a quantitative image analysis system, are shown in Table 4.1. While the volume fraction of solid primary  $\alpha$ -Mg particles was lower in the AZ91D alloy than in the AM60B alloy, the porosity was almost the same in both alloys and relatively small (about 1.25-1.30%).

*Table 4.1: Volume fraction of solid primary  $\alpha$ -Mg phase, porosity, and microhardness values in both thixomolded Mg alloys AZ91D and AM60B.*

<b>Specimen</b>	<b>Volume fraction of solid primary <math>\alpha</math>-Mg phase</b>	<b>Average porosity, (%)</b>	<b>Microhardness, (HV)</b>
AZ91D	0.35	1.25	62.1 $\pm$ 4.8
AM60B	0.57	1.30	50.4 $\pm$ 4.7

Details of the network-like eutectic structure under a higher magnification is shown in Figure 4.2 for AZ91D alloy, together with the EDS line scan results showing the compositional variation across the intermetallic phase. It is seen that in the AZ91D alloy the Al-rich eutectic took a completely divorced form, with massive and continuous precipitation of the  $\beta$  intermetallic phase, as reported in [92] as well. The concentration of Mg and Al inside the  $\alpha$ -

Mg grain was basically constant, while a sharp increase in Al content occurred at the  $\beta$ - $\text{Mg}_{17}\text{Al}_{12}$  phase. This indicates local micro-segregation due to the coring effect. Fan *et al.* [91] also observed similar micro-segregation effect in their rheo-diecast AZ91D alloy. Further distribution of other chemical elements, including Zn and Mn, within the microstructure, was traced by EDS spectrum. Figure 4.3 shows a SEM image with some EDS spectrum analyses for AZ91D alloy. It is clear that the white round particles contained mainly Al and Mn (Figure 4.3(b)), and the center of the  $\alpha$ -Mg grain contained basically Mg and traces of Al, Zn and Mn were below the detection level (Figure 4.3(c)). While moving towards the interface with the intermetallic  $\beta$ - $\text{Mg}_{17}\text{Al}_{12}$  phase, the content of Al and Zn also increased (Figure 4.3(d)). Czerwinski *et al.* [7] reported an obvious increase in Al and Zn content towards the intermetallic phase in a thixomolded AZ91D alloy and a part of the Al atoms could be substituted by Zn. It was thus claimed that at temperatures below 437°C it had a form of  $\text{Mg}_{17}(\text{Al,Zn})_{12}$ , possibly  $\text{Mg}_{17}\text{Al}_{11.5}\text{Zn}_{0.5}$  [7].

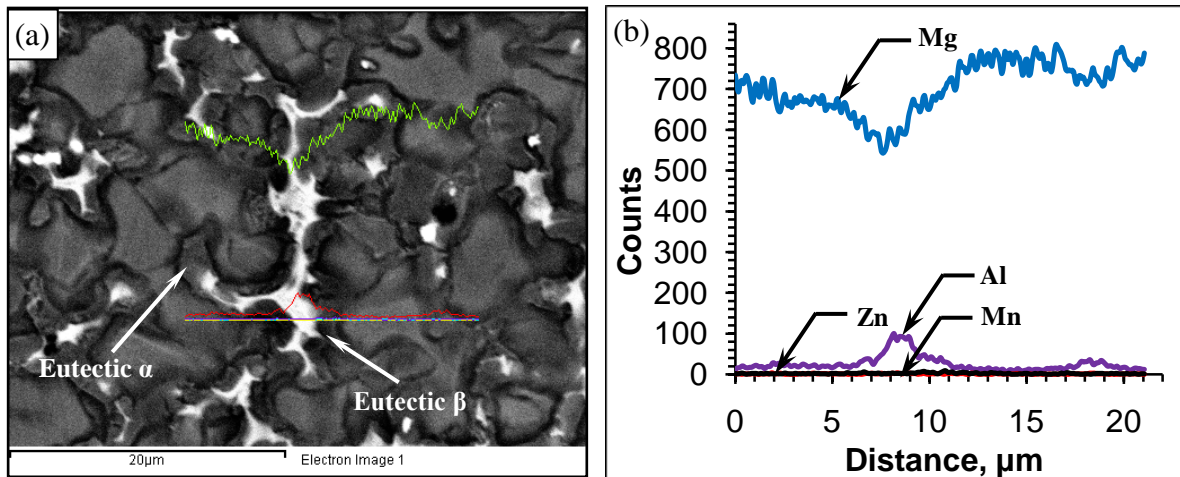


Figure 4.2: EDS line scan across the eutectic structure in the thixomolded AZ91D alloy, (a) overall view, and (b) magnified view of the compositional variation.

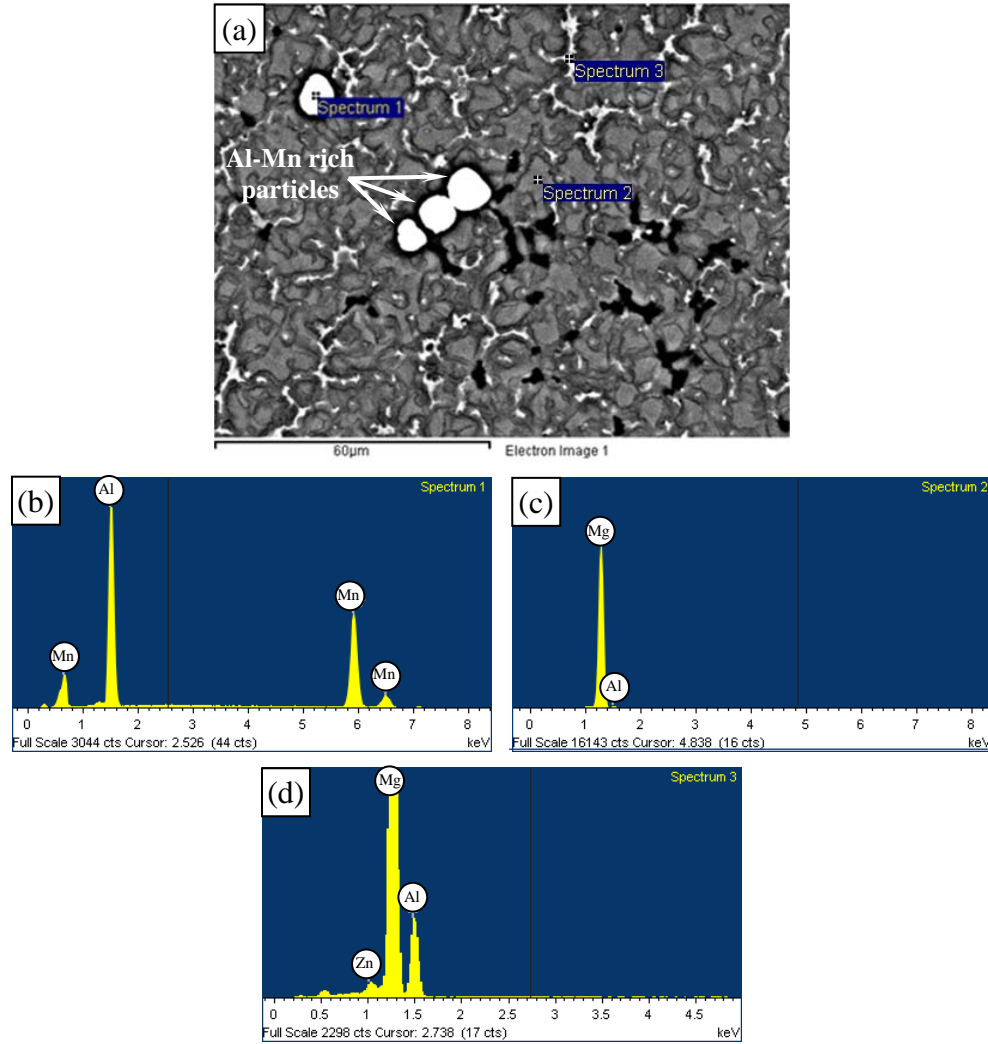


Figure 4.3: EDS point analysis in the AZ91D alloy, (a) SEM image showing the locations for the analysis, (b) EDS spectrum for an Al-Mn rich particle (spectrum 1 in (a)), (c) EDS spectrum for a primary  $\alpha$ -Mg grain (spectrum 2 in (a)), and (d) EDS spectrum for the eutectic structure containing intermetallic compound (spectrum 3 in (a)).

Figure 4.4 presents a SEM micrograph and its corresponding EDS line scan across a white particle for AM60B alloy, and Figure 4.5 shows the EDS point analyses on this white particle and in other areas. Again the strips of intermetallic  $\beta$ -phase were observed with Al-rich solid solution bands (Figure 4.5(d)), while the white particle phase contained Mn and Al (Figs. 4



and 5(b)). According to Wang *et al.* [93] these white particles could be  $\text{Al}_8\text{Mn}_5$  precipitates. It should be pointed out that in terms of the Mg-Al equilibrium phase diagram, the intermetallic  $\beta\text{-Mg}_{17}\text{Al}_{12}$  phase in the eutectic structure would not be anticipated to appear when the aluminum content was below about 13 wt%. However, the cooling rates in practical casting processes were generally sufficient to cause some eutectic to form during solidification of Mg alloys containing an Al content even as low as 2 wt% [92, 94]. It follows that the eutectic structure in the present thixomolded AZ91D and AM60B Mg alloys would be expected to be present since the Al content was much higher than 2 wt%, as mentioned above. As seen from Table 4.1, the lower volume fraction of solid primary  $\alpha\text{-Mg}$  phase in the AZ91D alloy corresponded to a higher volume fraction of eutectic structure (Figure 4.1). This implied that a higher amount of harder and more brittle intermetallic  $\beta\text{-Mg}_{17}\text{Al}_{12}$  phase existed in the composite-like eutectic, thus giving rise to a higher hardness value, as seen in Table 4.1.

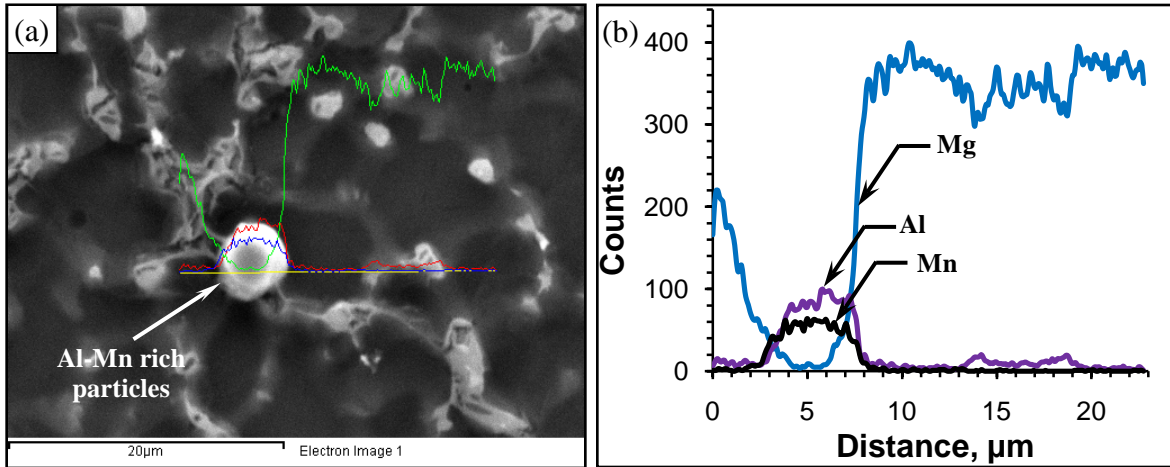


Figure 4.4: EDS line scan across an Al-Mn particle in the thixomolded AM60B alloy, (a) overall view, and (b) magnified view of the compositional variation.

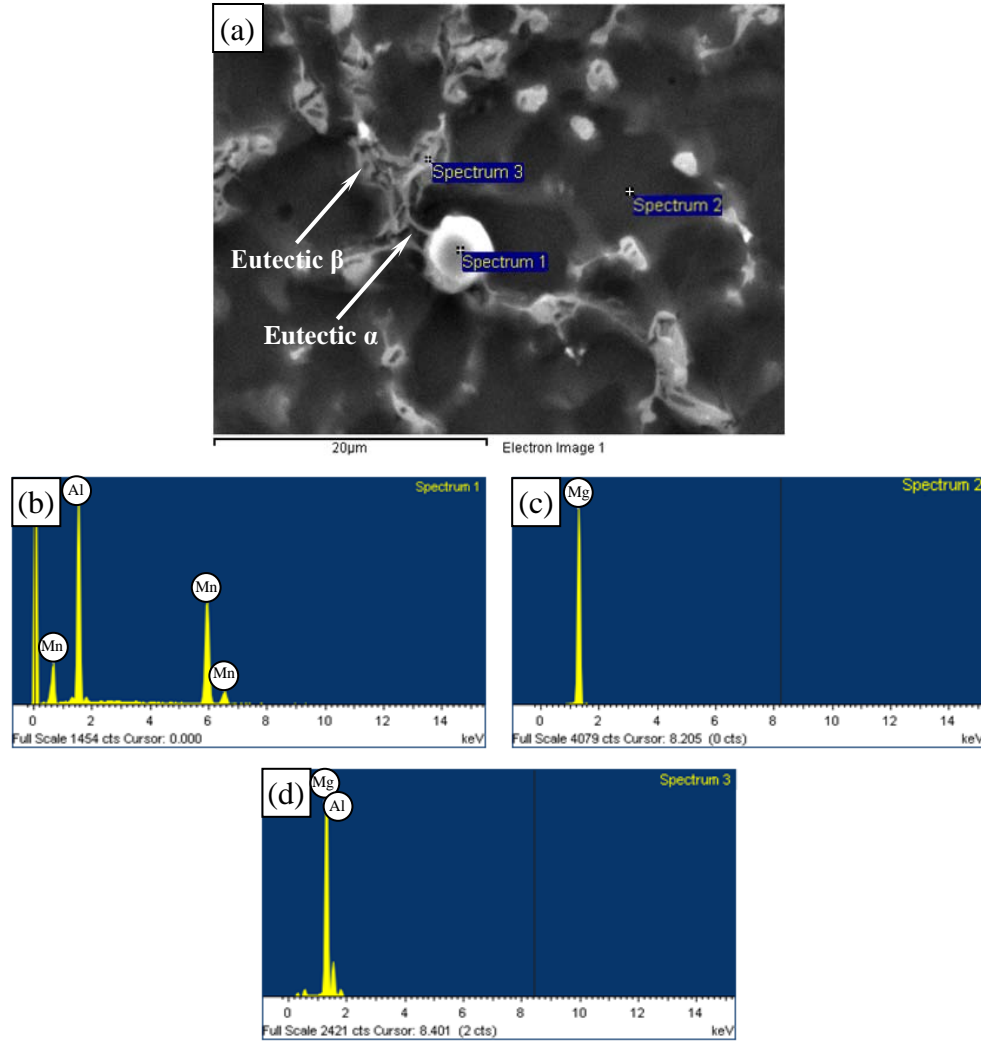


Figure 4.5: EDS point analysis in the AM60B alloy, (a) SEM image showing the locations for the analysis, (b) EDS spectrum for an Al-Mn rich particle (spectrum 1 in (a)), (c) EDS spectrum for a primary  $\alpha$ -Mg matrix (spectrum 2 in (a)), and (d) EDS spectrum for the eutectic structure containing intermetallic compound (spectrum 3 in (a)).

## 4.2 Tensile Properties

Experimental procedure for the tensile testing has been presented in section 3.3.4. The results of tensile tests carried out on semi-solid processed Mg alloys are presented in this section.

#### 4.2.1 Comparing tensile properties

Figure 4.6 shows typical engineering stress-strain curves for thixomolded AZ91D and AM60B specimens tested at different strain rates. It is seen that the AZ91D alloy had higher yield strength (YS) and lower ductility compared to AM60B alloy. It is of interest to observe that AM60B alloy showed a localized, heterogeneous type of transition rather than having a flow curve with a gradual transition from elastic to plastic deformation like AZ91D alloy. This indicated a tendency of yield-point-like phenomenon apparent on the stress-strain curves for AM60B alloy. The yield-point phenomenon had been reported in other metals and alloys including hcp materials, such as titanium, cadmium and zinc [66]. The yield point phenomenon was recently observed in Ti-3Al-4.5V-5Mo titanium alloy [95], Ti-20V-4Al-1Sn titanium alloy [96], and ultra-fine grained Al-Mg alloy [97].

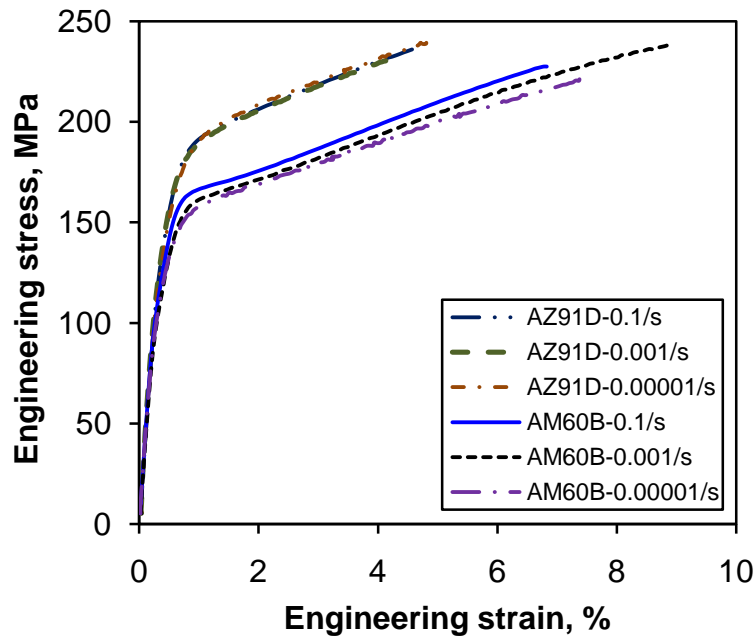


Figure 4.6: Typical engineering stress-strain curves obtained at different strain rates for thixomolded AZ91D and AM60B alloys.

Two major models on the yield point explanations proposed were associated with the impurity (e.g., carbon, nitrogen) locking/pinning and dislocation breakaway from the solute atmospheres by Cottrell and Bilby [98], and the increase of dislocation density with deformation together with the stress dependence of dislocation mobility by Johnston and Gilman [99]. While the impurity locking was stated to be a special case of yield point behavior [66], it was also possible that the yield point behavior could be controlled by combining both models [100]. The presence of the yield-point-like phenomenon in the AM60B alloy might be due to the interaction of dislocations and solute atoms [101] that increase the dislocation density, thus introducing some strain hardening as well. Further studies on the controlling mechanism of the yield-point-like phenomenon in the AM60B alloy are needed. From Figure 4.6 it is seen that the yield-point-like phenomenon in AM60B alloy became slightly more obvious with increasing strain rate, which was also in agreement with the previous observations documented in [66]. The ultimate tensile strength (UTS) for both thixomolded alloys was equivalent (about 225-235 MPa). This was due to the fact that AZ91D alloy failed before reaching the potential ultimate stress as a result of premature failure arising from the lower elongation (Figure 4.6). The lower ductility and higher yield strength of AZ91D alloy were apparently attributed to the higher amount of intermetallic  $\beta$ -phase. Since the intermetallic  $\beta$ -Mg<sub>17</sub>Al<sub>12</sub> phase (with a hardness value of about HV280 [102]), was much harder than the  $\alpha$ -Mg solid solution, more intermetallic  $\beta$ -phase would result in a higher resistance to the dislocation movement and/or twinning during the tensile deformation.

#### 4.2.2 Strain hardening and strain-rate sensitivity

The strain rate sensitivity in both thixomolded alloys seemed to be weak (as we can see from Figure 4.6), but it was slightly higher in AM60B alloy than in AZ91D alloy. To better see this, the yield strength (YS), ultimate tensile strength (UTS), percent elongation (%El) and strain hardening exponent ( $n$ ) as a function of strain rate are plotted in Figure 4.7(a-d) for both AZ91D and AM60B alloys, respectively.

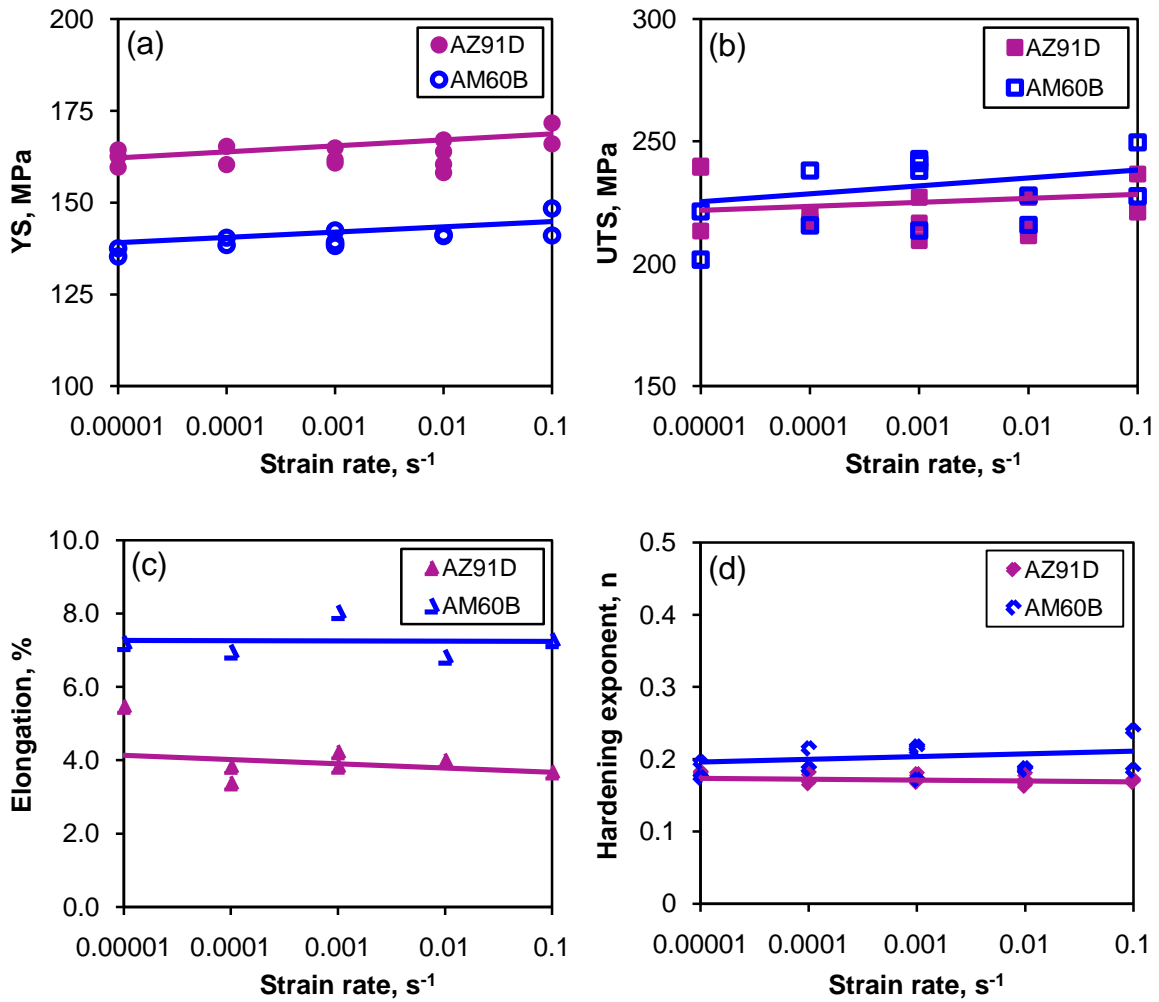


Figure 4.7: Effect of strain rate on (a) yield strength, (b) ultimate tensile strength, (c) % elongation, and (d) strain hardening exponent for thixomolded AZ91D and AM60B alloys.

There seemed to be only a slight linear increase in the YS and UTS with increasing strain rate (in the semi-log scale) for both AZ91D and AM60B alloys (Figure 4.7(a) and (b)). Likewise, the effect of strain rate on the ductility was observed to be insignificant as well for both AZ91D and AM60B alloys (Figure 4.7(c)). It is seen from Figure 4.7(d) that the strain hardening exponents varied from 0.18 to 0.21 for both alloys, and the n-value of AM60B alloy was slightly higher than that of AZ91D alloy. This was related to the lower yield strength of AM60B alloy while the UTS of both alloys were similar. Again the effect of strain rate on n-value was negligible for AZ91D alloy, while AM60B alloy had a slight increase in the n-value with increasing strain rate.

Similar results were reported by Abbott *et al.* [61] where the strain rate sensitivity reduced to almost zero once about 6% Al was present in the Mg alloy. However, it was clear that the ductility of AM60B alloy (7~8%) was higher than that of AZ91D alloy (about 4%) due to the presence of different amounts of intermetallic  $\beta$ -phase mentioned above. It should be noted that only those valid ductility data with failure occurred within the specified gauge length were plotted in Figure 4.7(c) in accordance with the ASTM-E8 standards. The failure location of the thixomolded (or in general, all cast) alloys would be related to the inhomogeneous cast microstructure in which coarse grains, fine grains, uneven amount of intermetallics and porosity co-existed, since fracture normally initiated at the weakest location of a test sample where the maximum stress concentration occurred.

Figure 4.8 shows a typical Kocks-Mecking plot of strain hardening rate ( $\theta=d\sigma/d\epsilon$ ) vs. true stress ( $\sigma$ ) at different strain rates for AZ91D and AM60B alloys. Stage III hardening

occurred immediately after yielding in both alloys, as indicated by the linear decrease in the strain hardening rate [103, 104]. Strain hardening rates were equivalent for both alloys, but the initial stress of hardening was different (~160 MPa for AZ91D and ~140 MPa for AM60B) corresponding to their yield strength (Figure 4.7(a)). The slope of stage III hardening decreased (i.e., it looked like in a counter-clockwise rotation) with decreasing strain rate for both alloys. This suggests a certain strain rate effect on the stage III work hardening rate.

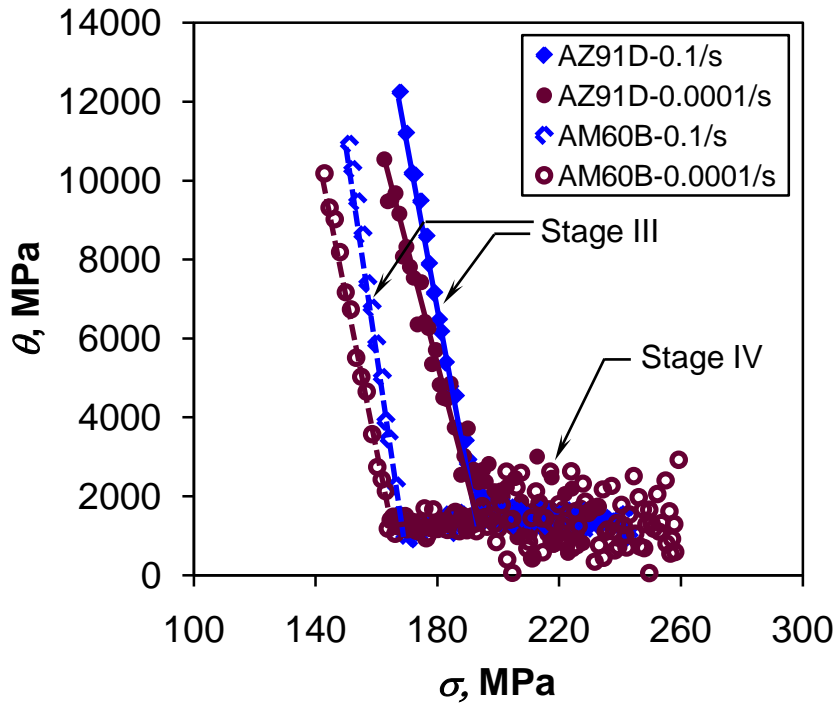


Figure 4.8: Strain hardening rate ( $\theta$ ) as a function of true stress ( $\sigma$ ) at varying strain rates for thixomolded AZ91D and AM60B alloys.

Kocks and Mecking [103] reported that in both single crystals and polycrystals, stage III hardening was characterized by a specific and strong dependence of temperature and strain rate. This effect could be understood on the basis of the following equation [103]:

$$\theta = \theta_0 - \frac{R_d \sigma}{\dot{\epsilon}^{\frac{1}{q}}}, \quad (5)$$

where  $R_d$  and  $q$  are temperature dependent, but are independent of stress ( $\sigma$ ) and strain rate ( $\dot{\epsilon}$ ), which are constants in this study,  $\theta$  is the strain hardening rate in stage III, and  $\theta_0$  is considered as a constant. It is clear that based on Eq. (5) the strain hardening rate  $\theta$  decreased with decreasing strain rate at a given true stress. When the true stress exceeded a certain value (~190 MPa for AZ91D alloy and ~165 MPa for AM60B alloy),  $\theta$  became small and stage IV hardening occurred. In this stage large plastic strain could occur at a very low, virtually constant work hardening rate [103].

### 4.3 Role of Twinning in Strain Hardening

During tensile deformation of Mg alloys with a hcp crystal structure, the basal slip  $\langle a \rangle$ , prismatic slip  $\langle a \rangle$  and pyramidal slip  $\langle c+a \rangle$  could be activated [105]. Also Mg alloy exhibited a strong propensity for mechanical twinning because twinning had a lower critical resolved shear stress (CRSS) than  $\langle c+a \rangle$  pyramidal slip at room temperature [26]. The effect of twinning could be explained as the reorientations of the basal planes that then became more favorable relative to the stress axis such that the slip could take place [106]. This would cause the higher strain hardening as a consequence of numerous dislocation pile-



ups at the grain boundaries and twin boundaries as well as slip-twinning interactions [26]. To demonstrate the evidence of twinning occurred close to the fracture surface, some failed tensile specimens were sectioned, polished, etched and examined using SEM. The typical SEM images are illustrated in Figure 4.9(a) and (b) for AZ91D and AM60B alloys, respectively. It is seen that some deformation twins occurred in a few  $\alpha$ -Mg cells, as indicated by arrows, which would be favorably oriented with respect to the stress axis. This is consistent with the observations of Yan *et al.* [106] in the AM60 cast Mg alloy as well.

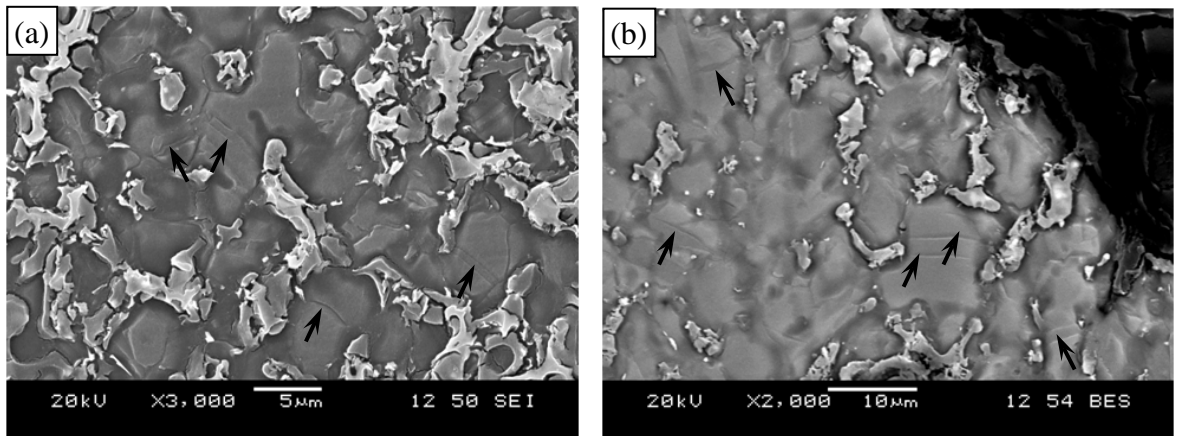
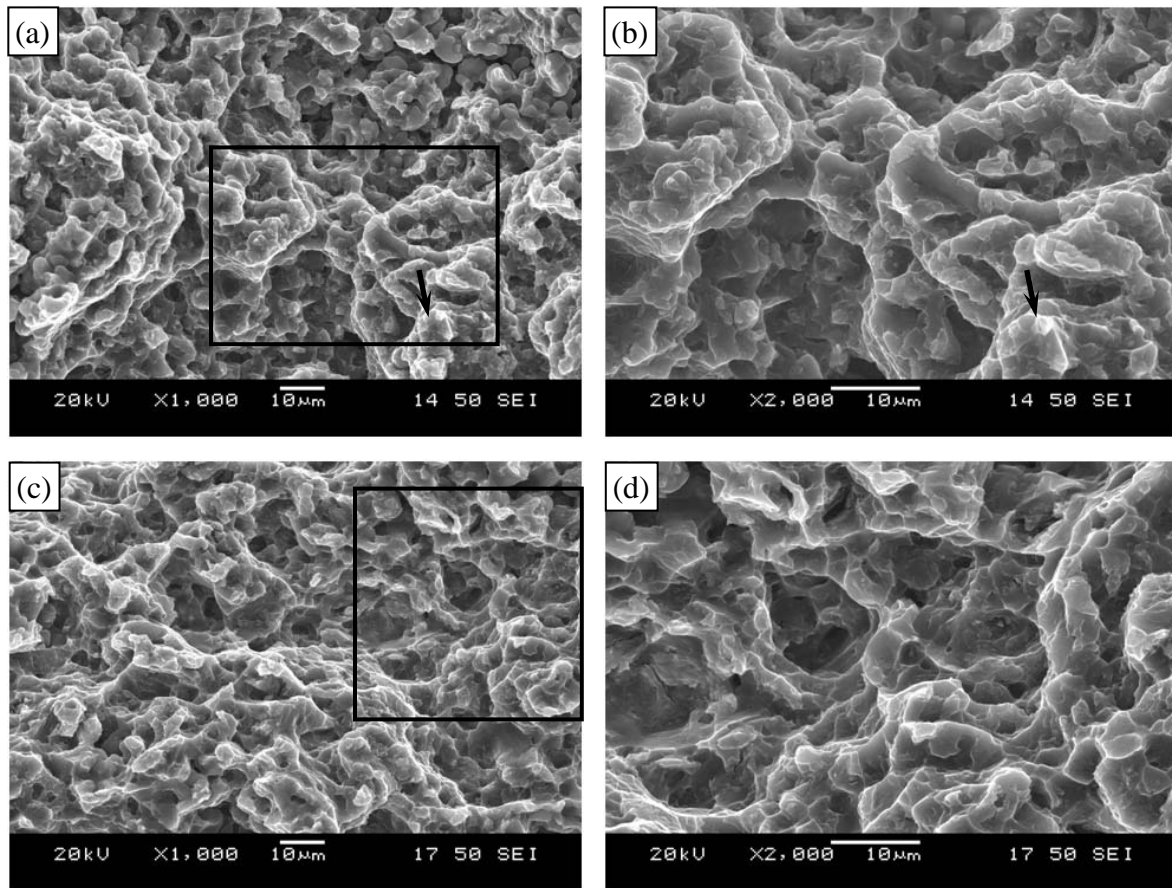


Figure 4.9: Typical SEM images showing the occurrence of twinning near the fracture surface of thixomolded alloys (a) AZ91D and (b) AM60B.

#### 4.4 Tensile Fracture Surfaces

Figure 4.10 shows some typical SEM images of the fractured tensile samples at different magnifications for both AZ91D and AM60B alloys.



*Figure 4.10: Typical SEM images showing the fracture surfaces of tensile tested (a) AZ91D alloy, (b) magnified view of the boxed region in (a), (c) AM60B alloy, and (d) magnified view of the boxed region in (c).*

AZ91D alloy appeared to exhibit more cleavage-like facets and steps in conjunction with some intergranular cracking (somewhat like grain pull-out) due to the presence of more eutectic microconstituent between the primary  $\alpha$ -Mg grains, especially in the vicinity of pores where the stress concentration was present as shown in Figure 4.10(a) and (b). This corresponded well to the relatively low ductility of AZ91D alloy (Figure 4.7(c)). An area with a brighter contrast in Figure 4.10(b) was marked by an arrow to show the decohesion of the intermetallic phase, which represented an interface between two phases of the eutectic

structure:  $\alpha$ -Mg and  $\beta$ -Mg<sub>17</sub>Al<sub>12</sub> intermetallic compound with connecting bridges through both phases. Similar observations on the decohesion of the intermetallic phase were also reported by Czerwinski *et al.* [7] and Zhang *et al.* [9] for thixomolded AZ91D alloy. The fracture surface of AM60B specimen illustrated in Figure 4.10(c) and (d) revealed some more ductile features, which were characterized by the presence of more dimple-like features. This corresponded well to the higher ductility of AM60B alloy (Figure 4.7(c)), in comparison with AZ91D alloy which showed more brittle-like failure as shown in Figure 4.10(a,b).

The side view in the area near the fracture surfaces of AZ91D and AM60B specimens, as shown in Figure 4.11(a) and (b), further corroborated the above fractographic observations. It is seen from Figure 4.11 that the fracture occurred predominantly through the eutectic structure that surrounded the primary  $\alpha$ -Mg grains in both alloys. Some obvious secondary cracks (marked by the arrows in Figure 4.11(a)) occurred along the eutectic structure containing intermetallic  $\beta$ -Mg<sub>17</sub>Al<sub>12</sub> phase. The crack initiation and subsequent propagation in AZ91D alloy would be closely associated with the decohesion of the eutectic structure which was characterized by relatively low ductility due to the presence of hard and brittle  $\beta$ -Mg<sub>17</sub>Al<sub>12</sub> intermetallic phase. Thus, secondary cracks in the vicinity of fracture surfaces were clearly observed along the eutectic structure in the AZ91D alloy.

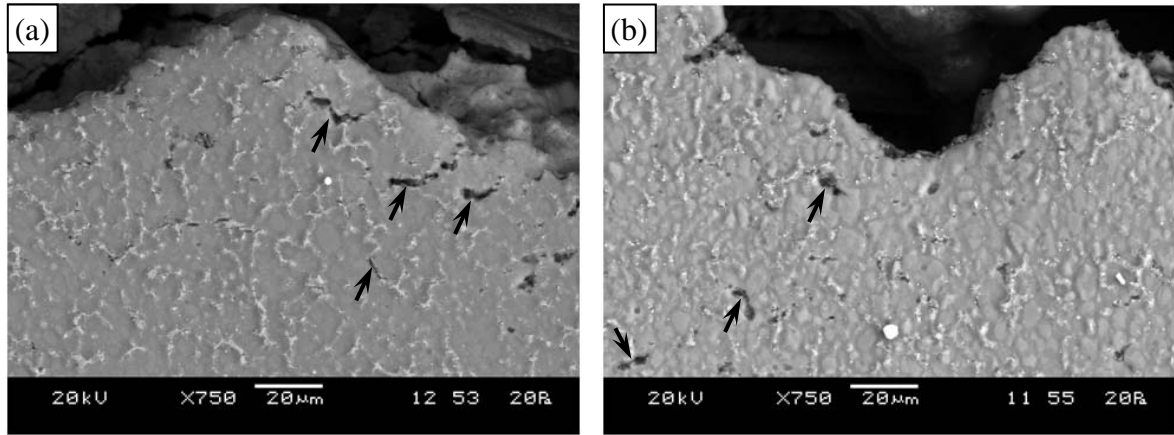


Figure 4.11: Typical SEM images showing the side surface of tensile tested (a) AZ91D alloy, and (b) AM60B alloy.

As shown in Table 4.1, in the AM60B alloy more primary  $\alpha$  phase which was relatively more ductile and less amount of intermetallic  $\beta$ - $\text{Mg}_{17}\text{Al}_{12}$  phase within the eutectic structure were present due to the lower content of aluminum. As a result, the tendency of the secondary cracking along the eutectic structure became lower, as seen in Figure 4.11(b). Indeed, no obvious secondary cracks in the neighbourhood of the fracture surface were observed. Occasionally, microvoids appeared to nucleate at the primary  $\alpha$ -Mg or  $\alpha$ - $\beta$  interface near the fracture surface of AM60B alloy, as marked by arrows in Figure 4.11(b). Similar observations were also reported by Nandy *et al.* [11] for their blended thixomolded Mg-Al alloy. A considerable amount of energy would be consumed in the process of the formation of microvoids and subsequently coalescence of microvoids under the tensile stress [107], exhibiting more ductile fracture. Therefore, these observations indicated that the higher ductility of AM60B alloy would be expected in comparison with the AZ91D alloy, as shown in Figure 4.7(c).

## **CHAPTER 5**

### **CYCLIC DEFORMATION AND TWINNING IN SEMI-SOLID PROCESSED MAGNESIUM ALLOYS**

Strain-controlled cyclic deformation tests were performed as described in Chapter 3 on semi-solid processed (thixomolded) AZ91D and AM60B alloys. Fatigue life, fatigue parameters, and cyclic deformation characteristics of these alloys were evaluated and discussed in this chapter.

#### **5.1 Cyclic Deformation Response**

Depending on the initial state and test condition, a metal may undergo cyclic hardening, cyclic softening, or remain cyclically stable. Under a total strain control condition, cyclic hardening would be reflected by an increasing peak stress (or stress amplitude) with increasing number of cycles, while cyclic softening would be characterized by decreasing stress amplitude and increasing plastic strain amplitude which would lead to early failure [66]. Figure 5.1(a) and (b) shows the stress amplitude and plastic strain amplitude as a function of the number of cycles at different total strain amplitudes for thixomolded AZ91D alloy, respectively. It is observed that, as the total strain amplitude increased, both the stress amplitude and the plastic strain amplitude increased, and the fatigue life decreased. At higher strain amplitudes (1.0% and 1.2%) the alloy showed cyclic hardening characteristics which also corresponded to decreasing plastic strain amplitude until failure. At intermediate strain

amplitudes (0.3%-0.8%) the alloy showed initially cyclic softening, followed by cyclic hardening for the remaining life. At lower strain amplitudes of 0.1% and 0.2%, the stress amplitude and plastic strain amplitude remained almost constant.

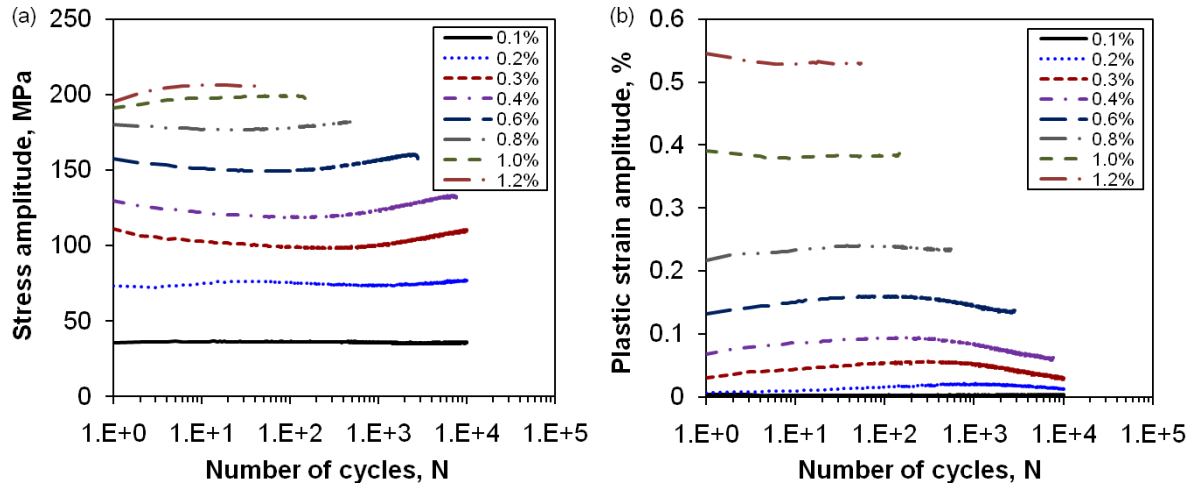


Figure 5.1: Variation of (a) stress amplitude, and (b) plastic strain amplitude with the number of cycles at different total strain amplitudes for thixomolded AZ91D alloy.

Similar results on the cyclic hardening/softening for thixomolded AM60B alloy were obtained, as seen from Figure 5.2(a) showing the evolution of stress amplitude with respect to the number of cycles at different strain amplitudes on a semi-log scale. It is seen that as the strain amplitude increased, the stress amplitude increased. At higher strain amplitudes (1.2%, 1.0%) the alloy showed initial cyclic hardening effect. At strain amplitude of 0.8%, during the early cycling (up to ~10 cycles) the alloy remained cyclically stable which was followed by a little cyclic hardening until failure. At strain amplitudes between 0.6 and 0.2%, the alloy exhibited initially slight cyclic softening followed by cyclic hardening for the remaining life. These changes corresponded well to the evolution of the plastic strain amplitude for

thixomolded AM60B alloy, as shown in Figure 5.2(b). As the total strain amplitude increased, the plastic strain amplitude increased and the fatigue life of the material decreased as well. At total strain amplitudes of 0.2% to 0.6%, the plastic strain amplitude increased to a maximum then it decreased with increasing number of cycles. At a strain amplitude of 0.8% for the early ( $\sim 10$ ) cycles the plastic strain amplitude remained almost constant and then decreased as cyclic deformation continued. At higher total strain amplitudes (1.0%, 1.2%), the alloy basically exhibited cyclic hardening with decreasing plastic strain amplitude for initial stage after which the plastic strain amplitude remained nearly constant until failure.

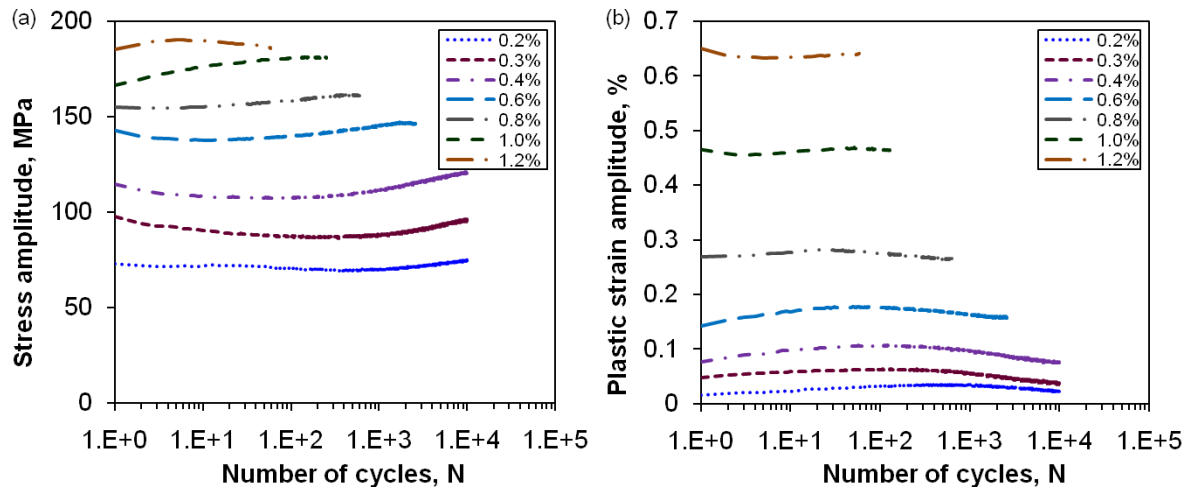


Figure 5.2: Variation of (a) stress amplitude, and (b) plastic strain amplitude with the number of cycles at different total strain amplitudes for thixomolded AM60B alloy.

Similar changes in the stress amplitude and plastic strain amplitude have also been reported for extruded AZ31 alloy [68, 69] and AM30 alloy [73], for conventional and die cast AZ91 alloy [29, 35], and superalloy Nimoc PE-16 [108]. Cyclic hardening effect was observed by Chen *et al.* [29] for a conventional die cast AZ91 alloy at total strain amplitudes ranging

0.3%-1.0%. Liu *et al.* observed cyclic strain hardening in a HPDC AZ91 alloy with and without solution (T4) treatment at strain levels between 0.25%-1.5% [35], while for an extruded AM50 alloy [36] cyclic hardening occurred at higher strain levels and cyclic softening occurred at lower strain levels. Also Xu *et al.* [109] observed cyclic hardening effect in the fine grained HPDC AM50, AE44, AJ62A alloys and cyclic softening effect in the coarse grained LPDC AM50 alloy. The observed hardening/softening behavior in the present study was in agreement with the above reports.

The variation of the stress response with the number of cycles was an important characteristic in the LCF [75]. Such a cyclic stress response depended mainly on two important factors including the mechanical and/or cyclic stability of the intrinsic microstructural features during fully reversed cyclic straining and an intrinsic ability of the microstructure to distribute the plastic strain over the entire volume of the specimen/material [75]. The cyclic hardening could be generally attributed to the increase of the dislocation density as a result of dislocation interaction during microplastic deformation, as well as interaction between dislocations and precipitates including  $\beta$ -Mg<sub>17</sub>Al<sub>12</sub> and Al-Mn particles. It was difficult for these incoherent precipitates to be cut by dislocations, thus they became effective barriers to impede dislocation motion. At the high total strain amplitudes the hardening effect from the precipitates seemed to be more significant in the present study. The cyclic softening observed at the initial cycles at the lower strain amplitudes was probably associated with dislocation annihilation and rearrangement [75]. When the hardening effect was balanced by the softening effect, the stable cyclic stress response would be attained as seen at lower total strain amplitudes.



## 5.2 Hysteresis Loops

The hysteresis loops for the first cycle and mid-life cycle at total strain amplitude of 1.2% is shown in Figure 5.3(a) and (b) for thixomolded alloys AZ91D and AM60B, respectively. Compared with the first loop, the mid-life loop showed a higher peak stress reflecting the occurrence of cyclic hardening, which corresponded well to the stress response shown in Figure 5.1(a) and 5.2(a).

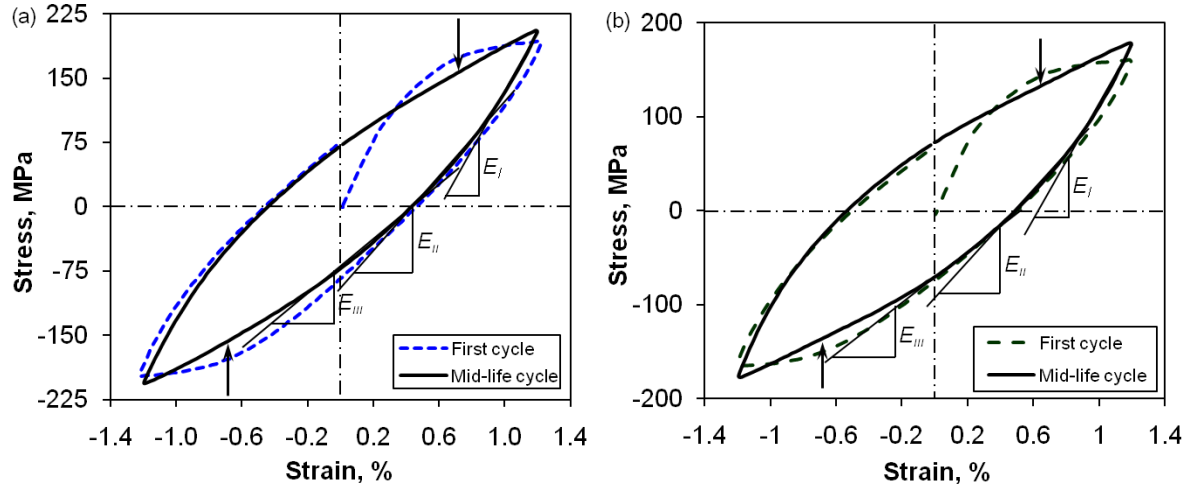
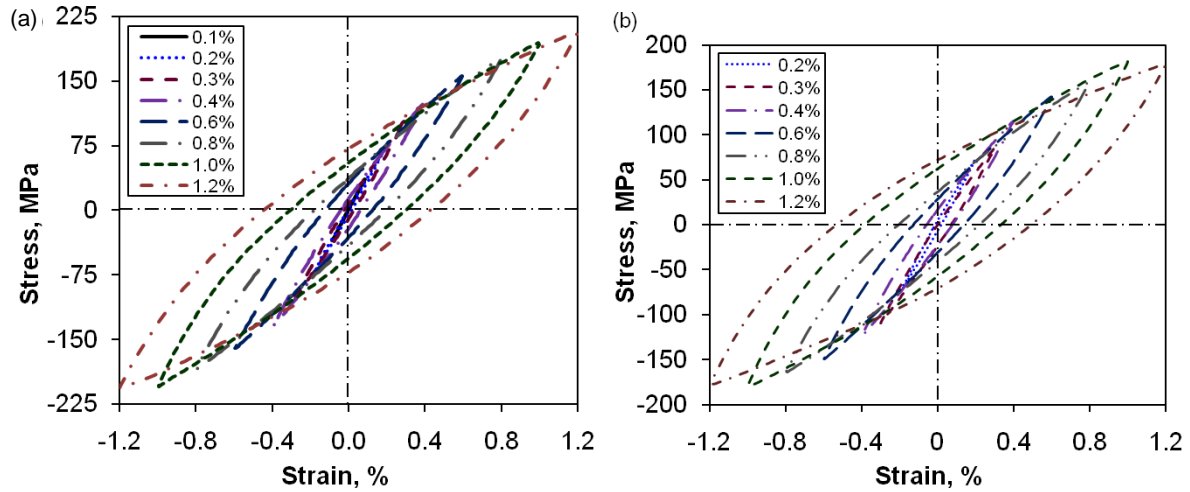


Figure 5.3: Typical hysteresis loops of the first and mid-life cycles at total strain amplitude of 1.2% for thixomolded Mg alloy (a) AZ91D and (b) AM60B.

It can be seen that the mid-life loop showed slight concavity as indicated by arrows before the reversal points in both the tensile and compressive phases, and the linear unloading portions immediately after the reversal points were quite small, which looked unlike the typical hysteresis loops in most fcc metals, and were replaced by the majority of non-linear change (i.e., with different moduli of  $E_I$ ,  $E_{II}$ ,  $E_{III}$  as shown in Figure 5.3(a) and (b)). It is seen

that the hysteresis loops at the beginning of the fatigue life and at the mid-life were basically symmetrical in the present thixomolded Mg alloys, in contrast with those of extruded Mg alloys where the hysteresis loops appeared asymmetrical when the cyclic loading was applied in the extrusion direction [67-69, 73, 75]. Similar observations on the symmetrical hysteresis loops have been reported for die cast AZ91 [35, 36, 110] and AM50 [78] alloys in the fully reversed strain-controlled fatigue tests.



*Figure 5.4: Typical hysteresis loops of the mid-life cycles at different total strain amplitudes for thixomolded Mg alloy (a) AZ91D and (b) AM60B.*

Figure 5.4(a) and (b) show the effect of strain amplitudes on the shape of hysteresis loops at the mid-life of thixomolded AZ91D and AM60B alloys, respectively. It is seen that the loops became bigger in both height and width with increasing total strain amplitude and the loops exhibited a clockwise rotation. At a given strain amplitude applied, the hysteresis loop of the thixomolded AM60B alloy was observed to be wider than that of the thixomolded AZ91D alloy, indicating that a larger plastic strain amplitude was present in the AM60B alloy. This

corresponded well to the higher ductility and lower yield strength (Figure 4.7). Caceres *et al.* [89] and Mann *et al.* [111] observed large symmetrical hysteresis loops under cyclic loading-unloading for their die cast AZ91 and Mg-Zn alloys, respectively, and showed that the anelastic effect developed gradually with increasing plastic strain, reaching a maximum at a strain of about 1.2%.

### **5.3 Change of Elastic Modulus during Cyclic Deformation**

The clockwise rotation of the hysteresis loops with increasing total strain amplitude shown in Figure 5.4 indeed revealed that the slope after the reversal points, i.e., elastic modulus, was different at different stress-strain levels. Such a response to the stress-strain without involving plastic deformation posed a complex issue to engineers who tried to design structural components on the assumption of a constant value of the elastic modulus [111]. The magnitude of the pseudoelastic effect was observed to be associated with both the applied total strain amplitude and the ensuing plastic strain amplitude in the present study. The variation of elastic modulus during cyclic deformation of the thixomolded AZ91D alloy was evaluated and shown in Figure 5.5(a) and (b) where the moduli of elasticity in the ascending/loading and descending/unloading phases (i.e.,  $E_l$  in both loading and unloading phases in Figure 5.3) were plotted, respectively. It is seen that both loading and unloading moduli decreased with increasing total strain amplitudes and both of them exhibited a similar trend. The similarity in the loading and unloading moduli reflected the relatively symmetrical hysteresis loops in tension and compression, as discussed in the previous section. At lower strain amplitudes (0.1%, 0.2%) both loading and unloading moduli remained constant

throughout the fatigue life within the experimental scatter, which corresponded well to the constant stress amplitude shown in Figure 5.1(a). At intermediate strain amplitudes (0.3%-0.6%), both loading and unloading moduli remained nearly constant for initial cycles and then increased for the remaining fatigue life. At higher strain amplitudes between 0.8%-1.2%, where the difference in the magnitude of moduli was small, both loading and unloading moduli kept increasing monotonically in the entire cyclic deformation process until failure, and the slope of the moduli versus the number of cycles in the semi-log scale became steeper.

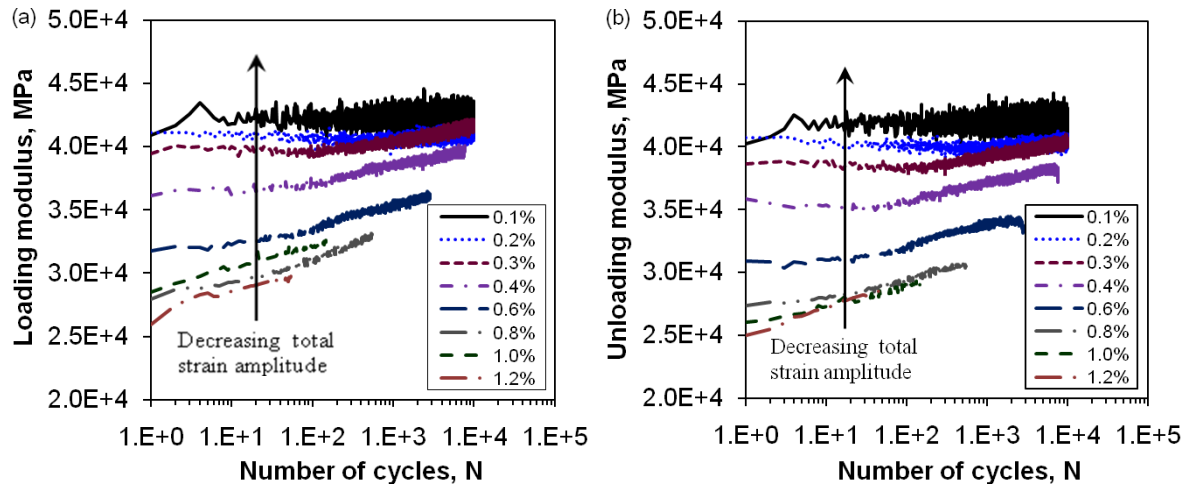


Figure 5.5: Variation of (a) loading modulus, and (b) unloading modulus with the number of cycles during cyclic deformation at different strain amplitudes for thixomolded AZ91D alloy.

Similar change of the moduli of elasticity in the loading and unloading phases with the number of cycles was observed for thixomolded AM60B alloy, as shown in Figure 5.6(a) and (b), respectively. Both loading and unloading moduli decreased with increasing total strain amplitudes and both of them exhibited a similar trend. At a lower strain amplitude of 0.2% both loading and unloading moduli slightly decreased within the initial 20~30 cycles after

which they remained almost constant throughout the fatigue process within the experimental scatter. Loading modulus remained basically constant and unloading modulus slightly decreased for the initial 20~30 cycles at the strain amplitudes of 0.3% and 0.4%, and then both loading and unloading moduli increased for the remaining fatigue life. At higher strain amplitudes between 0.6%-1.2%, both loading and unloading moduli kept increasing monotonically in the entire cyclic deformation process until failure, and the slope of the moduli versus the number of cycles in the semi-log scale became steeper with increasing strain amplitude (Figure 5.6), indicating stronger non-linear or pseudoelastic characteristics.

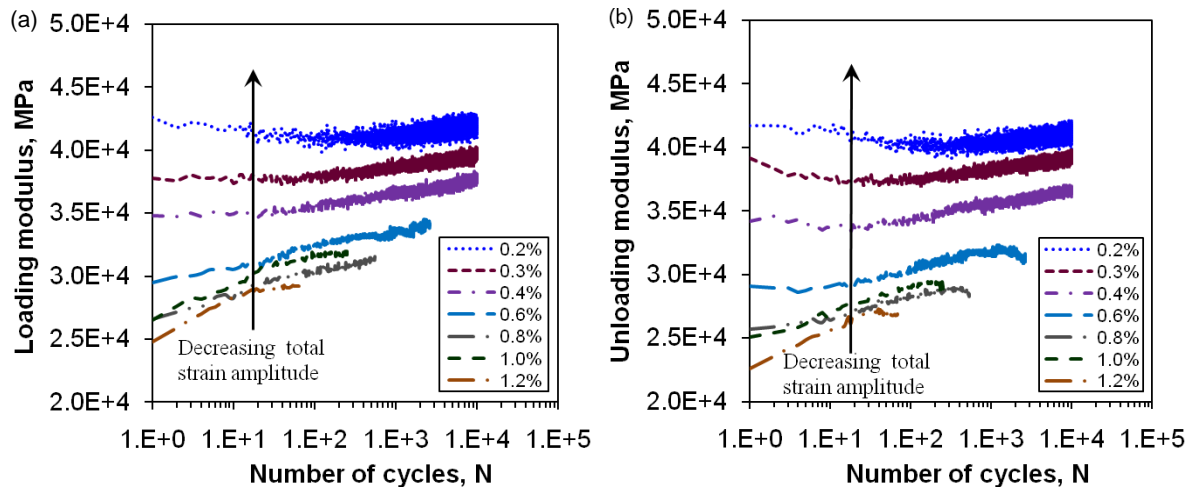


Figure 5.6: Variation of (a) loading modulus, and (b) unloading modulus with the number of cycles during cyclic deformation at different strain amplitudes for thixomolded AM60B alloy.

## 5.4 Pseudoelasticity

Caceres *et al.* [89] came up with an idea that twinning and not dislocation plasticity was mainly responsible for the shape of hysteresis loops and showed that the anelastic effect

developed gradually with increasing plastic strain, reaching a maximum at a strain of about 1-2% for a cast AZ91 alloy. In the present work, the elastic modulus was observed to be stress-dependent (Figure 5.5 and 5.6) due to the presence of nonlinear elastic effects (Figure 5.3(a) and (b)). Any non-linearity in the unloading curve could be referred to as pseudoelasticity. Pseudoelasticity could be related to several origins such as reversible movement of dislocations, twinning, and stress-induced phase transformation. Twinning pseudoelasticity was caused by the reversible movement of twin boundaries, or detwinning. The position of twins in the deformed state was not stable, and a driving force could cause them to return back upon unloading [67-69, 73, 75, 76, 89].

Caceres *et al.* [89] examined the change of elastic modulus in their cast AZ91 Mg alloy using tensile loading-unloading procedures, and observed that with increasing plastic strain up to 1-2% the elastic modulus decreased drastically, i.e., the anelastic or pseudoelastic strain could cause a decrease of up to 70% in the elastic modulus of the alloy due to the partial reversal of twins upon unloading. The decrease of the elastic modulus with increasing strain amplitude, observed in the present investigation (Figure 5.5 and 5.6), was in agreement with the results reported in [68, 69, 73, 89].

## **5.5 Fatigue Life and LCF parameters**

The plots of total strain amplitude vs. the number of cycles to failure for the thixomolded Mg alloys AZ91D and AM60B are presented in Figure 5.7(a) and (b). The experimental data available in the literature in different processing conditions, including those for a solution

treated die cast AZ91E alloy [33] and a die cast AZ91 alloy with or without solution treatment [34], are also plotted in the Figure 5.7(a) for comparison with thixomolded AZ91D alloy. Similarly, Figure 5.7(b) presents the fatigue life data for the thixomolded AM60B alloy, in comparison with that for the same material in the die cast process published earlier [27, 30]. Run-outs are indicated by arrows at or over  $10^7$  cycles. All alloys showed a similar trend of increasing fatigue life with decreasing strain amplitude.

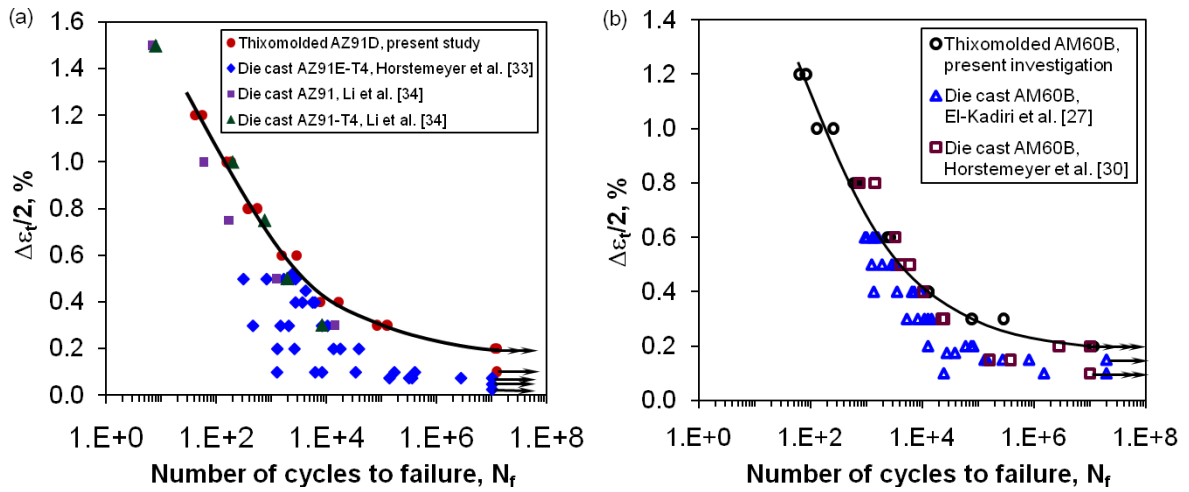


Figure 5.7: Fatigue lifetime in comparison with that of die cast Mg alloys reported in the literature for the thixomolded Mg alloys (a) AZ91D and (b) AM60B.

It is visible from Figure 5.7(a) that the thixomolded AZ91D alloy had a longer fatigue life with a relatively smaller experimental scatter compared to die cast AZ91 alloy [34]. Though at higher strain amplitudes (0.6-1.0%) the solution treated die cast alloy [33] showed an equivalent fatigue life, the semi-solid thixomolded alloy exhibited a higher fatigue resistance at lower strain amplitudes (below ~0.6%). For instance, at total strain amplitude of 0.3%, the thixomolded samples lasted for  $\sim 10^5$  cycles which was about 6-8 times longer than its die

cast counterpart. Similarly, both thixomolded samples tested at total strain amplitude of 0.2% in this study remained unfailed even after  $10^7$  cycles, while the solution treated AZ91E-T4 samples failed much earlier than  $10^5$  cycles (Failure of the solution treated AZ91E-T4 samples occurred even at total strain amplitude of 0.1% for most samples with a big scatter as well). It is seen from Figure 5.7(b) that the fatigue life of the semi-solid thixomolded AM60B alloy was equivalent to that of die cast AM60B alloy reported by Horstemeyr *et al.* [30] but longer than that of El Kadiri *et al.* [27], especially at the lower strain amplitudes. In addition, again the fatigue data of the thixomolded AM60B alloy exhibited a relatively smaller experimental scatter due to a smaller amount of porosity present in the thixomolded alloy as reported in Table 4.1. Moore *et al.* [37] also reported a longer fatigue life of the thixomolded AZ91D alloy than that of the vacuum (gravity) die cast counterpart at a given stress level in their stress-controlled high cycle fatigue tests.

Although the phases in the die cast AZ91 and AM60 alloy were similar to those of the thixomolded Mg alloys as studied in present work, the microstructural morphology of this alloy was essentially different. The alloy produced by casting methods [27, 30, 33] had a dendritic grain structure that was prone to large pores and cavities between the dendrite arm spacing in addition to gas porosity. These large pores in the cast alloy were the preferential sites to nucleate cracks as reported in [20, 33]. On the other hand, the thixomolded Mg alloy consisted of globular grain structure as shown in Figure 4.1 that systematically eliminated the pores and cavities in the absence of dendrites (due to the semi-solid non-turbulent casting [40]). The gas porosity would still be present in the present thixomolded AZ91D alloy as reported in Table 4.1. The absence of large pores delayed crack initiation and Al-Mn



particles could act as barriers to crack propagation (to be further discussed later in fractography), leading to an increased fatigue life especially at lower total strain amplitudes. Moore *et al.* [37] also reported that the fatigue behavior was primarily a factor of the size and distribution of the porosity within the specimen, and less a factor of the microstructural constituents when comparing  $S$ - $N$  curves between the thixomolded and Vacuum (gravity) die cast AZ91 alloys, with the former showing a higher fatigue limit.

As described in Eqs. (2) and (3), the total strain amplitude could be obtained by the superposition of elastic strain component known as the Basquin relation and plastic strain component known as Coffin-Manson relation. The obtained elastic, plastic, and total strain amplitudes plotted against the number of reversals to failure based on Eq. (4) (from Chapter 2) are shown in Figure 5.8(a) and (b) for thixomolded alloys AZ91D and AM60B, respectively. Additionally, the thixomolded AZ91D alloy was also compared with that of a vacuum die cast AZ91 alloy [28] in Figure 5.8(a). The values of the strain amplitudes were taken from the mid-life cycles. As seen from these figures, when the (elastic, plastic, and total) strain amplitude was lower, the fatigue lifetime was higher. The curves in all Mg alloys tend toward the plastic curve at large total strain amplitudes and tend toward the elastic curve at small total strain amplitudes. The experimental data obtained over the wide range of strain amplitudes in the present study and those reported in the literature [28] were in good agreement and also followed both the Basquin and Coffin-Manson relationships well.

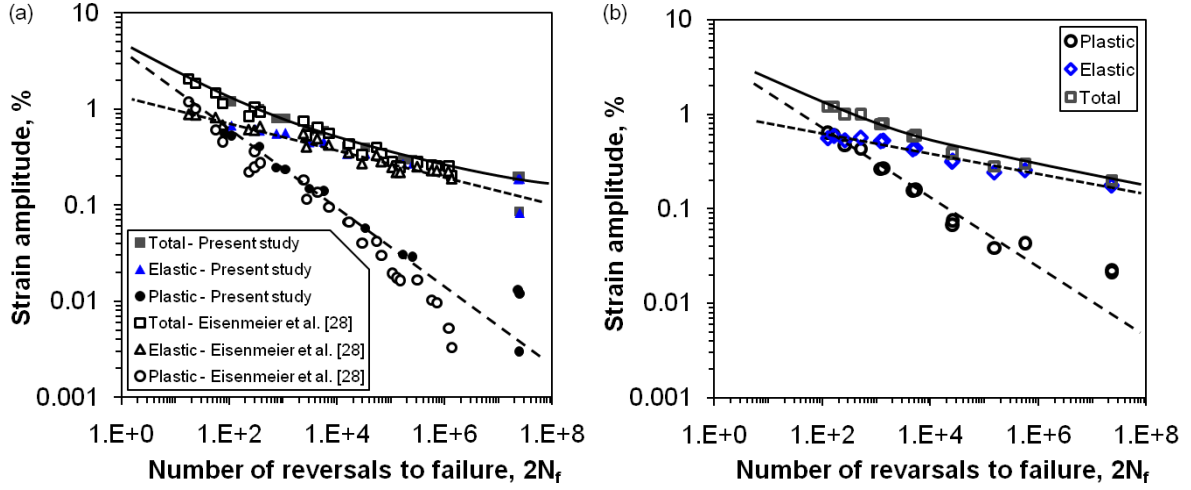


Figure 5.8: Various strain amplitudes vs. number of reversals to failure (a) thixomolded AZ91D alloy in comparison with that of vacuum die cast AZ91 alloy reported in [28], and (b) thixomolded AM60B alloy.

The fatigue parameters which are required to predict the fatigue life of automotive components, have been evaluated using Eqs. (1-3) (from Chapter 2) by plotting  $\log (\Delta \sigma / 2)$  vs.  $\log (\Delta \varepsilon_p / 2)$  representing cyclic stress-strain curves, plus  $\log (\Delta \varepsilon_e / 2)$  vs.  $\log (2N_f)$  and  $\log (\Delta \varepsilon_p / 2)$  vs.  $\log (2N_f)$ . The fatigue parameters evaluated for the thixomolded Mg alloys AZ91D and AM60B are summarized in Table 5.1. The parameters of the present thixomolded Mg alloys are in good agreement with the data reported in the literatures [28, 29, 34-36] for various AZ91 alloys produced by different processes (summarized in Table 2.1).

Table 5.1: Strain-controlled fatigue parameters obtained for the present thixomolded Mg alloys AZ91D and AM60B.

Thixomolded alloys	$n'$	$K'$ , MPa	$\sigma'_f$ , MPa	$b$	$\varepsilon'_f$ , %	$c$
AZ91D	0.23	708	494	-0.12	3.4	-0.39
AM60B	0.23	630	454	-0.11	3.6	-0.37

It is interesting to observe that fatigue parameter values for both the alloys are approximately the same especially fatigue ductility coefficient  $\varepsilon'_f$  and exponents  $c$ , showing that both alloys possess roughly equal fatigue life at higher total strain amplitudes. The higher fatigue strength coefficient  $\sigma'_f$  and cyclic strength coefficient  $K'$  for AZ91D alloy reflect the higher stress amplitude at the same total strain amplitude compared to AM60B alloy, as seen in Figure 5.1(a) and 5.2(a). This may be better seen in Figure 5.9, where nearly the same fatigue life for both semi-solid thixomolded AZ91D and AM60B alloys is seen.

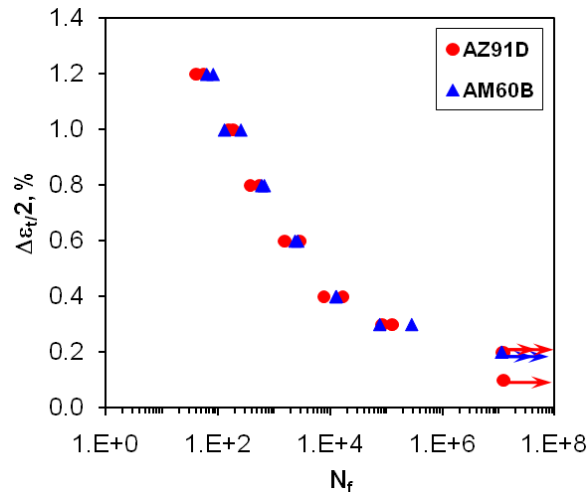


Figure 5.9: Fatigue lifetime for the semi-solid thixomolded AZ91D and AM60B alloys.

## 5.6 Effect of Strain Ratio

To examine the effect of strain ratio on the fatigue characteristics of the thixomolded AZ91D and AM60B alloys, varying strain ratios ( $R_\epsilon$ ) from +0.5 to -2 were applied while keeping other parameters constant, i.e., at a total strain amplitude of 0.6% and strain rate of  $1 \times 10^{-2} \text{ s}^{-1}$ . Two tests were conducted at each strain ratio. The resulting fatigue lives were plotted as a function of strain ratio in Figure 5.10 for both the alloys. It is seen that the fatigue life increased with decreasing strain ratio from  $R_\epsilon = +0.5$  to  $R_\epsilon = -1$ , but the trend slowed down or slightly decreased from  $R_\epsilon = -1$  to  $R_\epsilon = -2$ , with completely reversed strain-controlled test ( $R_\epsilon = -1$ ) showed highest fatigue life in both alloys. Similar effect of strain ratio was reported in the extruded Mg alloys as well [67, 73]. Here, the fatigue life of AM60B alloy is higher than that of AZ91D alloy.

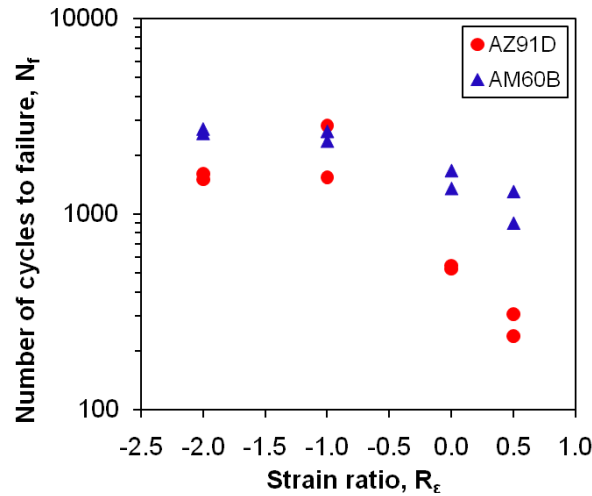


Figure 5.10: Number of cycles to failure vs. strain ratio for the thixomolded AZ91D and AM60B alloys tested at a total strain amplitude of 0.6% and strain rate of  $1 \times 10^{-2} \text{ s}^{-1}$ .

### 5.6.1 Effect on stress amplitudes

The variation of stress amplitude during cyclic deformation at different strain ratios is shown in Figure 5.11(a) and (b) for thixomolded alloys AZ91D and AM60B, respectively. It is of interest to observe that at a strain ratio of  $R_\epsilon = -1$  the stress amplitude was highest, while at other strain ratios the stress amplitude decreased with increasing  $R_\epsilon$  values for both alloys. This could be understood by the definitions of stress amplitude ( $\sigma_a$ ) and strain ratio ( $R_\epsilon$ ).

$$\sigma_a = \frac{\sigma_{\max} - \sigma_{\min}}{2}, \quad (6)$$

$$R_\epsilon = \frac{\epsilon_{\min}}{\epsilon_{\max}}. \quad (7)$$

For the fully-reversed ( $R_\epsilon = -1$ ) test  $\sigma_a$  would be equal to  $\sigma_{\max}$  due to the nearly symmetrical cycling (Figure 5.3) that leads to the highest stress amplitude at that ( $R_\epsilon = -1$ ) strain ratio.

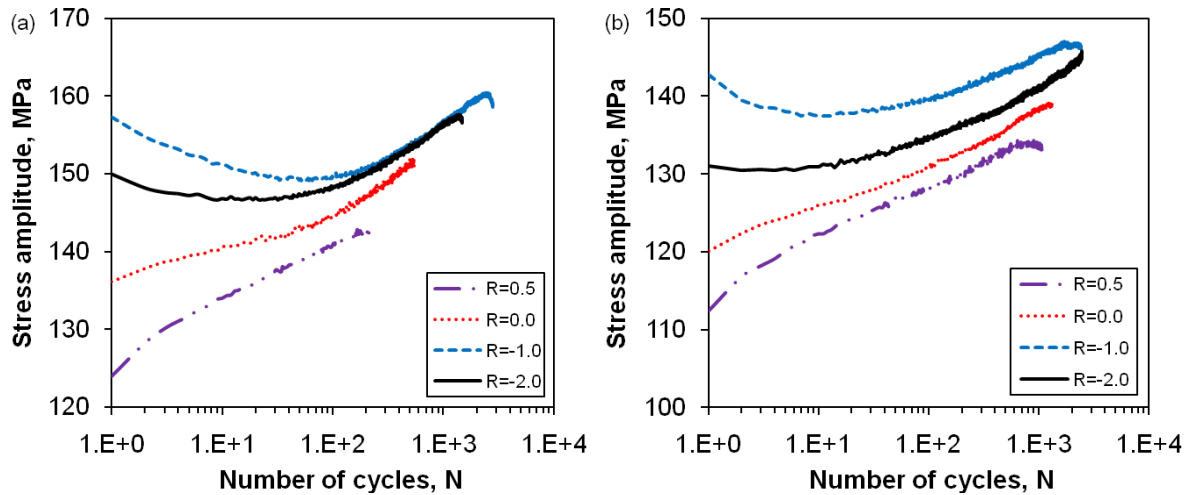


Figure 5.11: Stress amplitude vs. number of cycles for thixomolded alloy (a) AZ91D and (b) AM60B, tested at a total strain amplitude of 0.6% and strain rate of  $1 \times 10^{-2} \text{ s}^{-1}$ .

From Figure 5.11(a), it is seen that for  $R_\epsilon \leq -1$  cyclic softening occurred in the initial ~50 cycles and then cyclic hardening appeared until the test sample failed, while at strain ratios of  $R_\epsilon > -1$  (i.e.,  $R_\epsilon = 0$  and  $0.5$ ) the material underwent only cyclic hardening from the start to failure for AZ91D alloy. Similarly, from Figure 5.11(b), it is also observed that at  $R_\epsilon = -1$  cyclic softening occurred while at  $R_\epsilon = -2$  the stress amplitude was almost constant up to ~10 cycles and after that cyclic hardening occurred until failure at both strain ratios, while at strain ratios of  $R_\epsilon > -1$  the material underwent only cyclic hardening from the outset to failure for AM60B alloy. The extent of cyclic hardening was higher at  $R_\epsilon = 0.5$  and it decreased with decreasing strain ratio in both alloys.

### 5.6.2 *Effect on mean stress*

The change in the strain ratio also led to different mean stresses, as shown in Figure 5.12(a) and (b) for thixomolded AZ91D and AM60B, respectively, where the mean stress was plotted as a function of a normalized cycle ratio ( $N/N_f$ ). The value of mean stress increased with increasing strain ratio and as cyclic deformation progressed the absolute value of the mean stress became smaller due to the mean stress relaxation for both the alloys. The mean stress relaxation mainly occurred in the initial 10-20% of fatigue life, and the mean stresses became more stabilized beyond the mid-life. Similar results were also reported in fatigue behavior of the AM60 [88], AM50 [78] and AZ91E-T6 [87] die cast Mg alloys. It should be noted that only partial mean stress relaxation occurred in both Mg alloys since the mean stress never reached zero in the non-fully reversed  $R_\epsilon \neq -1$  tests even at the end of the fatigue life. It is well known that tensile mean stress had a detrimental effect on the fatigue resistance

by the mechanisms of accelerating the crack initiation and propagation, while the reverse was true for compressive mean stress [112]. This is true since  $R_\epsilon \leq -1$  showed zero to compressive mean stress for both alloys, thus giving a longer fatigue life compared to  $R_\epsilon > -1$  with high tensile mean stresses (Figure 5.12).

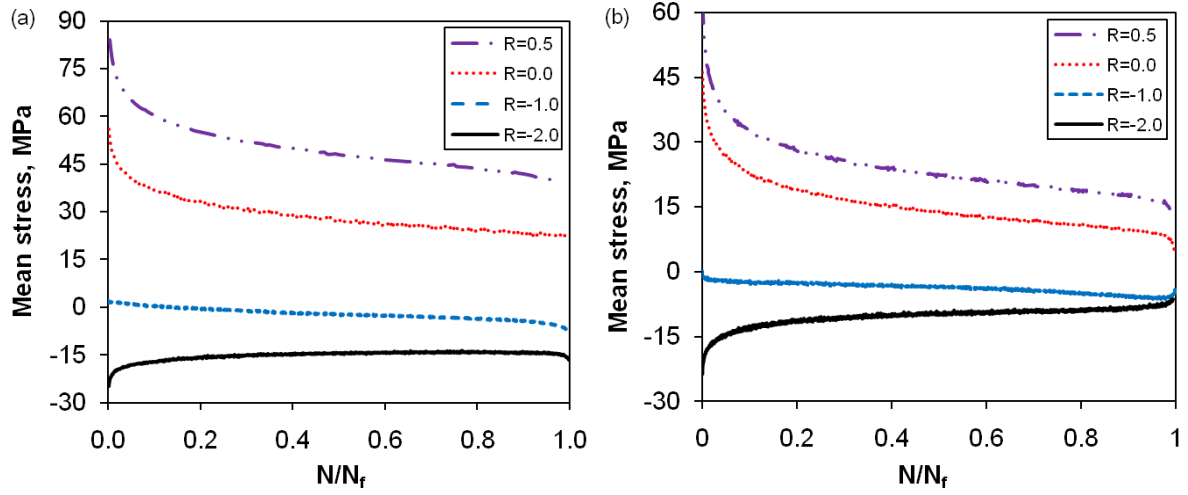


Figure 5.12: Mean stress vs. a normalized cycle ratio ( $N/N_f$ ) at different strain ratios for thixomolded alloy (a) AZ91D and (b) AM60B, tested at total strain amplitude of 0.6% and strain rate of  $1 \times 10^{-2} \text{ s}^{-1}$ .

### 5.6.3 Effect on hysteresis loops

The effect of strain ratio on the first cycle hysteresis loops are shown in Figure 5.13(a) and (b) for thixomolded alloys AZ91D and AM60B, respectively. It is seen from the figures that at all strain ratios the initial tensile phase of the first cycle was synchronized and followed the same path for both alloys. With increasing strain ratio from -2 to 0.5 the maximum/peak tensile stress  $\sigma_{\max}$  increased from  $\sim 125 \text{ MPa}$  to  $\sim 210 \text{ MPa}$  for AZ91D and  $\sim 110 \text{ MPa}$  to  $\sim$

175 MPa for AM60B, with the plastic deformation in the tensile phase becoming much more significant for both alloys. In particular, there was a large amount of plastic deformation occurred in the tensile phase at zero or positive strain ratio ( $R_\epsilon > -1$ ). This was related to the high positive mean strain value. With decreasing strain ratio from 0.5 to -2, the minimum compressive stress  $\sigma_{\min}$  decreased from  $\sim -40$  MPa to  $\sim -175$  MPa for AZ91D and from  $\sim -50$  MPa to  $\sim -150$  MPa for AM60B, where the compressive yielding was not reached at  $R_\epsilon > -1$  for both alloys.

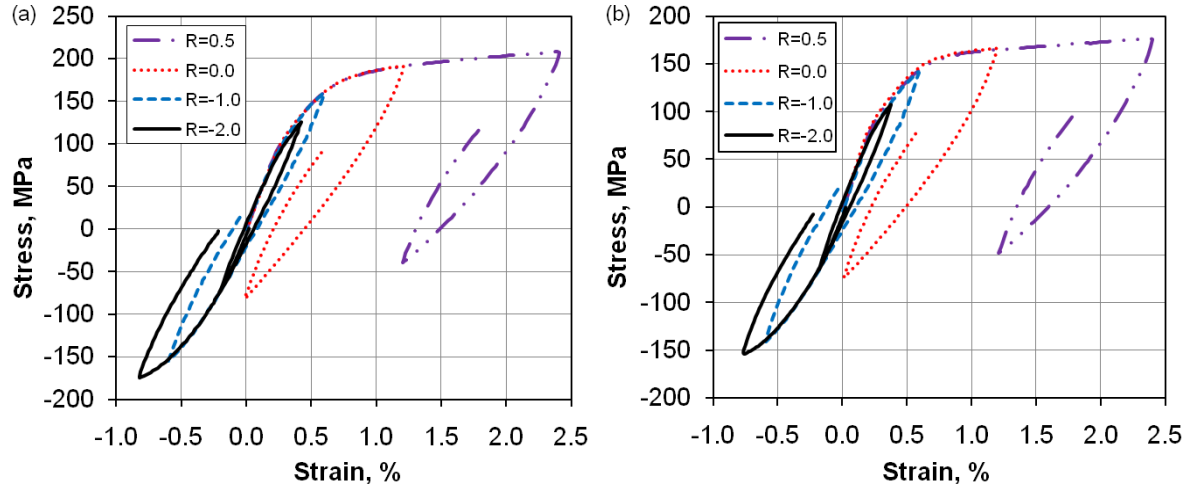


Figure 5.13: First cycle hysteresis loops at different strain ratios for thixomolded alloys (a) AZ91D and (b) AM60B, tested at total strain amplitude of 0.6% and strain rate of  $1 \times 10^{-2} \text{ s}^{-1}$ .

Clearly, in the present study of thixomolded Mg alloys, while the  $R_\epsilon = -1$  test gave basically symmetrical hysteresis loops (Figure 5.3), the tests at other strain ratios resulted in asymmetrical hysteresis loops (Figure 5.13(a) and (b)). However, the initially asymmetrical hysteresis loops became relatively more symmetric in tension and compression at the mid-



life, as shown in Figure 5.14(a) and (b) for thixomolded alloys AZ91D and AM60B, respectively. Such a shift of the hysteresis loops at non-fully reversed strain control (i.e.,  $R_\epsilon \neq -1$  test) was attributed to the mean stress relaxation [66, 88]. However, only partial mean stress relaxation occurred (also seen from Figure 5.12(a) and (b)) since the mid-life hysteresis loops at  $R_\epsilon \neq -1$  tests were not completely symmetric with respect to the zero stress, although more shift was seen in the case of  $R_\epsilon = 0.5$  and 0 (Figure 13(a-b) and 14(a-b)).

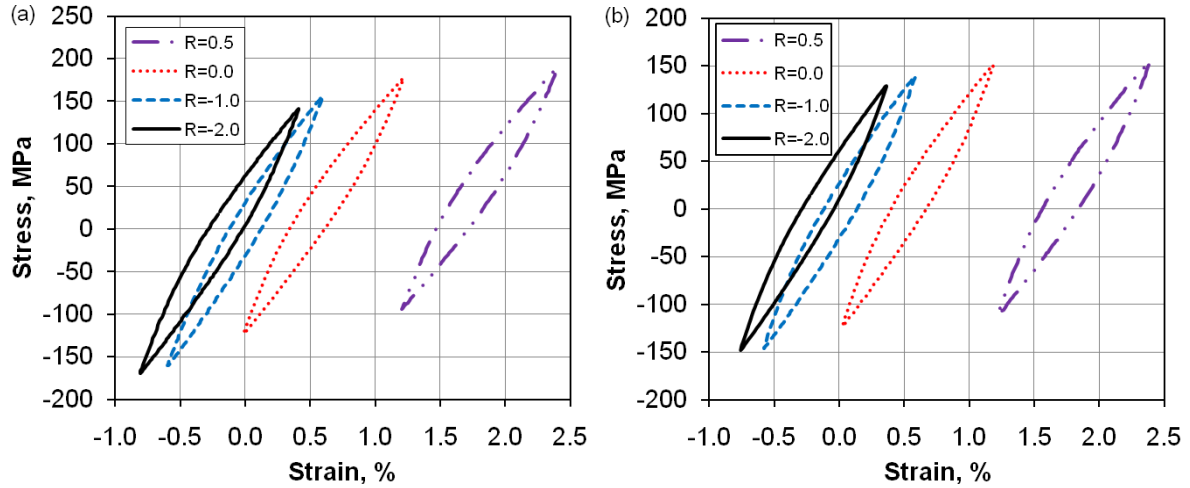
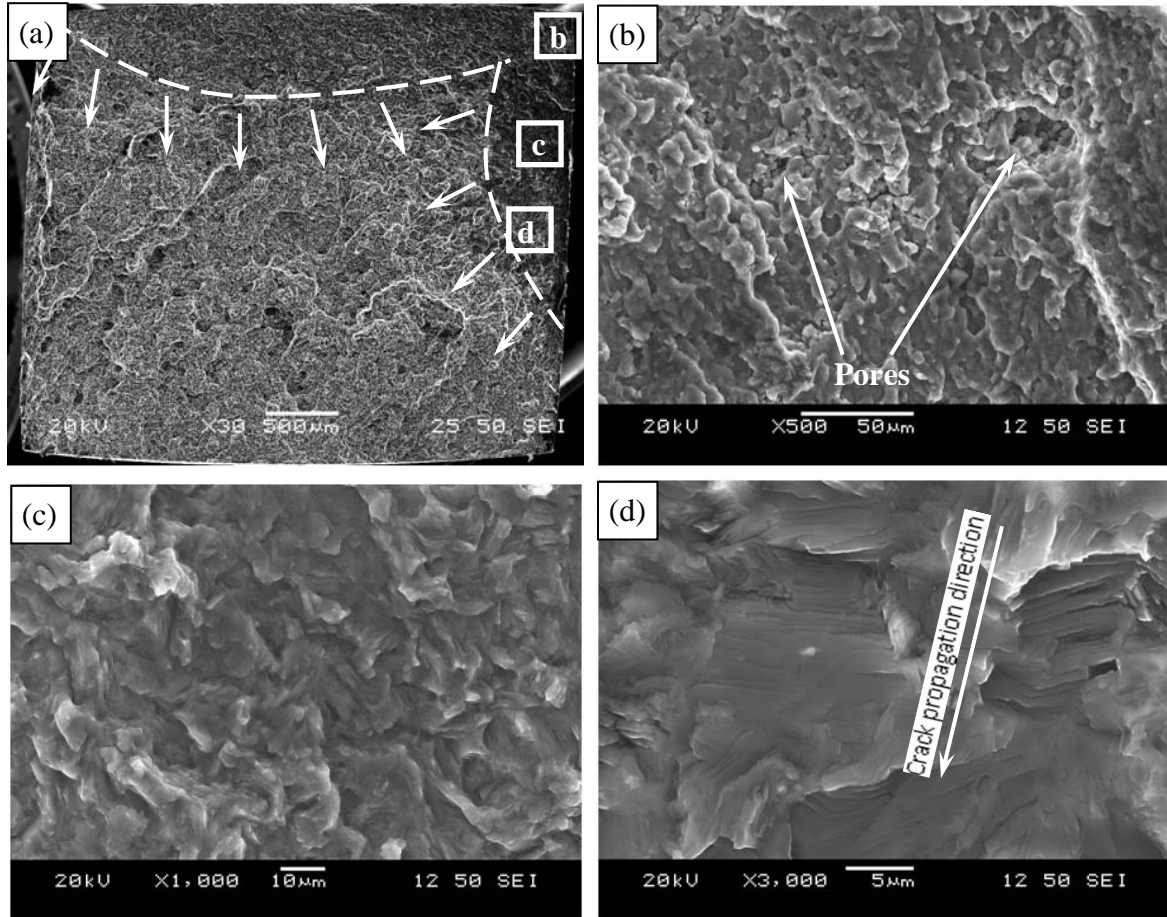


Figure 5.14: Mid-life hysteresis loops at different strain ratios for thixomolded alloys (a) AZ91D and (b) AM60B, tested at total strain amplitude of 0.6% and strain rate of  $1 \times 10^{-2} \text{ s}^{-1}$ .

## 5.7 Fractography

Fracture surfaces of the fatigued specimens were examined using SEM. Figure 5.15(a-d) shows typical images for specimens tested at a total strain amplitude of 0.3% and  $R_\epsilon = -1$  for thixomolded AZ91D alloy.



*Figure 5.15: Typical SEM images showing the fatigue fracture surface of thixomolded AZ91D alloy obtained at a total strain amplitude of 0.3%; (a) overall view at a low magnification, (b) magnified view near the initiation site as marked in (a), (c) magnified view in the crack propagation area as marked in (a), and (d) further magnified view in the crack propagation area as marked in (a).*

It is seen from a low-magnification image (Figure 5.15(a)) that the fracture surface was in general flat with no slant fracture in the final rapid fracture area. Multiple crack initiation from the surface or near surface defects/pores was observed (Figure 5.15(b)), which was possible since the locations of the pores were unknown in the thixomolded or cast alloys.

Figure 5.15(c) and (d) shows the higher magnification SEM images taken in the propagation area as indicated by the boxed regions in Figure 5.15(a). Crack propagation was basically characterized by fatigue striation-like features that was randomly oriented (due to random grain distribution) with each other in conjunction with tear ridges near the initiation site (Figure 5.15(c)). The fatigue striations were perpendicular to the crack propagation direction observed far from crack initiation site (Figure 5.15(d)).

For thixomolded AM60B alloy, Figure 5.16(a,b) and (c,d) shows some typical images of fatigue crack initiation site and propagation zone for the specimen tested at a total strain amplitude of 0.3% and 0.6%, respectively. It is seen from Figure 5.16(a) and (c) that fatigue crack initiated from the specimen surface or near-surface defects, regardless of the applied strain amplitudes. The area of the fatigue crack propagation zone increased with decreasing total strain amplitudes, as indicated by the dashed line on the images. This corresponded to the magnitude of stress amplitude as shown in Figure 5.2(a) and the related number of cycles to failure, which was higher for the lower strain amplitudes (Figure 5.7(b)). As seen from Figure 5.16(b) and (d), fatigue crack propagation was characterized by fatigue striation-like features that were perpendicular to the crack propagation direction. As the total strain amplitude increased the spacing of fatigue striations increased. Each fatigue striation would represent a single stress cycle [66]. As a result, the larger spacing of fatigue striations observed at the higher strain amplitudes corresponded to faster crack propagation, and thus a shorter fatigue lifetime, as shown in Figure 5.7(b).

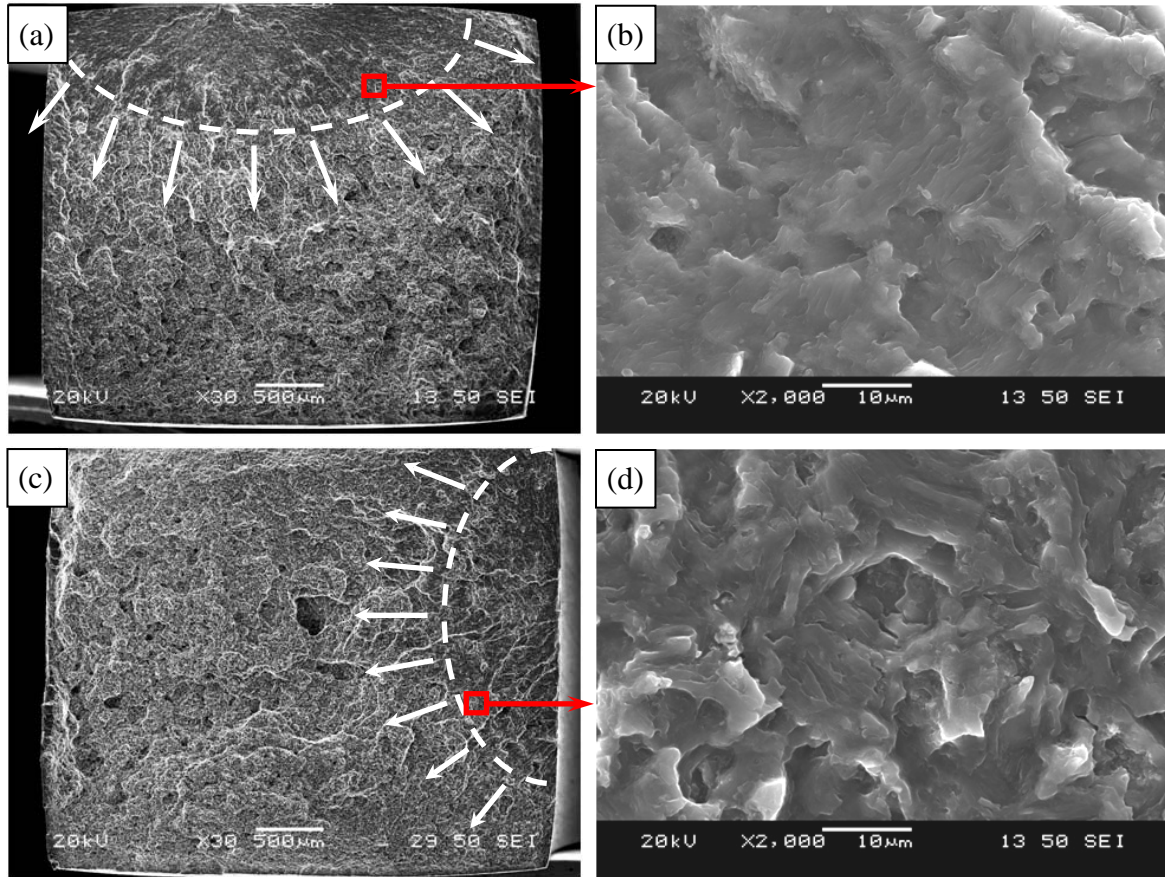


*Figure 5.16: Typical SEM images showing fatigue fracture surfaces of thixomolded AM60B alloy; (a) overall view and (b) magnified view of the boxed region in (a) at a total strain amplitude of 0.3%, (c) overall view and (d) magnified view of the boxed region in (c) at a total strain amplitude of 0.6%.*

The initiated cracks started propagating from different locations, but the final separation occurred when the multiple cracks merged along the weakest path (with more pores). These casting and shrinkage pores provided a driving force for fatigue crack nucleation and propagation due to the presence of stress concentration. Thus, relatively large pores in the alloy served as crack formation sites, while distributed porosity caused a preferential path for fatigue crack propagation. Once the cracks propagated to such a depth that remaining

material was no longer sufficient to withstand the applied cyclic load, the remaining portion/ligament failed like a tensile fracture of the alloy. The present thixomolded Mg alloys had a relatively low porosity ( $\sim 1.25\text{-}1.3\%$ ), leading to a longer fatigue life especially at low strain amplitudes (Figure 5.7(a-b) and 5.9). Significant experimental evidence also showed that fatigue life correlated inversely with the size of such pores or inclusions in both as-cast and wrought materials [33].

To further corroborate the above fractographic observations, side view near the area of fatigue fracture of some thixomolded AZ91D alloys are presented in Figure 5.17(a-c). Some secondary cracks were observed near the fracture surface of the fatigued specimens as seen in Figure 5.17(a) and (b). It seemed that the crack initiated at a free surface through  $\alpha$  phase, but the Al-Mn particle was not cut through during the crack propagation (Figure 5.17(a)). Instead, the crack changed its direction and moved further into the sample. This deflection suggested that Al-Mn particles could act as barriers to fatigue crack propagation. Figure 5.17(b) shows that after reaching a certain depth the crack ran either along the  $\alpha$ - $\beta$  interface or through the primary  $\alpha$ -Mg grains. Figure 5.17(c) shows the side view in the rapid fracture area of a fatigued sample, where the eutectic structure basically dislodged from  $\alpha$  grains. Similarly, side view near the area of fracture surface of thixomolded AM60B alloy is presented in Figure 5.17(d), which is further enlarged in Figure 5.17(e). It is seen that there was an obvious secondary crack generated at the interface between  $\alpha$ - $\beta$  eutectic, and even though it was not generated from the free surface it is wider than (almost double the thickness of the crack in Figure 5.17(b)) that of AZ91D alloy. This may be due to the higher ductility of  $\alpha$ -Mg (due to higher volume fraction) matrix and lower content of eutectic in AM60B alloy.



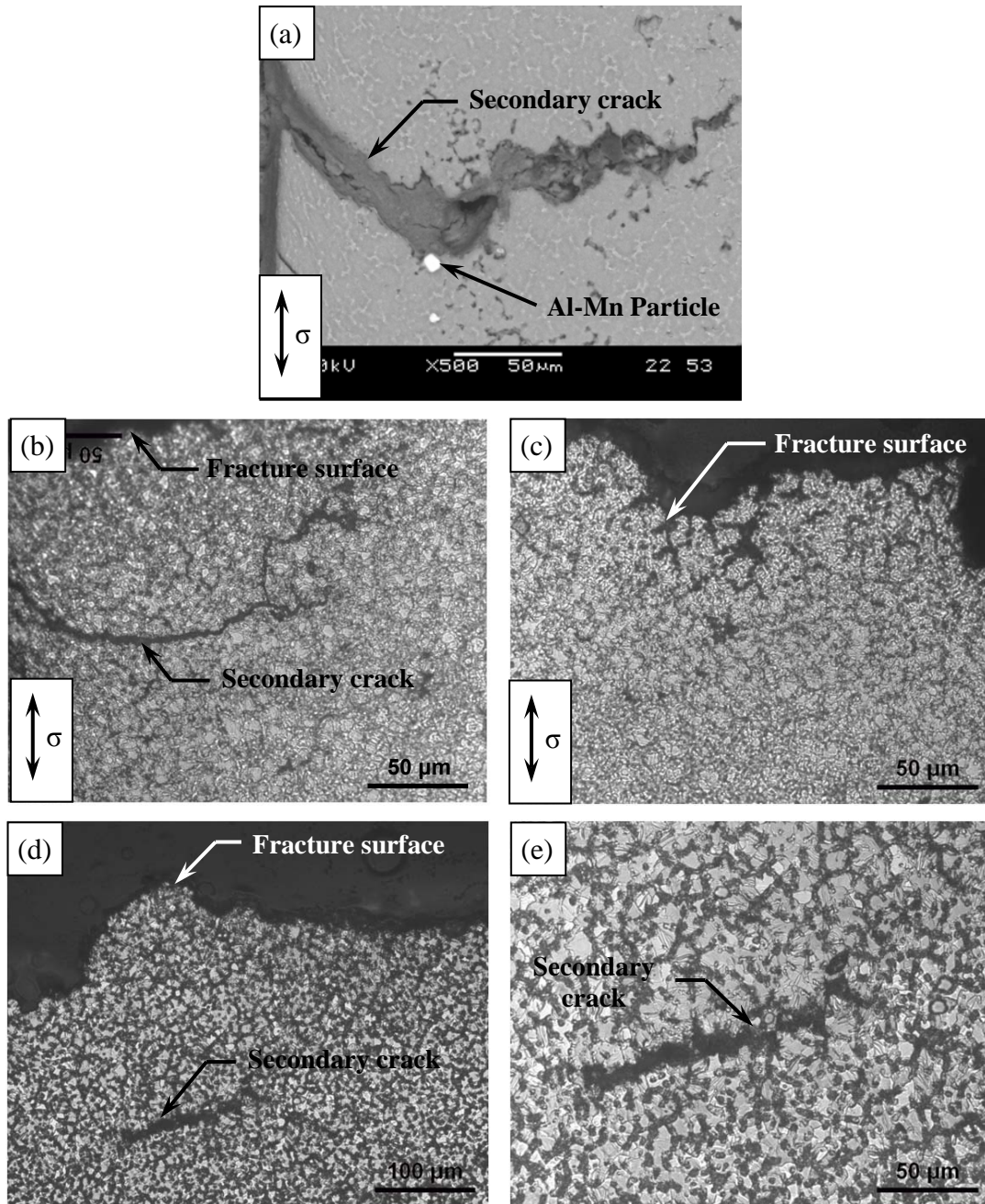


Figure 5.17: Typical micrographs showing the side view near the fatigue fracture surface: (a) SEM image showing an Al-Mn particle acting as a barrier to the secondary crack propagation, (b) OM image showing a secondary crack propagating mainly along  $\alpha$ - $\beta$  interfaces, (c) OM image in the rapid fracture area where the eutectic structure was dislodged from the  $\alpha$  grains in thixomolded AZ91D alloy, and (d) OM image showing formation of wider secondary crack near fracture surface, (e) enlarged view of the wider crack in thixomolded AM60B alloy.

It has been reported that relatively small cracks were unable to prematurely fracture or debond the  $\beta$  phase in front of the crack tip owing to relatively small stress intensity factor and tend to propagate primarily through the  $\alpha$ -Mg grains. On the other hand, when the crack tip stress intensity factor was high enough to fracture/debond the  $\beta$  phase, the failed phase provided a weak material path for the propagating crack tip [30]. It is seen from Figure 5.17(b-e) that the fracture occurred predominantly through the eutectic structure or grain boundary. Even the secondary crack near the fracture surface after a certain depth also followed the similar path as illustrated in Figure 5.17(b,c). The  $\beta$ -Mg<sub>17</sub>Al<sub>12</sub> intermetallic phase in the eutectic structure was known for its higher strength but lower ductility and toughness by lowering the cohesive strength in the grain boundary regions, resulting in a brittle interface between  $\alpha$  and  $\beta$  phases. This brittle interface arose from the incompatibility between the bcc crystal structure of  $\beta$  phase and the hcp crystal structure of  $\alpha$  phase [13], and increased stress concentrations at the grain boundaries [27]. Thus in the present thixomolded AZ91D alloy in the absence of large pores and less amount of porosity, the cracks propagated basically either along  $\alpha$ - $\beta$  interfaces or through the  $\alpha$ -Mg grains to form fatigue striations (Figure 5.15 and 5.16), while Al-Mn particles acted as a barrier.

## **5.8 Formation of Twins during Fatigue**

As mentioned in above sections, twinning played a significant role in the deformation of Mg alloys. At room temperature twinning would help this material to satisfy the Von Mises criterion, which required five independent deformation systems for an arbitrary homogeneous straining. Besides the slip of dislocations with  $\langle c + a \rangle$  Burgers vectors, which

was recognizably a very hard deformation mechanism, twinning was the only active deformation mode that could provide straining along the c-axis at room temperature [75, 113]. It is generally known that principal or extension twinning occurs under tension parallel to the c-axis or under compression perpendicular to the c-axis of hcp crystal structure with the c/a ratio less than 1.732 [114, 115]. In magnesium and its alloys with a c/a ratio of 1.624, it is not surprising to observe some twinning after fatigue tests where both tensile and compressive stresses were applied for a number of times during testing.

To demonstrate the evidence of twinning occurred in the thixomolded Mg alloys, fatigue specimens tested at total strain amplitude of 1.0% and 0.8% were sectioned for AZ91D and AM60B, respectively. The observed typical micrographs are shown in Figure 5.18(a-c) for AZ91D and Figure 5.19(a,b) for AM60B. It is seen that twins formed in the vicinity of the fracture surface. It is of interest to see some wider lenticular twins in Figure 5.18(b) and some needle-like narrow (banded) twins marked by small arrows in Figure 5.18(c) for AZ91D alloy, both can also be seen in Figure 5.19(b) for AM60B alloy. The wider twins (clean inside) were extension twins- $\{10\bar{1}2\}$ , formed when a unit cell was in tension along its c-axis or in compression perpendicular to the c-axis [114, 116, 117]. While the narrow twins (thin, dark inside) were contraction twins- $\{10\bar{1}1\}$ , which were expected to occur when a unit cell was in compression along c-axis [116, 117]. The twinning basically occurred in some favorably oriented large primary  $\alpha$ -Mg grains with respect to the loading axis for both alloys, which could be explained by the decreasing stacking fault energy [22] and lower CRSS (critical resolved shear stress) [26, 74].



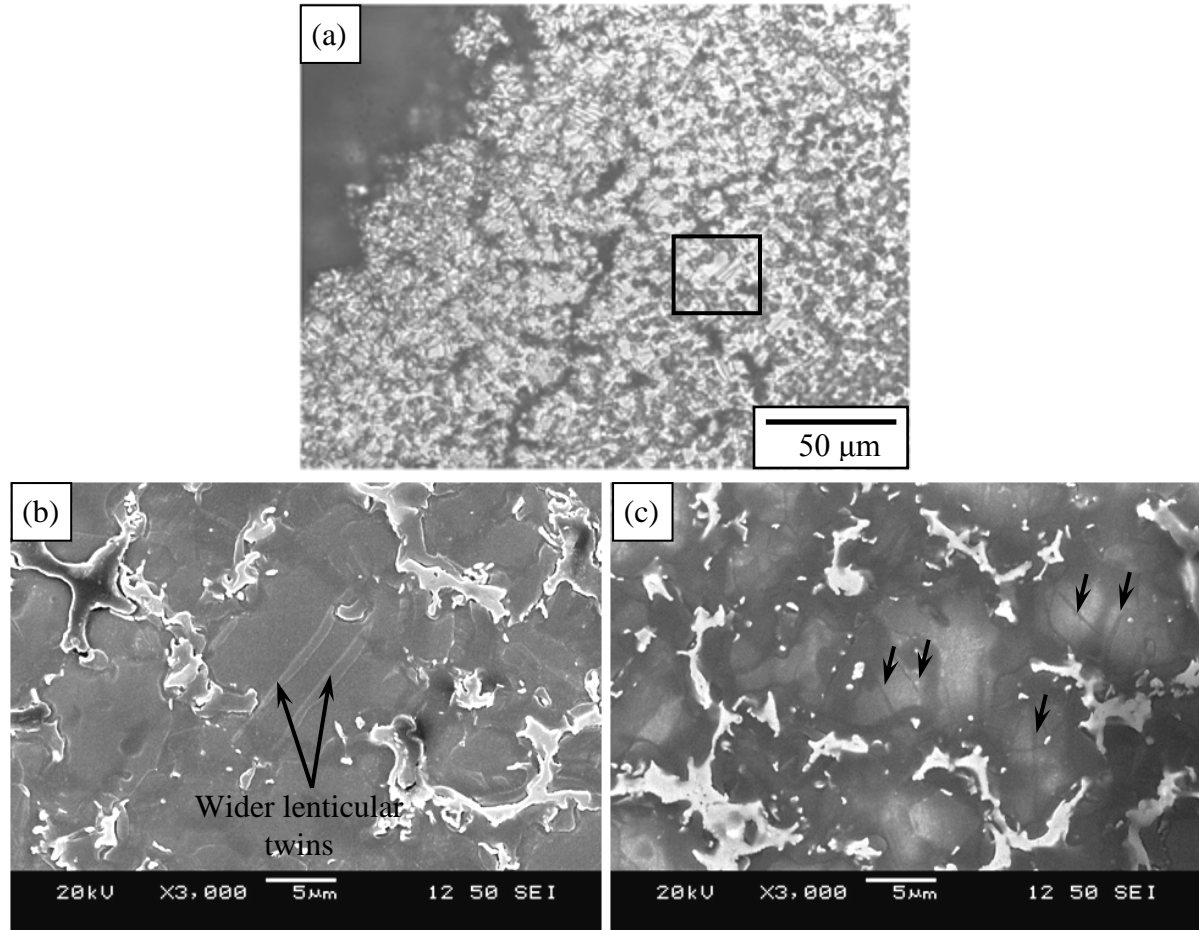


*Figure 5.18: Twinning in thixomolded AZ91D alloy: (a) Low magnification OM image showing twins near the fracture surface, (b) SEM image of the boxed region in (a) at a higher magnification showing wide lenticular extension twins, and (c) another SEM image at a higher magnification showing narrow contraction twins marked by arrows.*

It was expected that the generation of twins in the plastic zone ahead of the crack tip (Figure 5.16) would participate in the formation of fatigue striations in Mg alloy, which has also been pointed out in [67-69, 73-75]. As mentioned earlier, two types of twins were observed as shown in Figure 5.18 and 5.19. It has been reported that the needle-like narrow banded contraction twins would be more detrimental since voids were observed to form largely at

this type of narrow contraction twins that were arrested by grain boundaries [117]. This was considered due to the fact that the narrow contraction twins led to a reduction in cross-sectional area, stress concentrations, and premature transgranular failure in the extruded AM30 Mg alloy [117]. More studies in this aspect are needed to further identify the relationship between the formation of fatigue striations and twinning in Mg alloys.

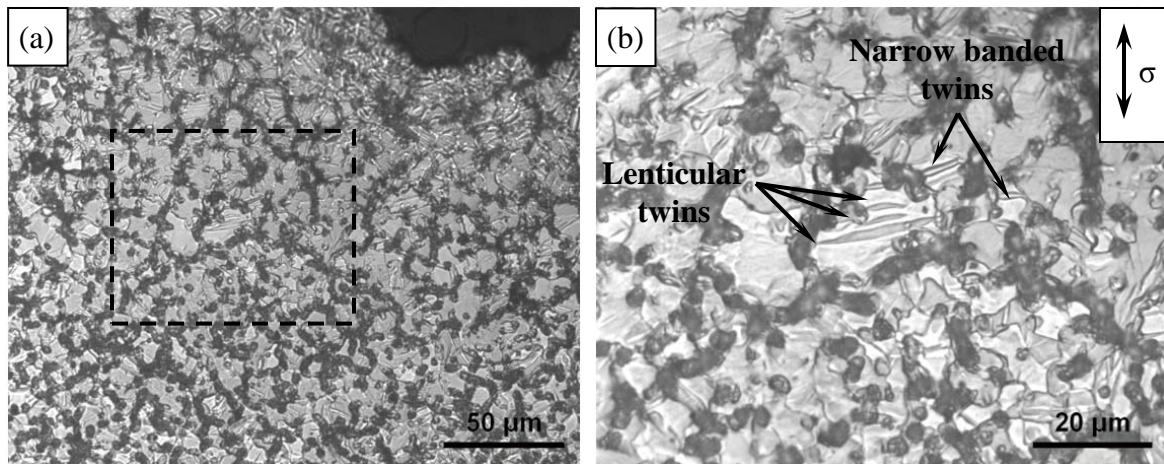


Figure 5.19: Optical microscope images showing (a) the formation of twins near the fracture surface, and (b) a magnified view of the area enclosed by the dashed box in (a) of thixomolded AM60B alloy.

## 5.9 Comparison of Thixomolded and Extruded Mg Alloys

While the present thixomolded Mg alloys exhibited symmetrical hysteresis loops and the extruded Mg alloys (e.g., AM30, AZ31, and ZK60 [67-69, 73-76]) displayed strong asymmetrical/skewed hysteresis loops when the cycling was conducted in the extrusion direction, they were indeed very different from the typical hysteresis loops of fcc metals (e.g., Al and Cu alloys), Figure 5.20 shows clearly such a big difference where the hysteresis

loop of wrought 6061-T6 Al alloy was plotted for the sake of comparison between the extruded and thixomolded Mg alloys.

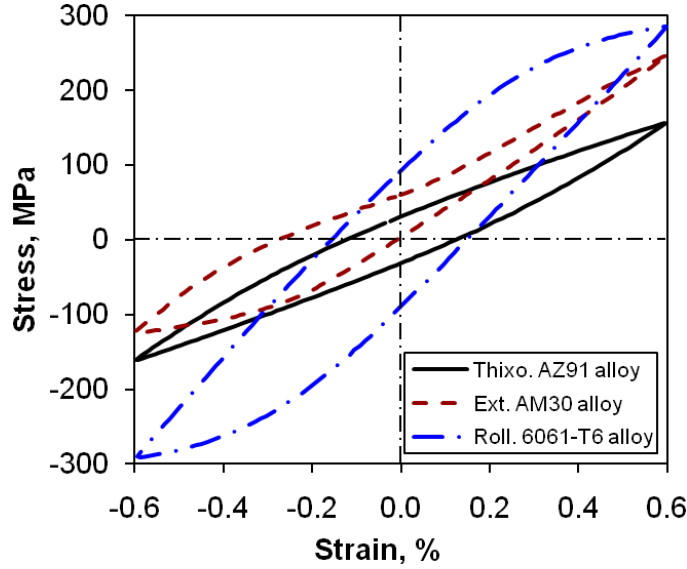


Figure 5.20: Comparing the typical hysteresis loops at mid-life of various alloys with different crystal structures and processing conditions.

The Al alloy with an fcc crystal structure demonstrated nearly perfect symmetry in the hysteresis loop, where the majority of the unloading portion was linear with a constant elastic modulus of  $E_{Al}$  in contrast to the non-linear behavior of the thixomolded Mg alloy (with varying values of  $E$  indicated in Figure 5.3). In comparison with the fcc Al alloy, the extruded AM30 Mg alloy showed both asymmetry and non-linearity. That is, the extruded Mg alloy showed a higher peak stress in the tensile phase, and early yielding occurred in the compressive phase resulting in the skewed compressive portion and lower peak compressive stress [67-69, 73-76]. In the present thixomolded Mg alloy, while the hysteresis loops were basically symmetrical, the non-linearity remained (Figure 5.3).

The symmetry of the tension-compression cycle was usually considered as a result of the dislocation slip-predominant deformation for most materials [118]. However, Caseres *et al.* [89] reported that twinning rather than dislocation plasticity was mainly responsible for the non-linear characteristics of such hysteresis loops, in spite of the relative symmetry in the cast and thixomolded Mg alloys. Likewise, the asymmetrical hysteresis loops with a sigmoidal shape (S-shaped) characteristic (Figure 5.20) in the wrought Mg alloys were mainly attributed to the extensive mechanical twinning [70, 74, 75], which was in turn associated with the crystallographic texture resulting from material forming processes. The presence of texture then gave rise to a difference in twinning initiation stress under tension and compression [110]. Extruded or rolled Mg alloys were strongly textured with the preferred orientation placing the c-axis in most grains perpendicular to the loading axis in the rolling/extrusion direction favorable to twinning under compressive loading [67, 69, 73], while cast or semi-solid processed Mg alloys, such as the current thixomolded alloy, had more randomly oriented grains to the loading axis, leading to the relatively symmetrical hysteresis loops. However, some favorably oriented grains with respect to the loading axis would still be expected to undergo some extent of twinning. This would be the cause for the presence of the non-linearity of the hysteresis loops (Figure 5.3).

## **CHAPTER 6**

### **EFFECT OF HEAT TREATMENT ON THE MECHANICAL BEHAVIOR OF SEMI-SOLID PROCESSED AM60B ALLOY**

Test plates of the thixomolded AM60B alloys were subjected to various heat treatments as also described in Chapter 3. The selected heat treatment procedure is as follows:

- Solution treatment: T4 - 16h @ 413°C; warm water (65°C) quench;
- Artificially aged: T5 - 16h @ 168°C; air cool;
- Solution treated and artificially aged: T6 - 16h @ 413°C; warm water (65°C) quench; followed by 16h @ 168°C; air cool.

The thixomolded alloy was designated as Tx, solution treated alloy was designated as T4, the artificially aged alloy was designated as T5, and the solution treated then artificially aged alloy was designated as T6. Various mechanical tests were carried out on these heat-treated samples and the effect of heat treatment on the obtained properties is discussed in this chapter.

#### **6.1 Effect of Heat Treatment on Microstructure**

Figure 6.1(a-d) shows the optical microscopic images (OM) of AM60B alloy under various heat treated conditions.

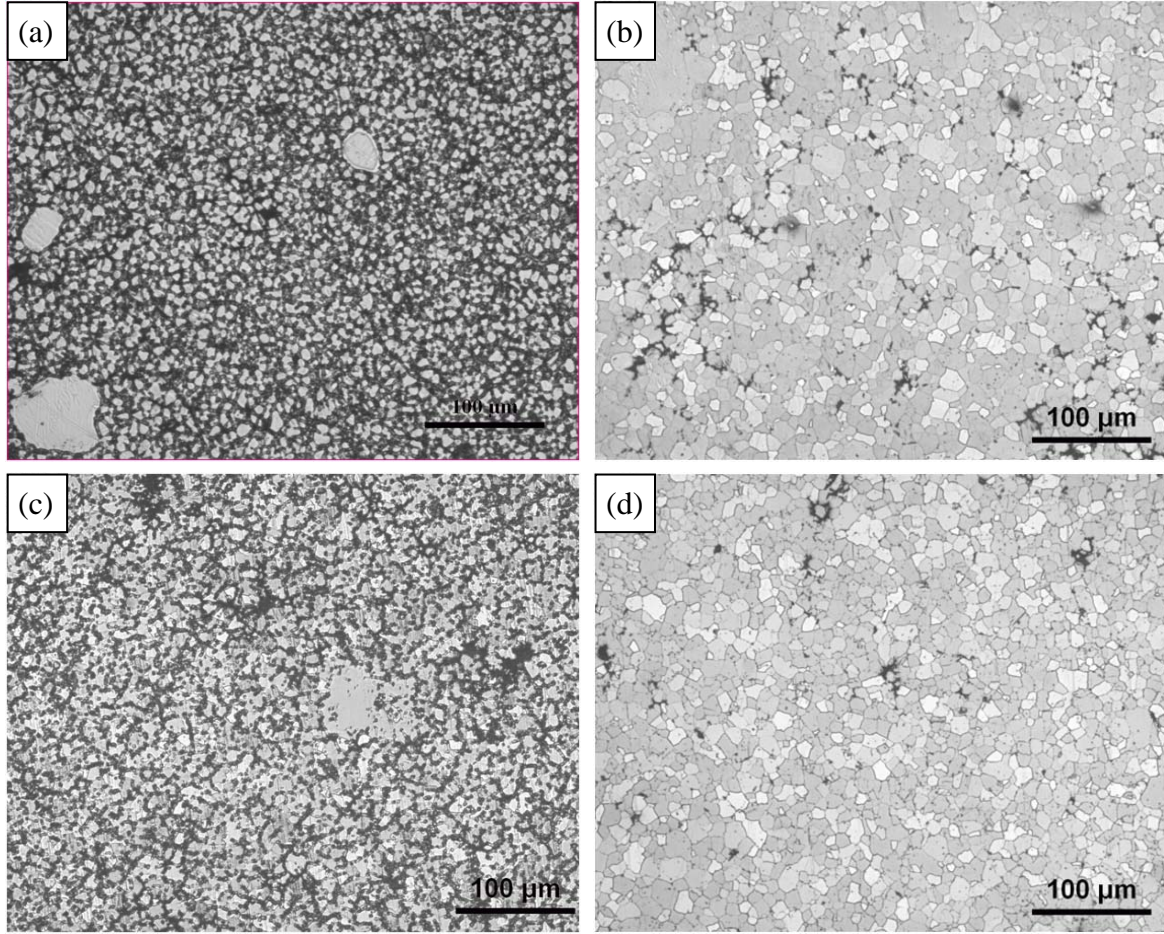


Figure 6.1: Microstructures of thixomolded AM60B alloy in different conditions: (a) Tx, (b) T4, (c) T5, and (d) T6.

Figure 6.1(a) shows typical thixotropic structure of Tx alloy with globular primary  $\alpha$ -Mg surrounded by network-like eutectic structure. Figure 6.1(b) shows the OM image of solution treated T4 alloy, where  $\alpha$ -Mg grains were distributed uniformly. It is seen that while the eutectic structure was no longer present, the grain size became considerably larger (about 20-25  $\mu\text{m}$ ) after the long period of solution treatment at 413°C in comparison with the Figure 6.1(a), where except a few large solid primary  $\alpha$ -Mg particles, the average  $\alpha$ -Mg grain size was measured to be  $\sim 5 \mu\text{m}$ . The microstructure for artificially aged T5 alloy is shown in



Figure 6.1(c), which was close to the thixotropic microstructure described above for Tx alloy with similar average  $\alpha$ -Mg grain size since the relative low aging temperature at 168°C did not drive the grain growth. The microstructure of solution treated and artificially aged T6 alloy was similar to that of T4 alloy, as seen in Figure 6.1(d).

Blandin *et al.* [14] carried out solution treatments on thixomolded AZ91 alloy and reported that there was no significant grain growth occurred for longer holding times at 350°C (below solvus), while the grain growth increase with increasing holding time at 415°C (above solvus). Another study [48] showed that the average grain diameter increased after 4 h heat treatment of the rheocast AM60 alloy at 395°C and 415°C (close to and above solvus), reaching a stable size of 100  $\mu\text{m}$ , from the starting values of 80  $\mu\text{m}$  in the period of time considered. This are in agreement with the results reported above.

To understand the microstructural changes in detail, the polished samples were further examined by SEM. The SEM images for the thixomolded AM60B alloy in the Tx, T4, T5, and T6 conditions are shown in Figure 6.2(a-d), respectively. As indicated for a Tx alloy in Figure 6.2(a); the grey phase shows the primary  $\alpha$ -Mg, while the bright phase is intermetallic  $\beta$ - $\text{Mg}_{17}\text{Al}_{12}$  in the eutectic bands of about 2-3  $\mu\text{m}$  comprised of two distinctive phases of eutectic  $\alpha+\beta$ . The EDS line scan and spectrum analysis revealed progressive depletion of Al content from the cell boundary towards the cell center as reported in Chapter 4. Further a small quantity of Al-Mn rich particles were also observed near the eutectic network, possibly  $\text{Al}_8\text{Mn}_5$  (shown in Figure 4.4 and 4.5). From the binary Mg-Al phase diagram, the dissolution of the  $\beta$ - $\text{Mg}_{17}\text{Al}_{12}$  phase is expected to occur at a temperature higher than the solvus

temperature, which is  $\sim 400^{\circ}\text{C}$  for AM60 alloy [13]. This resulted in the complete dispersion and fragmentation of eutectic network containing eutectic  $\alpha\text{-Mg}$  and an intermetallic  $\beta\text{-Mg}_{17}\text{Al}_{12}$  into a uniform  $\alpha\text{-Mg}$  matrix as shown in Figure 6.2(b) for T4 alloy after solution treatment at  $413^{\circ}\text{C}$  for 16 h. This uniform microstructure was likely to improve ductility and formability especially at elevated temperatures.

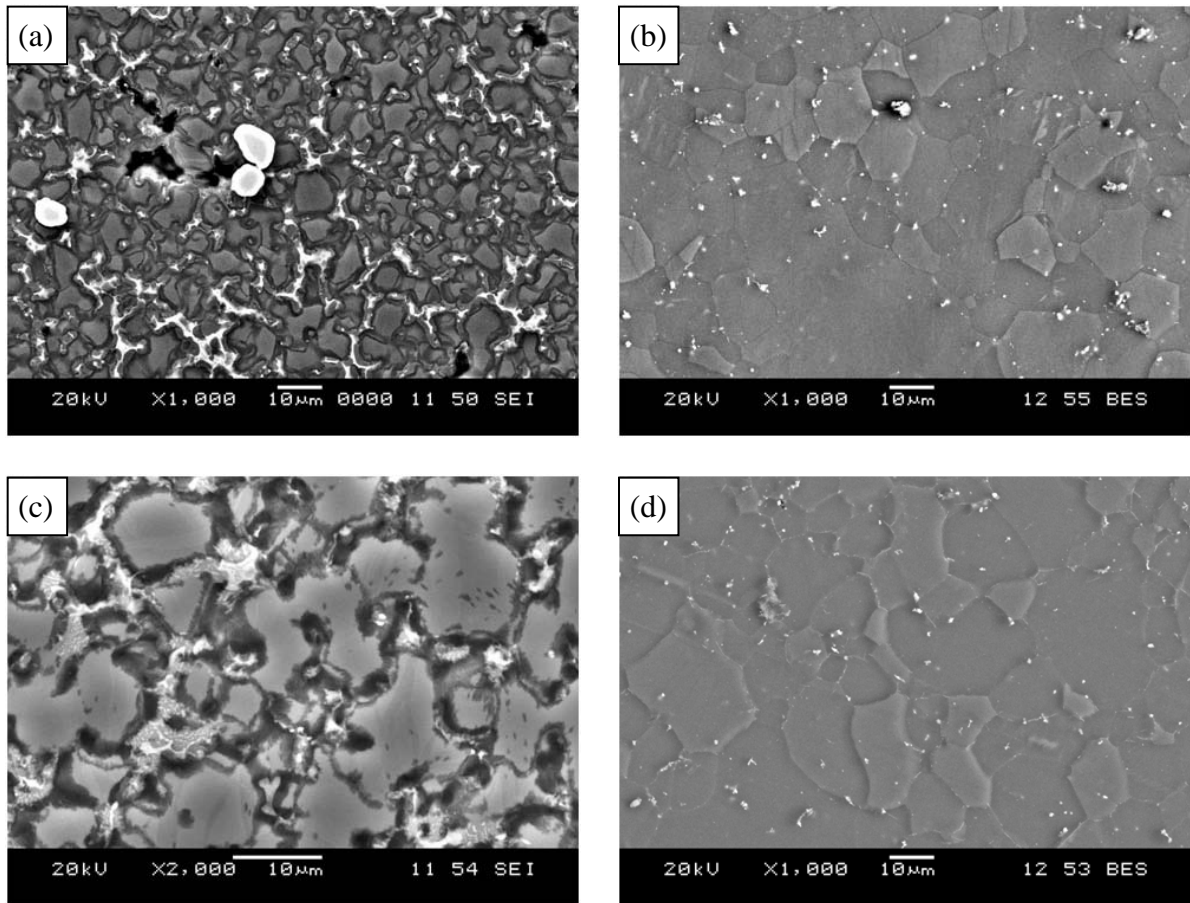
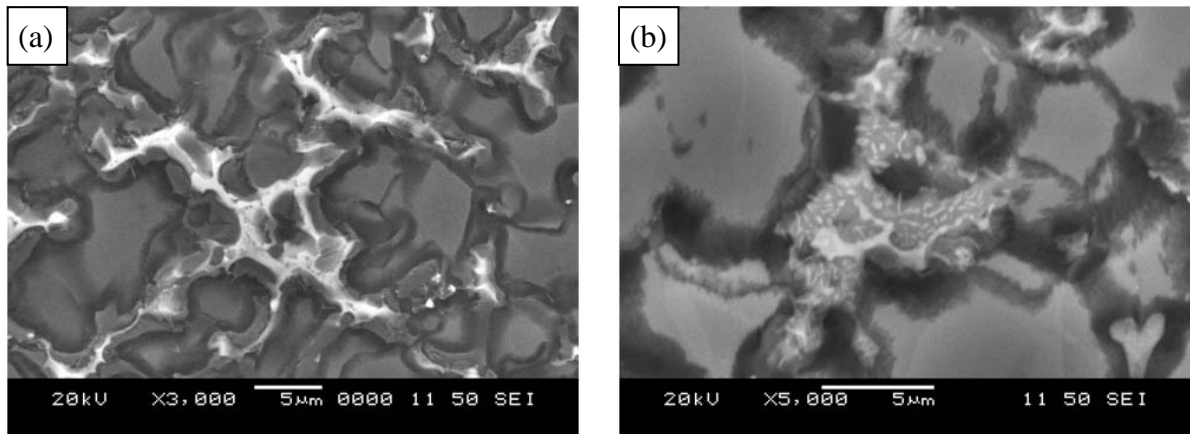


Figure 6.2: SEM images of thixomolded AM60B alloy in different conditions: (a) Tx, (b) T4, (c) T5, and (d) T6.

It is interesting to compare the T5 type aging with T6 aging that followed by solution treatment. Figure 6.2(c) and (d) shows the SEM images for AM60B T5 and T6 alloys,



respectively. The main advantage of the T5 treatment is to save time, energy and cost by avoiding solution treatment and enhance potential precipitation at a shorter time. The microstructure of T5 alloy (Figure 6.2(c)) was similar to the thixomolded alloy, while the microstructure of the T6 alloy (Figure 6.2(d)) was similar to that of T4 alloy. Such microstructural changes will be seen to be directly associated with the change in the tensile and fatigue properties, to be presented in the following sections. Further, higher magnification SEM images are presented in Figure 6.3(a) and (b) to better see the differences in the intermetallic phases in both Tx and T5 alloys, respectively.



*Figure 6.3: Higher magnification SEM images showing intermetallic phase of thixomolded AM60B alloy in two different conditions: (a) Tx, and (b) T5.*

It is of interest to note that a relatively more typical eutectic structure containing tiny  $\beta$  particles occurred in T5 alloy (Figure 6.3(b)), while that was in the form of irregular  $\beta$  bands in the divorced eutectic structure in Tx alloy as seen from Figure 6.3(a). In fact eutectic was the region where a high solute content remained after solidification available for subsequent aging. Cerri *et al.* [48] observed similar microstructure components when rheocast AM60

alloy directly aged at 220°C for 60 h. Blandin *et al.* [14] carried out solution treatment on thixomolded AZ91 alloy and Cerri *et al.* [48] performed solution treatment on rheocast AM60 alloy at 415°C for about 2-20 h (above solvus temperature) and observed that the  $\beta$ -phase was mostly dissolved and eutectic disappeared. In the present thixomolded AM60 alloy, the solution treatment (T4), performed at 413°C for 16 h, would lead to dissolution of eutectic structure with significant grain growth, while T5 treatment changed significantly the eutectic structure containing tiny  $\beta$  particles due to the big temperature difference.

## **6.2 Effect of Heat Treatment on Tensile Properties**

The tensile tests on the thixomolded and heat treated AM60B alloys were conducted at a constant strain rate of  $1 \times 10^{-3} \text{ s}^{-1}$  at room temperature and the resultant properties are listed in Table 6.1. Furthermore, the engineering stress-strain curves are compared in Figure 6.4. It is seen from Table 6.1 and Figure 6.4 that the thixomolded (Tx) alloy lay in-between the stress-strain curve of T5 and those of T4 and T6, giving rise to an intermediate YS and a lowest %El of about 9.3%. T4 treatment exhibited the lowest YS with a highest ductility of 13.5%, while T5 treatment resulted in the highest YS with an increased ductility to 10.7%. T6 treatment shows a marginally higher YS but lower ductility than T4 treatment. The UTS is indeed the same for Tx, T4, and T6 alloys in spite of the lower YS after T4 and T6 treatment. The present study indicated that both strength (YS and UTS) and ductility improved after T5 treatment while the strain hardening exponent remained essentially unchanged (0.21-0.22), in comparison with the original thixomolded (Tx) condition, although T4 and T6 treatment gave rise to a higher strain hardening exponent of 0.27-0.28 due to the

lower YS. The tensile properties of the heat treated thixomolded AM60B alloy are in agreement with those reported in [6].

*Table 6.1: Tensile properties for the heat treated and thixomolded AM60B alloy tested at a strain rate of  $1 \times 10^{-3} \text{ s}^{-1}$  at room temperature.*

Material condition	YS (MPa)	UTS (MPa)	%El	E (GPa)	n	K (MPa)
Tx	142	246	9.3	42.2	0.22	434
T4	119	245	13.5	41.0	0.28	491
T5	149	259	10.7	43.1	0.21	448
T6	121	244	12.1	42.5	0.27	482

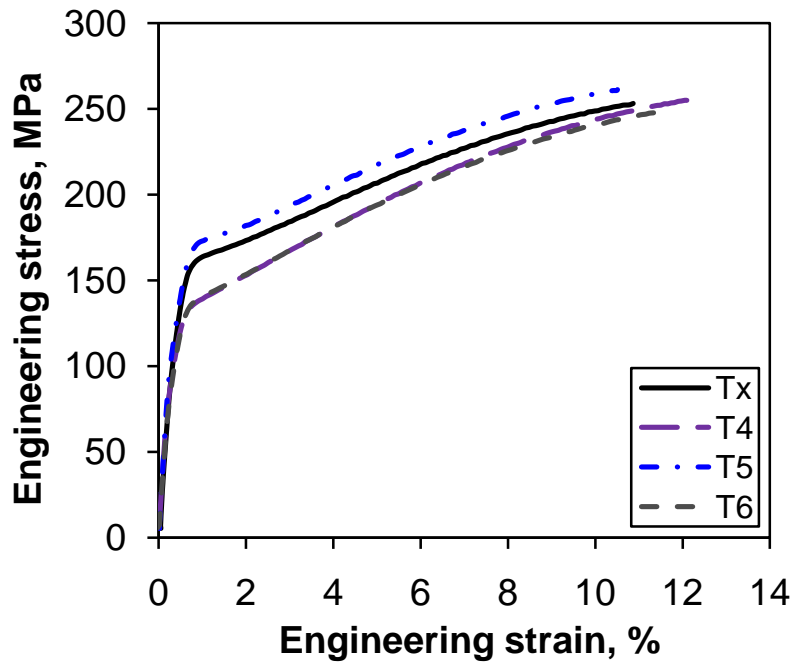


*Figure 6.4: Comparison of the engineering stress-strain curves for both thixomolded and heat treated AM60B alloy in different conditions.*

Figure 6.5 shows a comparison of the Kocks-Mecking type plot of strain hardening rate ( $\theta=d\sigma/d\varepsilon$ ) vs. true stress ( $\sigma$ ) at a strain rate of  $1\times 10^{-3} \text{ s}^{-1}$  for both thixomolded and heat treated AM60B samples. Stage III hardening occurred immediately after yielding as indicated by the linear decrease in the strain hardening rate ( $\theta$ ) in all the material conditions. The initial stress of hardening was higher for T5 followed by Tx, while T4 and T6 showed the lowest but equivalent initial stress of hardening with each other. Such a sequence in different material states was also true for the initial strain hardening rate, as seen in Fig. 6.5. The differences in the curves and the initial stress of hardening corresponded to their respective yield strengths. At lower values of  $\theta$ , stage IV hardening occurred as indicated by the very low level of strain hardening rate.

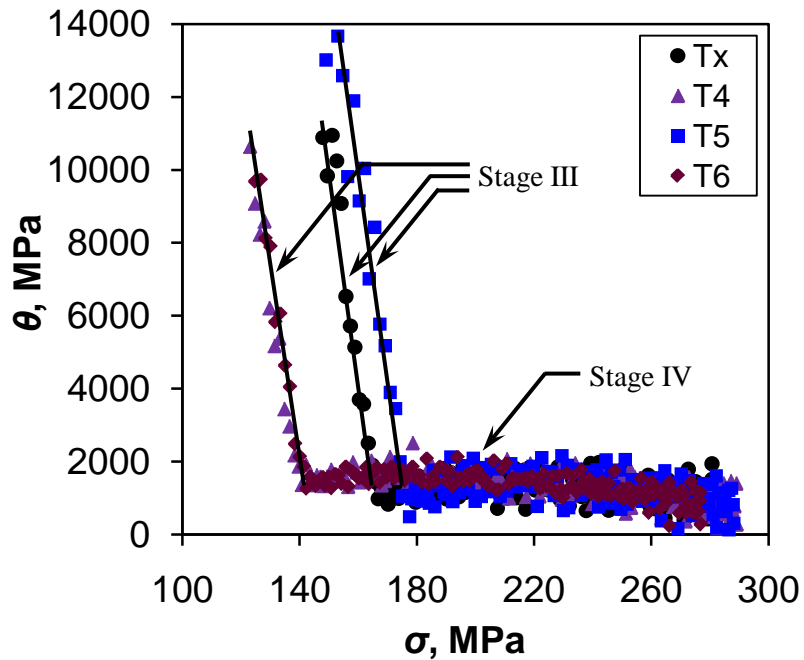


Figure 6.5: Comparison of the strain hardening rates against true stress for the thixomolded and heat treated AM60B alloy.

It is known that the tensile properties have direct relation with the microstructure [7-9, 119]. Since the average grain size of the  $\alpha$ -Mg matrix in different conditions varies from about 5 to 25  $\mu\text{m}$ , the Hall-Petch relationship in determining the proof strength would play a role. Since the  $\beta$ -phase was brittle and had a higher hardness (HV280), it may play an important role in the deformation mechanism of these alloys [7]. The thixomolded (Tx) and aged (T5) samples consisted of both  $\alpha$  (hcp) and  $\beta$  (bcc) phases. As reported in [13], the strain incompatibility between these two phases led to brittleness of the  $\alpha$ - $\beta$  interface and subsequently to lower ductility with higher strength. After the T4 and T6 treatment, these alloys showed better elongation with lower strength. In fact during the exposure at high temperatures (above solvus) the  $\beta$  phase tends to dissolve, enhancing the dislocation movement and reducing premature fracture [48].

### **6.3 Effect of Heat Treatment on Fatigue Behavior**

Completely reversed strain controlled fatigue tests (procedure reported in Chapter 3) were conducted on heat treated AM60B alloy and compared with each other as well as thixomolded condition. The effect of heat treatment on the stress amplitude and plastic strain amplitude was plotted against the number of cycles in Figure 6.6(a) and (b), respectively, at a total strain amplitude of 0.6%. Figure 6.6 shows that all samples at this applied total strain amplitude exhibited cyclic softening in the initial ~50 cycles with decreasing stress amplitude or increasing plastic strain amplitude, after which cyclic hardening occurred in remaining fatigue life.

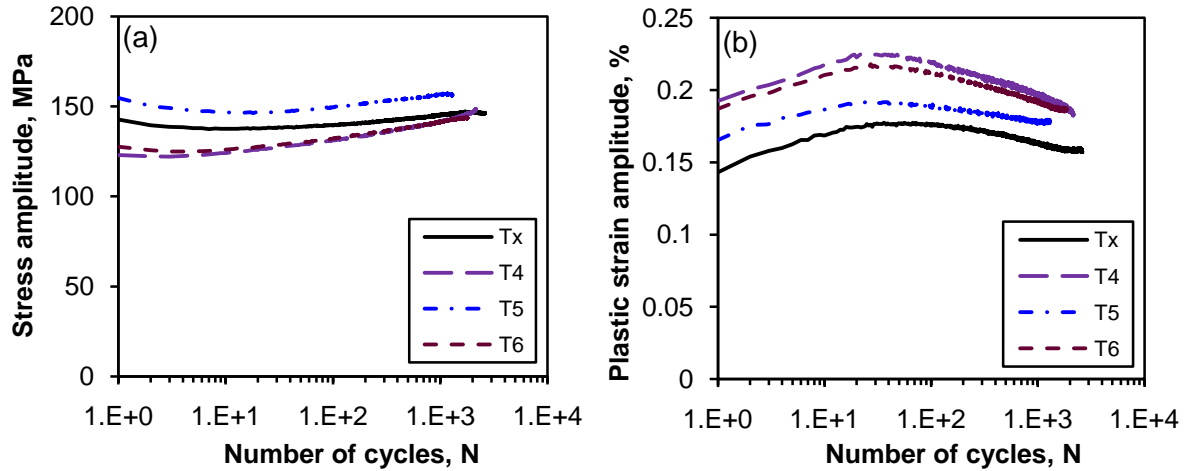


Figure 6.6: (a) Cyclic stress amplitudes and (b) plastic strain amplitudes for thixomolded and heat treated AM60B samples tested at a total strain amplitude of 0.6%.

The amount of hardening was slightly lower for T5 alloy, but it showed the highest stress amplitude, corresponding to the highest strength (Table 6.1 and Figure 6.4). While the T4 and T6 samples had the lowest stress amplitude and highest plastic strain amplitude, a higher rate of cyclic hardening is seen, as indicated by the increasing slope in Fig. 6.6(a) and decreasing slope in Fig. 6.6(b) after the initial about 50 cycles. The Tx alloy showed intermediate stress amplitude and rate of cyclic hardening. Since the total strain amplitude is constant at 0.6%, the sequence of the initial stress amplitudes corresponded to that of the YS of the test samples, that is, the highest for T5, intermediate for Tx, and the lowest for T4 and T6 samples. Similarly, Figure 6.6(b) shows the cyclic softening characteristics with increasing plastic strain amplitude in the initial stage and cyclic hardening characteristics with decreasing plastic strain amplitude in the later stage of the fatigue life for each alloy. This corresponded well to the cyclic hardening/softening behavior presented in Figure 6.6(a).

Here, the value of the plastic strain amplitude was related to the ductility of the alloy in different conditions (Table 6.1). This means that the value of the plastic strain amplitude was higher for T4 corresponding to its highest ductility, while the lower ductility of Tx alloy led to the lowest plastic strain amplitude (Figure 6.6(b)). Liu *et al.* [35] performed low cycle fatigue of AZ91 alloy in as-die cast, solution treated and aging conditions, and observed that the specimens with different heat histories exhibited different degrees of cyclic strain hardening. The aged specimen exhibited the highest monotonic and cyclic strength but the lowest of cyclic strain hardening. The solution treated specimens had the lowest monotonic and cyclic strength but the highest cyclic strain hardening. The die casting specimens had moderate monotonic, cyclic strength and cyclic strain hardening. All of these results are in good agreement with the observation in the current investigation although the processing condition was different.

Figure 6.7 shows the fatigue lifetime of AM60B in various heat treated conditions. All samples showed a similar trend of increasing fatigue life with decreasing strain amplitude. Run-outs were indicated by arrows at or slightly over  $10^7$  cycles and all samples did not fail at a total strain amplitude of 0.2%. Comparatively all samples showed fatigue life very close to each other within a certain degree of experimental scatter. Overall, at higher strain amplitudes T6 alloy appeared to have a higher fatigue resistance along with T4 alloy which was very close to it, while T5 alloy has a slightly lower fatigue life. Tx alloy showed basically an intermediate fatigue life. The fatigue life at the lower strain amplitudes for both thixomolded and heat treated samples was essentially the same within the experimental scatter.

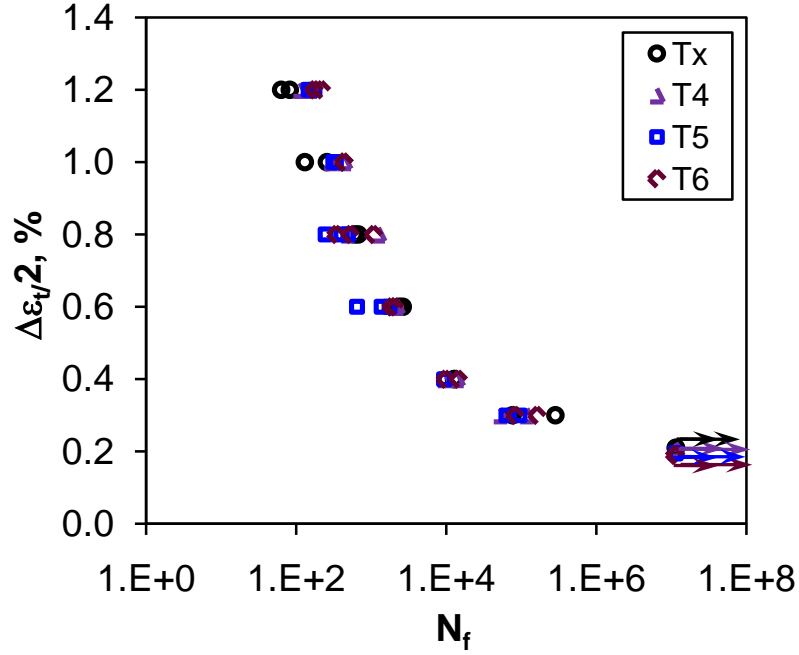


Figure 6.7: Comparison of the fatigue lifetime curves for the thixomolded and heat treated AM60B samples.

Figure 6.8 shows the cyclic stress-strain curves for the thixomolded AM60B alloy in various conditions. It is seen that the cyclic stress-strain curves corresponded nicely to the monotonic stress-strain curves (Figure 6.4), with the same effect of heat treatment on both the monotonic and cyclic deformation behavior. The major difference lay in the elastic-plastic transition. That is, a smooth transition occurred in the cyclic deformation (Figure 6.8), while a yield-point-like transition characteristic was seen in the monotonic deformation (Figure 6.4).



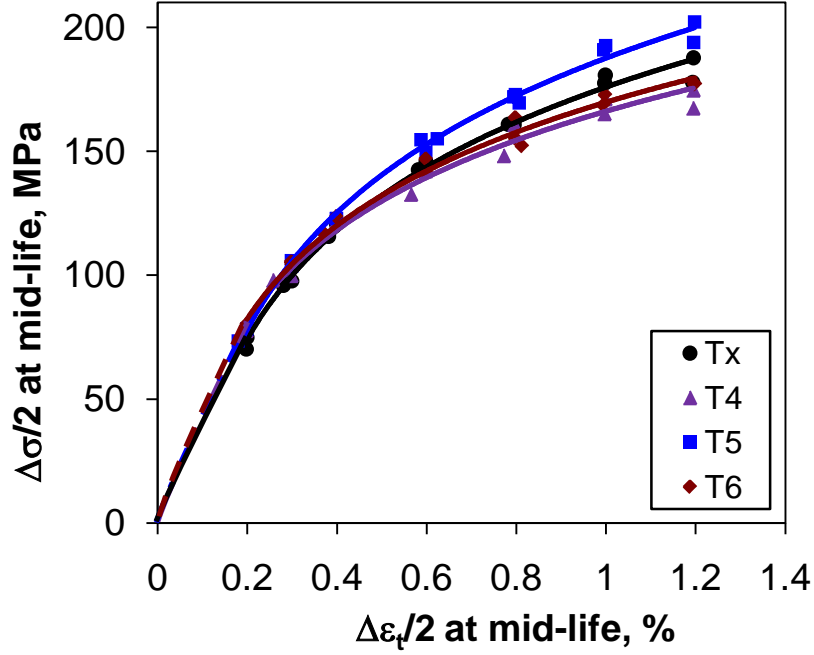


Figure 6.8: Comparison of the cyclic stress-strain curves for thixomolded and heat treated AM60B alloy.

The fatigue parameters evaluated according to Eqs. (1-3) from Chapter 2 are listed in Table 6.2 in comparison with various heat treatment conditions for AM60B alloy. The cyclic yield strength  $\sigma'_y$  was equivalent to the monotonic YS for Tx alloy (Table 6.1), while for all heat treated samples  $\sigma'_y$  was observed to be higher than the monotonic YS (Table 6.1). This seemed to suggest that heat treatment enhanced the cyclic deformation resistance. It is seen that there were almost no differences between the parameters of T4 and T6 states, indicating an equivalent fatigue life in the two conditions, but some changes have happened for Tx and T5 samples. The values of  $\sigma'_f$  and  $b$  were higher in T5 sample, lower in Tx sample and intermediate in T4/T6 samples.

Table 6.2: Fatigue parameters obtained from fully reversed strain-controlled tests for the heat treated and thixomolded AM60B samples.

Low cycle fatigue parameters	Tx	T4	T5	T6
Cyclic yield strength, $\sigma'_y$ , MPa	144	130	154	130
Fatigue strength coefficient, $\sigma'_f$ , MPa	439	468	533	458
Fatigue strength exponent, $b$	-0.11	-0.13	-0.13	-0.12
Fatigue ductility coefficient, $\epsilon'_f$ , %	3.6	8.0	1.3	6.0
Fatigue ductility exponent, $c$	-0.37	-0.44	-0.26	-0.40
Cyclic strain hardening exponent, $n'$	0.23	0.20	0.27	0.20
Cyclic strength coefficient, $K'$ , MPa	630	473	826	500

It is well known that, as a measurable physical parameter during total strain-controlled cyclic deformation, cyclic plastic strain resulted in a number of damage processes which affected the strain fatigue life [29]. Further, in the case of the low-cycle fatigue, the cyclic plastic strain resulted from the applied cyclic strain rather than from cyclic stress [66]. It is thus noted that the values of the fatigue ductility coefficient  $\epsilon'_f$  and exponent  $c$  (evaluated from Coffin-Manson relation Eq. (2)) were highest for T4/T6, intermediate for Tx and lowest for T5. Based on the above observations with higher value of  $\sigma'_f$  and lower value of  $\epsilon'_f$ , T5 alloy should show lower fatigue resistance compared to others which corresponded well to Figure 6.7. Similarly intermediate values of  $\sigma'_f$  and lower value of  $\epsilon'_f$  could be responsible for the longer fatigue life of T6 and T4 alloy compared to others, with Tx alloys showing moderate results (Figure 6.7).

## 6.4 Summary on the Effect of Heat Treatment

The effect of heat treatment on the microstructure and mechanical properties of a thixomolded AM60B alloy has been studied in this chapter. The original thixomolded (Tx) alloy consisted of globular primary  $\alpha$ -Mg and network-like eutectic structure containing eutectic  $\alpha$ -Mg and intermetallic  $\beta$ -Mg<sub>17</sub>Al<sub>12</sub>. After solution treatment (T4) at 413°C, the eutectic structure completely dissolved and single  $\alpha$  phase alloy was developed but with significant grain growth. The aging treatment (T5) at 168°C for 16 h showed that significant microstructural changes occurred in the eutectic structure. While irregular eutectic  $\beta$  bands were present in the thixomolded condition, a more typical eutectic structure containing tiny  $\beta$  particles appeared after T5 treatment. There seemed to be no significant microstructural change occurred in the T6 state in comparison with the T4 sample.

The presence of eutectic structure in the Mg alloy was observed to increase strength and reduce ductility due to the resistance of intermetallic  $\beta$  phase to the movement of dislocations. Among the samples with the eutectic structure, the thixomolded alloy exhibited intermediate YS and lowest ductility, while aging treatment resulted in the highest YS with elongation slightly higher than that of thixomolded alloy. The dissolution of eutectic structure facilitated the dislocation movement and reduced premature fracture in the solution and solution-aged samples, leading to increased ductility and reduced yield strength. The cyclic stress-strain curves were observed to have a similar effect of heat treatment on the monotonic tensile stress-strain curves. However, a smooth transition occurred during cyclic deformation, while a yield-point-like transition characteristic appeared in the monotonic

deformation. Since these solution and solution-aging specimens had the highest values of fatigue ductility exponent (absolute value) and fatigue ductility coefficient, the strain-controlled low cycle fatigue life was higher at higher strain amplitudes. The aged specimens exhibited the highest fatigue strength coefficient but lowest fatigue ductility coefficient and fatigue ductility exponent, corresponding to the slightly lower low cycle cyclic life at higher strain amplitudes, while the thixomolded specimen exhibited an intermediate fatigue life. The fatigue life at the lower strain amplitudes for both thixomolded and heat treated samples was basically the same within the experimental scatter.

## CHAPTER 7

### SUMMARY, CONCLUSIONS AND FUTURE WORK

#### 7.1 Summary and Conclusions

1. The microstructure of the thixomolded AZ91D and AM60B alloys consisted of globular primary  $\alpha$ -Mg and network-like eutectic structure containing eutectic  $\alpha$ -Mg and intermetallic  $\beta$ -Mg<sub>17</sub>Al<sub>12</sub>, along with some Al-Mn particles. More primary  $\alpha$ -Mg phase was present in the AM60B alloy than in the AZ91D alloy, with a volume fraction of 0.57 and 0.35, respectively. The porosity remained nearly constant at a level of 1.25-1.30% for both alloys.
2. While the ultimate tensile strength (UTS) was equivalent within experimental scatter for both alloys, the yield strength (YS) was higher and the ductility was lower for the AZ91D alloy than for the AM60B alloy due to the presence of more primary  $\alpha$ -Mg phase and a smaller amount of hard and brittle intermetallic  $\beta$ -Mg<sub>17</sub>Al<sub>12</sub> in the AM60B alloy. This also gave rise to slightly higher strain hardening exponents evaluated for the AM60B alloy in comparison with the AZ91D alloy.
3. Little effect of strain rate on the YS, UTS and strain hardening exponent for the AZ91D alloy was observed, while the UTS and strain hardening exponent increased slightly with increasing strain rate from  $1 \times 10^{-5}$  to  $1 \times 10^{-1} \text{ s}^{-1}$  for the AM60B alloy.

4. The AZ91D alloy displayed a gradual transition from elastic to plastic deformation, while the AM60B alloy showed a tendency of yield-point-like phenomenon which became more obvious with increasing strain rate.
5. After yielding, stage III and stage IV hardening occurred in both AZ91D and AM60B alloys. The slope of strain hardening rate was observed to increase with increasing strain rate for both alloys. The strong strain hardening was attributed to the dislocation pile-ups at the grain boundaries and twin boundaries, as well as slip-twinning interactions.
6. SEM examinations of tensile fracture surfaces and side surfaces revealed that cleavage-like fracture accompanied by secondary cracking along the eutectic structure occurred in the AZ91D alloy, while some shallow dimples due to the formation and coalescence of microvoids were observed on the fracture surface of AM60B alloy, giving rise to higher ductility.
7. Low cycle fatigue tests showed that stress amplitude increased and plastic strain amplitude decreased with increasing total strain amplitude for both AZ91D and AM60B alloys. The amount of hardening effect was higher at higher strain amplitudes, and decreased with decreasing total strain amplitudes, while almost constant at lower strain amplitudes.
8. The hysteresis loops in both the thixomolded Mg alloys were basically symmetrical in tension and compression, which were very different from those of extruded Mg alloys exhibiting early yielding in the compressive phase leading to skewed and

unsymmetrical hysteresis loops. However, there remained a strong non-linear stress-strain variation in both ascending and descending phases especially at higher strain amplitudes, which was in sharp contrast to the typical hysteresis loops of fcc alloys. Furthermore, the mid-life hysteresis loops exhibited a clockwise rotation.

9. The elastic moduli in both loading and unloading phases were observed to decrease with increasing strain amplitude arising from the strong nonlinear or pseudoelastic cyclic deformation behavior due to the occurrence of twinning and detwinning.
10. The fatigue life of the thixomolded AZ91D and AM60B alloys, which increased with decreasing strain amplitude and strain ratio, was observed to be equivalent to that of its die cast counterpart at higher strain amplitudes, but significantly higher than that of its die cast counterpart at lower strain amplitudes.
11. The mean stress relaxation was observed to occur mainly in the initial 10~20% of the fatigue life, and the mean stresses were basically stabilized after mid-life. However, only partial mean stress relaxation was present in the thixomolded Mg alloys. The negative mean stresses occurred at lower strain ratios led to an increased fatigue life in both alloys.
12. Fatigue cracks were observed to initiate from the specimen surface or near-surface defects, such as pores/inclusions, regardless of the strain amplitudes applied. Fatigue crack propagation was mainly characterized by fatigue striation-like features coupled with some secondary cracks and tear ridges in both the alloys.

13. Two types of twins (wider lenticular extension twins and narrower banded contraction twins) were observed to occur in some favorably oriented and relatively large primary  $\alpha$ -Mg grains near the fracture surface of both AZ91D and AM60B alloys.
14. The solution treatment on thixomolded AM60B alloy (T4) resulted in the formation of single  $\alpha$  phase by dissolving eutectic structure. Aging treatment directly on the thixomolded AM60B alloy (T5) led to a significant change in the eutectic structure which contained tiny  $\beta$  particles. There appeared to be no significant microstructural change after solution-aging treatment (T6) in comparison with the T4 sample.
15. After direct aging treatment (T5), the yield strength and ultimate tensile strength increased while the ductility remained unchanged or slightly higher. However, both the solution only (T4) and solution plus aging (T6) led to lower yield strength and ultimate tensile strength but the ductility increased.
16. The cyclic stress-strain curves were observed to have a similar effect of heat treatment on the monotonic tensile stress-strain curves. However, a smooth transition occurred during cyclic deformation, while a yield-point-like transition characteristic appeared in the tensile deformation.
17. The fatigue life at higher strain amplitudes seemed to be higher in the T4 and T6 conditions, intermediate in the thixomolded condition, and slightly lower in the T5 condition. Nevertheless, at the lower strain amplitudes the fatigue life for both the thixomolded and all the heat treated samples was essentially the same within the experimental scatter.



## **7.2 Recommendations for Future Work**

The use of the Mg alloys is still limited mainly due to their poor corrosion resistance, low formability and creep properties. However, considerable research efforts have been devoted recently to overcome these drawbacks, and today new developments are increasingly carried out. Thixomolding process has a 20-year track record of research with commercial applications beginning in 1992. The present investigation was aimed at studying the mechanical properties and fatigue behavior of AZ91D and AM60B Mg alloys, and further improving the properties of the AM60B alloy via heat treatment. While a number of results have been obtained in the present study, there still remained a lot of work that needs to be done. The following points are the recommendations for the future work.

1. High temperature tests for both alloys would be an interesting aspect to study the creep behavior or creep-fatigue interaction of these alloys both in tensile and fatigue modes, since no such results have been reported in the literature for thixomolded AM60B and AZ91D alloys.
2. While in the LCF, once the crack initiates, it would propagate quickly due to the high stress level; in the HCF, the crack propagation would consume most of the fatigue life. It is thus interesting to study the fatigue crack growth behavior and the related propagation mechanisms for these alloys.
3. Fracture toughness of these alloys using notched samples needs to be performed.

4. In the present investigation, the effect of solution-aging (T6) treatment on the AM60B alloy seemed to be not so effective. The heat treatment procedure needs to be further optimized.
5. Detailed microstructural characterization of the thixomolded Mg alloys with or without heat treatment needs to be done using high temperature XRD and TEM.
6. There were a number of reports describing the appearance and disappearance of twins (also known as twinning-detwinning behavior) by observing in-situ fatigue deformation in some wrought Mg alloys. It would be of great interest to carry out an in-situ examination of the present thixomolded Mg alloys.

## REFERENCES

- [1] T.M. Pollock, Weight loss with magnesium alloys. *Science* **328**, 986-987, 2010.
- [2] M. Wise, K. Calvin, A. Thomson, L. Clarke, B. Bond-Lamberty, R. Sands, S.J. Smith, A. Janetos, J. Edmonds, Implications of limiting CO<sub>2</sub> concentrations for land use and energy. *Science* **324**, 1183-6, 2009.
- [3] J.A. Patz, D. Campbell-Lendrum, T. Holloway, J.A. Foley, Impact of regional climate change on human health. *Nature* **438**, 310-17, 2005.
- [4] L.R. Kump, Reducing uncertainty about carbon dioxide as a climate driver. *Nature* **419**, 188-90, 2002.
- [5] G.S. Cole, Summary of "Magnesium Vision 2020: A North American Automotive Strategic Vision for Magnesium". In: R.S. Beals, A.A. Luo, N.R. Neelameggham, M.O. Pekguleryuz, (Eds.) *Magnesium Technology 2007*, TMS, Orlando, FL , United States, Feb. 25-Mar. 1, 2007, pp. 35-40.
- [6] K. Sadayappan, M. Vassos, Evaluation of a Thixomolded Magnesium Alloy Component for Automotive Application, In: *SAE 2010 World Congress & Exhibition*, SAE International **SAE 10M-0298**, 1-8, 2010.
- [7] F. Czerwinski, A. Zielinska-Lipiec, P.J. Pinet, J. Overbeeke, Correlating the microstructure and tensile properties of a thixomolded AZ91D magnesium alloy. *Acta Mater.* **49**, 1225-1235, 2001.
- [8] Y.F. Zhang, Y.B. Liu, Q.Q. Zhang, Z.Y. Cao, X.P. Cui, Y. Wang, Microstructural evolution of thixomolded AZ91D magnesium alloy with process parameters variation. *Mater. Sci. Eng. A* **444**, 251-256, 2007.

- [9] Y.F. Zhang, Y.B. Liu, Z.Y. Cao, Q.Q. Zhang, L. Zhang, Mechanical properties of thixomolded AZ91D magnesium alloy. *J. Mater. Process. Technol.* **209**, 1375-1384, 2009.
- [10] R. Beals, S. LeBeau, O. Roberto, P. Shashkov, Advances in thixomolding magnesium alloys part II. In: *H.I. Kaplan (Ed.), Magnesium Technology 2003*, TMS, San Diego, California, United States, Mar. 2-6, 2003, pp. 283-288.
- [11] T.K. Nandy, R.M. Messing, J.W. Jones, T.M. Pollock, D.M. Walukas, R.F. Decker, Microstructure and properties of blended Mg-Al alloys fabricated by semisolid processing. *Metall. Mat. Trans. A* **37**, 3725-3736, 2006.
- [12] P. E. Thoma, C. Hays, A. Baik, Influence of microstructure on the fracture and tensile properties of die cast and thixomolded magnesium alloys. *Materials Research Society Symposium - Proceedings* **539**, 35-40, 1999.
- [13] B. Mansoor, S. Mukherjee, A. Ghosh, Microstructure and porosity in thixomolded Mg alloys and minimizing adverse effects on formability. *Mater. Sci. Eng. A* **512**, 10-18, 2009.
- [14] J. J. Blandin, D. Giunchi, M. Suery, E. Evangelista, Effect of thermal treatments on mechanical behaviour of thixoformed magnesium alloy. *Mater. Sci. Technol.* **18**, 333-40, 2002.
- [15] L. Yang, Y. Wei, L. Hou, Microstructure evolution of thixomolding AZ91D magnesium alloy during heat treatment. *J. Mater. Sci.* **45**, 3626-3634, 2010.
- [16] E. Evangelista, S. Spigarelli, P. Cavaliere, Microstructure and mechanical properties of a thixoformed AZ91 magnesium alloy. *Key Eng. Mat.* **188**, 139-148, 2000.

- [17] M. Cabibbo, E. Cerri, E. Evangelista, Microstructural study after solution treatments of a thixocast AZ91. *In: N. Hryn (Ed.) Magnesium Technology 2001, TMS*, New Orleans, Louisiana, United States, Feb. 11-15, 2001, pp. 211-216.
- [18] Z. Chen, B.Kuhr, A. Ritter, J. Huang, R. Decker, S. LeBeau, C.J. Boehlert, The effect of thermomechanical processing on the tensile and fatigue behavior of thixomolded® AM60, *In: S.R. Agnew, N.R. Neelameggham, E.A. Nyberg, W. Sillekens (Eds.), Magnesium Technology 2010, TMS*, Seattle, WA, United States, Feb. 14-18, 2010, pp. 495-500.
- [19] C. Potzies, K.U. Kainer, Fatigue of die-cast magnesium alloys, *In: A.A. Luo (Ed.) Magnesium Technology 2004, TMS*, Charlotte, NC, United States, Mar. 14-18, 2004, pp. 275-278.
- [20] H. Mayer, M. Papakyriacou, B. Zettl, S.E. Stanzl-Tschegg, Influence of porosity on the fatigue limit of die cast magnesium and aluminium alloys. *Int. J. Fatigue* **25**, 245-256, 2003.
- [21] F. Renner, H. Zenner, Fatigue strength of die-cast magnesium components. *Fatigue Fract. Engng. Mater. Struct.* **25**, 1157-1168, 2002.
- [22] R.K. Islamgaliev, O.B. Kulyasova, B. Mingler, M. Zehetbauer, A. Minkow, Structure and fatigue properties of the Mg alloy AM60 processed by ECAP. *Mater. Sci. Forum* **584-586**, 803-808, 2008.
- [23] O. Kulyasova, R. Islamgaliev, B. Mingler, M. Zehetbauer, Microstructure and fatigue properties of the ultrafine-grained AM60 magnesium alloy processed by equal-channel angular pressing. *Mater. Sci. Eng. A* **503**, 176-180, 2009.

- [24] R. Zeng, E. Han, L. Liu, Y. Xu, W. Ke, Effect of rolled microstructure on fatigue properties of magnesium alloy AM60. *Chinese J. Mater. Research (Cailiao Yanjiu Xuebao)* **17**, 241-246, 2003.
- [25] R. Zeng, E. Han, W. Ke, L. Liu, Y. Xu, Corrosion fatigue of as-extruded AM60 magnesium alloy. *Chinese J. Mater. Res. (Cailiao Yanjiu Xuebao)* **19**, 1-7, 2005.
- [26] R. Zeng, E. Han, W. Ke, W. Dietzel, K.U. Kainer, A. Atrens, Influence of microstructure on tensile properties and fatigue crack growth in extruded magnesium alloy AM60. *Int. J. Fatigue* **32**, 411-419, 2010.
- [27] H. El Kadiri, M.F. Horstemeyer, J.B. Jordon, Y. Xue, Fatigue crack growth mechanisms in high-pressure die-cast magnesium alloys. *Metall. Mat. Trans. A* **39**, 190-205, 2008.
- [28] G. Eisenmeier, B. Holzwarth, H.W. Hoppel, H. Mughrabi, Cyclic deformation and fatigue behaviour of the magnesium alloy AZ91. *Mater. Sci. Eng. A* **319-321**, 578-582, 2001.
- [29] L. Chen, J. Shen, W. Wu, F. Li, Y. Wang, Z. Liu, Low-cycle fatigue behavior of magnesium alloy AZ91. *Mater. Sci. Forum* **488-489** 725-728, 2005.
- [30] M.F. Horstemeyer, N. Yang , K. Gall, D. McDowell, J. Fan, P. Gullett, High cycle fatigue mechanisms in a cast AM60B magnesium alloy. *Fatigue Fract. Engng. Mater. Struct.* **25**, 1045-1056, 2002.
- [31] S.G. Lee, G.R. Patel, A.M. Gokhale, Inverse surface macro-segregation in high-pressure die-cast AM60 magnesium alloy and its effects on fatigue behavior. *Scr. Mater.* **52**, 1063-1068, 2005.

- [32] S.G. Lee, G.R. Patel, A.M. Gokhale, The effect of inverse macro-segregation on fatigue behavior of die-cast AM60 magnesium alloy. *Mater. Sci. Forum* **488-489**, 713-716, 2005.
- [33] M.F. Horstemeyer, N. Yang, K. Gall, D.L. McDowell, J. Fan, P.M. Gullett, High cycle fatigue of a die cast AZ91E-T4 magnesium alloy. *Acta Mater.* **52**, 1327-1336, 2004.
- [34] F. Li, Y. Wang, L. Chen, Z. Liu, J. Zhou, Low-cycle fatigue behavior of two magnesium alloys. *J. Mater. Sci.* **40**, 1529-1531, 2005.
- [35] Z. Liu, Y.Y. Xu, Z.G. Wang, Y. Wang, Z.Y. Liu, Low cycle fatigue behavior of AZ91HP alloy in as high pressure die casting. *Acta Metallurgica Sinica (English Letters)* **13**, 961-966, 2000.
- [36] Z. Liu, H. Ji, L. Lin, L. Chen, W. Wu, L. Yang, Cyclic deformation behavior and potential automobile application of magnesium die casting alloys AZ91 and AM50, *Mater. Sci. Forum* **539-543**, 1626-1631, 2007.
- [37] A.R. Moore, C.J. Torbet, A. Shyam, J.W. Jones, D.M. Walukas, R.F. Decker, Fatigue behavior of thixomolded® magnesium AZ91D using ultrasonic techniques, *In: A.A. Luo (Ed.), Magnesium Technology 2004, TMS*, Charlotte, NC, United States, Mar. 14-18, 2004, pp. 263-268.
- [38] F. D'Errico, M. Boniardi, G. Perricone, D. Vujanovic, Influence of microstructure on mechanical properties of an AZ91D thixomolded® magnesium alloy. *Key Eng. Mat.* **348-349**, 873-876, 2007.
- [39] T. Tsukeda, K. Saito, K. Takeya, K. Kitamura, The latest technology trends on thixomolding® of magnesium alloys *Mater. Sci. Forum* **488-489**, 287-290, 2005.

- [40] K.U. Kainer, *Magnesium Alloys and Technology*, Wiley-VCH, Weinheim, Germany, 2003.
- [41] N. Li, R. Osborne, B. Cox, D. Penrod, The USCAR structural cast magnesium development project, *In: 2005 TMS Annual Meeting, Minerals, Metals and Materials Society*, San Francisco, CA, United States, Feb. 13-17, 2005, p. 535.
- [42] R.S. Beals, Z.K. Liu, J.W. Jones, P.K. Mallick, D. Emadi, D. Schwam, B.R. Powell, USAMP magnesium powertrain cast components: Fundamental research summary. *JOM* **59**, 43-48, 2007.
- [43] F. Czerwinski, Selected aspects of semisolid forming magnesium alloys *Mater. Sci. Forum* **539-543** 1644-1649, 2007.
- [44] M. Regev, H. Rosenson, Z. Koren, Microstructure study of particle reinforced AZ91D and AM50 magnesium alloy semisolid casting. *Mater. Sci. Technol.* **23**, 1485-1491, 2007.
- [45] M.M. Avedesian, H. Baker, *Magnesium and Magnesium Alloys - ASM Speciality Handbook*, ASM International® Publication, United States of America, 1999.
- [46] F. Czerwinski, Microstructure control during thixomolding of magnesium alloys. *J. Adv. Mater.* **38**, 8-11, 2006.
- [47] F. Czerwinski, Processing features of thixomolding magnesium alloys. *Die Casting Engineer* **48**, 52-58, 2004.
- [48] E. Cerri, P. Cavaliere, P. Leo, P.P. De Marco, Heat treatment and mechanical properties of a rheocast magnesium alloy, *In: A.A. Luo, N.R. Neelameggham, R.S. Beals (Eds.), Magnesium technology 2006, TMS*, San Antonio, TX, United States, March 12-16, 2006, pp. 109-113.



- [49] B. Song, Y. Liu, X. Yang, J. An, Effects of Y addition and solid solution treatment on microstructure and mechanical properties of AM60 magnesium alloys. *Transactions of Materials and Heat Treatment (Cailiao Rechuli Xuebao)* **27**, 34-36+41, 2006.
- [50] B., Y. Song, Liu, J. An, Effects of neodymium addition and solid solution treatment on microstructure and mechanical properties of AM60 alloy. *Foundry Technology (Zhuzao Jishu)* **27**, 1299-1302, 2006.
- [51] D. Ghosh, K. Kang, J.G. Roemer, C. VanSchilt, R.D. Carnahan, R.F. Decker, P.S. Frederick, N. Bradley, Properties and microstructure of thixomolded and heat-treated AZ61A magnesium alloy, *Proceedings of the international symposium on advances in production and fabrication of light metals and metal matrix composites*, Edmonton, Alberta, Canada, 1992, p. 399.
- [52] D. Ghosh, K. Kang, C. Bach, J.G. Roemer, C. VanSchilt, Development of ductile thixomolded magnesium alloys, *In: S. Macewen, J.P. Gilardeau (Eds.), Proceedings of the International Symposium on Recent Metallurgical Advances in Light Metals Industries*, Vancouver, Canada, 1995, pp. 473-479.
- [53] H. Eibisch, A. Lohmuller, N. Kompel, R.F. Singer, Effect of solidification microstructure and Ca additions on creep strength of magnesium alloy AZ91 processed by Thixomolding. *Int. J. Mater. Res.* **99**, 56-66, 2008.
- [54] H. Frank, H. Dieringa, N. Hort, K.U. Kainer, The influence of the casting process on the creep properties of different AZ-based magnesium alloys, *Modeling of casting, welding and advanced solidification processes - XI, Minerals, Metals and Materials Society*, Opio, France, May 28-June 2, 2006, pp. 669-676.

- [55] S.H.C. Park, Y.S. Sato, H. Kokawa, Microstructural evolution and its effect on Hall-Petch relationship in friction stir welding of thixomolded Mg alloy AZ91D. *J. Mater. Sci.* **38**, 4379-4383, 2003.
- [56] P. Su, A. Gerlich, M. Yamamoto, T.H. North, Formation and retention of local melted films in AZ91 friction stir spot welds. *J. Mater. Sci.* **42**, 9954-9965, 2007.
- [57] J.A. Esparza, W.C. Davis, L.E. Murr, Microstructure-property studies in friction-stir welded, thixomolded magnesium alloy AM60. *J. Mater. Sci.* **38**, 941-952, 2003.
- [58] Z. Zhao, Q. Chen, F. Kang, D. Shu, Microstructural evolution and tensile mechanical properties of thixoformed AZ91D magnesium alloy with the addition of yttrium. *J. Alloys Compd.* **482**, 455-467, 2009.
- [59] E. El-Magd, M. Abouridouane, Characterization, modelling and simulation of deformation and fracture behaviour of the light-weight wrought alloys under high strain rate loading. *Int. J. Impact Eng.* **32**, 741-758, 2006.
- [60] M.A. Meyers, *Dynamic Behavior of Materials*, Springer, Berlin, 1994.
- [61] T. Abbott, M. Easton, W. Song, Mechanical behaviour of cast magnesium alloys, *Mat. Sci. Forum* **419-422**, 141-146, 2003.
- [62] T. Abbott, M. Easton, R. Schmidt, Magnesium for crashworthy components, *In: H.I. Kaplan (Ed.), Magnesium Technology 2003*, TMS, San Diego, California, United States, Mar. 2-6, 2003, pp. 227-230.
- [63] W.Q. Song, P. Beggs, M. Easton, Compressive strain-rate sensitivity of magnesium-aluminum die casting alloys. *Materials and Design* **30**, 642-648, 2009.
- [64] E.A. Ball, P.B. Prangnell, Tensile-compressive yield asymmetries in high strength wrought magnesium alloys. *Scripta Metall. Mater.* **31**, 111-116, 1994.

- [65] T. Yokoyama, Impact Tensile Stress-strain Characteristics of Wrought Magnesium Alloys. *Strain* **39**, 167-175, 2003.
- [66] G.E. Dieter, *Mechanical Metallurgy*, McGraw-Hill, Boston, USA, 1986.
- [67] S. Begum, D.L. Chen, S. Xu, A.A. Luo, Effect of strain ratio and strain rate on low cycle fatigue behavior of AZ31 wrought magnesium alloy. *Mater. Sci. Eng. A* **517**, 334-343, 2009.
- [68] S. Begum, D.L. Chen, S. Xu, A.A. Luo, Low cycle fatigue properties of an extruded AZ31 magnesium alloy. *Int. J. Fatigue* **31**, 726-735, 2009.
- [69] X.Z. Lin, D.L. Chen, Strain controlled cyclic deformation behavior of an extruded magnesium alloy. *Mater. Sci. Eng. A* **496**, 106-113, 2008.
- [70] D.W. Brown, A. Jain, S.R. Agnew, B. Clausen, Twinning and detwinning during cyclic deformation of Mg alloy AZ31B. *Mater. Sci. Forum* **539-543**, 3407-3413, 2007.
- [71] U. Noster, B. Scholtes, Isothermal strain-controlled quasi-static and cyclic deformation behavior of magnesium wrought alloy AZ31. *Mater. Res. Adv. Tech. (Zeitschrift fuer Metallkunde)* **94**, 559-563, 2003.
- [72] S. Hasegawa, Y. Tsuchida, H. Yano, M. Matsui, Evaluation of low cycle fatigue life in AZ31 magnesium alloy. *Int. J. Fatigue* **29**, 1839-1845, 2007.
- [73] S. Begum, D.L. Chen, S. Xu, A.A. Luo, Strain-controlled low-cycle fatigue properties of a newly developed extruded magnesium alloy. *Metall. Mat. Trans. A* **39**, 3014-3026, 2008.

- [74] C.L. Fan, D.L. Chen, A.A. Luo, Dependence of the distribution of deformation twins on strain amplitudes in an extruded magnesium alloy after cyclic deformation. *Mater. Sci. Eng. A* **519**, 38-45, 2009.
- [75] L. Wu, A. Jain, D.W. Brown. G.M. Stoica, S.R. Agnew, B. Clausen, D.E. Fielden, P.K. Liaw, Twinning-detwinning behavior during the strain-controlled low-cycle fatigue testing of a wrought magnesium alloy, ZK60A. *Acta Mater.* **56**, 688-695, 2008.
- [76] L. Wu, S.R. Agnew, D.W. Brown. G.M. Stoica, B. Clausen, A. Jain, D.E. Fielden, P.K. Liaw, Internal stress relaxation and load redistribution during the twinning-detwinning-dominated cyclic deformation of a wrought magnesium alloy, ZK60A. *Acta Mater.* **56**, 3699-3707, 2008.
- [77] H. El Kadiri, Y. Xue, M.F. Horstemeyer, J.B. Jordon, P.T. Wang, Identification and modeling of fatigue crack growth mechanisms in a die-cast AM50 magnesium alloy. *Acta Mater.* **54**, 5061-5076, 2006.
- [78] Z. Liu, Z.G. Wang, Y. Wang, Z.Y. Liu, Cyclic deformation behavior of high pressure die casting alloy AM50. *J. Mater. Sci. Lett.* **18**, 1567-1569, 1999.
- [79] P. Cavaliere, P.P. De Marco, Fatigue behaviour of friction stir processed AZ91 magnesium alloy produced by high pressure die casting. *Mater. Charact.* **58**, 226-232, 2007.
- [80] Y. Uematsu, K. Tokaji, K. Fujiwara, Y. Tozaki, H. Shibata, Fatigue behaviour of cast magnesium alloy AZ91 microstructurally modified by friction stir processing. *Fatigue Fract. Engng. Mater. Struct.* **32**, 541-551, 2009.

- [81] S.N. Perov, V.V. Ogarevic, R.I. Stephens, Application and verification of fatigue life calculation methods for AZ91E-T6 cast magnesium alloy under variable amplitude loading. *J. Eng. Mater. Technol. Trans. ASME* **115**, 385-390, 1993.
- [82] N. Llorca, A. Bloyce, T.M. Yue, Fatigue behaviour of short alumina fibre reinforced AZ91 magnesium alloy metal matrix composite. *Mater. Sci. Eng. A* **135**, 247-252, 1991.
- [83] K. Gall, G. Biallas, H.J. Maier, P. Gullett, M.F. Horstemeyer, D.L. McDowell, In-Situ Observations of Low-Cycle Fatigue Damage in Cast AM60B Magnesium in an Environmental Scanning Electron Microscope. *Metall. Mat. Trans. A* **35**, 321-331, 2004.
- [84] K. Gall, G. Biallas, H.J. Maier, P. Gullett, M.F. Horstemeyer, D.L. McDowell, J. Fan, In-situ observations of high cycle fatigue mechanisms in cast AM60B magnesium in vacuum and water vapor environments. *Int. J. Fatigue* **26**, 59-70, 2004.
- [85] K. Gall, G. Biallas, H.J. Maier, M.F. Horstemeyer, D.L. McDowell, Environmentally influenced microstructurally small fatigue crack growth in cast magnesium. *Mater. Sci. Eng. A* **396**, 143-154, 2005.
- [86] H.T. Kang, T. Ostrom, Mechanical behavior of cast and forged magnesium alloys and their microstructures. *Mater. Sci. Eng. A* **490**, 52-56, 2008.
- [87] D.L. Goodenberger, R.I. Stephens, Fatigue of AZ91E-T6 cast magnesium alloy. *J. Eng. Mater. Technol. Trans. ASME* **115**, 391-397, 1993.
- [88] S. Xu, X. Zeng, Z. Gao, H. Chen, J. Fan, Experimental and theoretical study of the cyclic relaxation of die cast magnesium alloy. *Mater. Sci. Forum* **610-613**, 991-998, 2009.

- [89] C.H. Caceres, T. Sumitomo, M. Veidt, Pseudoelastic behaviour of cast magnesium AZ91 alloy under cyclic loading-unloading. *Acta Mater.* **51**, 6211-6218, 2003.
- [90] Z. Fan, Semisolid metal processing. *International Materials Reviews* **47**, 49-86, 2002.
- [91] Z. Fan, G. Liu, Y. Wang, Microstructure and mechanical properties of rheo-diecast AZ91D magnesium alloy. *J. Mater. Sci.* **41**, 3631-3644, 2006.
- [92] A.K. Dahle, Y.C. Lee, M.D. Nave, P.L. Schaffer, D.H. StJohn, Development of the as-cast microstructure in magnesium–aluminium alloys. *J. Light Metals* **1**, 61-72, 2001.
- [93] L. Wang, B. Zhang, S. Zhu, M. Zhang, C. Zhang, S. Guan, Effects of silicocalcium on microstructure and properties of Mg-6Al-0.5Mn alloy. *Trans. Nonferrous Met. Soc. China (English Ed.)* **16**, 551-555, 2006.
- [94] I.J. Polmear, Light Alloys, Chapman and Hall, London, 1989.
- [95] X.W. Li, M.X. Lu, A.X. Sha, L.Zhang, The tensile deformation behavior of Ti-3Al-4.5V-5Mo titanium alloy. *Mater. Sci. Eng. A* **490**, 193-197, 2008.
- [96] X. Wang, H. Hamasaki, M. Yamamura, R. Yamauchi, T. Maeda, Y. Shirai, F. Yoshida, Yield-point phenomena of Ti-20V-4Al-1Sn at 1073 K and its constitutive modelling. *Mater. Trans.* **50**, 1576-1578, 2009.
- [97] O. Nijs, B. Holmedal, J. Friis, E. Nes, Sub-structure strengthening and work hardening of an ultra-fine grained aluminium-magnesium alloy. *Mater. Sci. Eng. A* **483-484**, 51-53, 2008.
- [98] A.H. Cottrell, B.A. Bilby, Dislocation theory of yielding and strain ageing of iron. *Proceedings of the Physical Society, Section A* **62**, 49-62, 1949.

- [99] W.G. Johnston, J.J. Gilman, Dislocation velocities, dislocation densities and plastic flow in lithium fluoride crystals. *J. Appl. Phys.* **30**, 129-144, 1959.
- [100] P. Gondi, R. Tognato, Dislocation damping and yielding phenomena in Cd alloyed Zinc. *Scr. Metall.* **7**, 721-725, 1973.
- [101] R. Mahmudi, Yield point phenomenon in ultrafine-grained aluminium sheets. *Mater. Lett.* **19**, 243-246, 1994.
- [102] L. Zhang, Z.Y. Cao, Y.B. Liu, G.H. Su, L.R. Cheng, Effect of Al content on the microstructures and mechanical properties of Mg-Al alloys. *Mater. Sci. Eng. A* **508**, 129-133, 2009.
- [103] U.F. Kocks, H. Mecking, Physics and phenomenology of strain hardening: The FCC case. *Progress in Materials Science* **48**, 2003.
- [104] D. Kuhlmann-Wilsdorf, N. Hansen, Theory of work-hardening applied to stages III and IV. *Metall. Trans. A* **20**, 2393-2397, 1989.
- [105] J.W. Choi, K.S. Shin, Development of high performance magnesium alloys via microstructure and texture control, *Mat. Sci. Forum* **618-619** 249-252, 2009.
- [106] C. Yan, W. Ma, V. Burg, M.W. Chen, Experimental and numerical investigation on ductile-brittle fracture transition in a magnesium alloy. *J. Mater. Sci.* **42**, 7702-7707, 2007.
- [107] H. Hu, M. Zhou, Z. Sun, N. Li, Tensile behaviour and fracture characteristics of die cast magnesium alloy AM50. *J. Mater. Process. Technol.* **201**, 364-368, 2008.
- [108] M. Valsan, P. Parameswaran, K.B. Rao, M. Vijayalakshmi, S.L. Mannan, D.H. Shastri, High-temperature low-cycle fatigue behavior of a NIMONIC PE-16

- superalloy - correlation with deformation and fracture. *Metal. Trans. A* **23**, 1751-1761, 1992.
- [109] S. Xu, V.Y. Gertsman, J. Li, J.P. Thomson, M. Sahoo, Role of mechanical twinning in tensile compressive yield asymmetry of die cast Mg alloys. *Can. Metall. Q.* **44**, 155-166, 2005.
- [110] H. Zenner, F. Renner, Cyclic material behaviour of magnesium die castings and extrusions. *Int. J. Fatigue* **24**, 1255-1260, 2002.
- [111] G.E. Mann, T. Sumitomo, C.H. Caceres, J.R. Griffiths, Reversible plastic strain during cyclic loading-unloading of Mg and Mg-Zn alloys. *Mater. Sci. Eng. A* **456**, 138-146, 2007.
- [112] S.G. Hong, S.H. Park, Y.H. Huh, C.S. Lee, Anisotropic fatigue behavior of rolled Mg-3Al-1Zn alloy. *J. Mater. Res.* **25**, 966-971, 2010.
- [113] S.R. Agnew, O. Duygulu, Plastic anisotropy and the role of non-basal slip in magnesium alloy AZ31B. *Int. J. Plasticity* **21**, 1161-1193, 2005.
- [114] R.E. Reed-Hill, R. Abbaschian, *Physical Metallurgy Principles*, PWS Publ. Co., Boston, 1994.
- [115] S.H. Park, S. Hong, C.S. Lee, Activation mode dependent  $\{10\bar{1}2\}$  twinning characteristics in a polycrystalline magnesium alloy. *Scr. Mater.* **62**, 202-205, 2010.
- [116] J. Koike, Enhanced deformation mechanisms by anisotropic plasticity in polycrystalline Mg alloys at room temperature. *Metall. Mat. Trans. A* **36**, 1689-1696, 2005.
- [117] B.F. Gerard, Anisotropy and voiding at high strain rates in a mg alloy extrudate. *Adv. Mater. Process.* **168**, 32-33, 2010.



- [118] S. Suresh, *Fatigue of Materials*, 2<sup>nd</sup> Ed., Cambridge University Press, Cambridge, UK, 1998.
- [119] F. Czerwinski, P.J. Pinet, J. Overbeeke, The influence of primary solid content on the tensile properties of a thixomolded AZ91D magnesium alloy, *In: N. Hryn, Magnesium Technology 2001, TMS*, New Orleans, Louisiana, United States, Feb. 11-15, 2001, pp. 99-102.

## HIMESH PATEL

<b>EDUCATION</b>	Master of Applied Science (Aug. 2010) Ryerson University, Toronto, ON, Canada Major: Mechanical Engineering, GPA: 4.2/4.33  Bachelor of Engineering (Mar. 2006) Sardar Vallabhbhai National Institute of Technology (SVNIT), India. Major: Mechanical Engineering
<b>EXPERIENCE</b>	Teaching Assistant, Sep. 2008 – Aug. 2010 Ryerson University, Toronto, ON, Canada  Sr. Mechanical Engineer, Mar. 2001- June, 2007 Larsen & Toubro Ltd., Surat, Gujarat, India
<b>AWARDS</b>	Ontario Graduate Scholarship - OGS, 2010-2011 Ryerson Graduate Scholarship for academic excellence, 2009-2010

### LIST OF PUBLICATIONS (over the past two years during my MASc. study)

#### A. Refereed journal papers (accepted or under review):

1. **H.A. Patel**, D.L. Chen, S.D. Bhole, K. Sadayappan, Microstructure and tensile properties of thixomolded magnesium alloys, *Journal of Alloys and Compounds*, 496, 2010, 140-148.
2. **H.A. Patel**, D.L. Chen, S.D. Bhole, K. Sadayappan, Cyclic deformation and twinning in a semi-solid processed AZ91D magnesium alloy, submitted to *Material Science & Engineering A*, 2010, Ref. No.: MSEA-D-10-01406 (under revision).
3. **H.A. Patel**, N. Rashidi, D.L. Chen, S.D. Bhole, A.A. Luo, Cyclic deformation behavior of super-vacuum die cast alloy AM60B at different strain ratios, submitted to *Journal of Alloys and Compounds*, 2010, Ref. No.: JAC-D-10-03354 (under revision).
4. **H.A. Patel**, D.L. Chen, S.D. Bhole, K. Sadayappan, Low cycle fatigue behavior of a semi-solid processed magnesium alloy AM60B, submitted to *Fatigue & Fracture of Engineering Materials & Structures*, 2010, Ref. No.: FFEMS-4625 (under review).
5. H. Elhadari, **H.A. Patel**, D.L. Chen, W. Kasprzak, Tensile and cyclic deformation behavior of cast aluminum alloys for automotive applications (under review of CANMET researcher).
6. **H.A. Patel**, D.L. Chen, S.D. Bhole, K. Sadayappan, Effect of heat treatment on the tensile and fatigue behavior of a semi-solid processed AM60B magnesium alloy (under preparation).

#### B. Conference presentations:

1. C.L. Fan, **H.A. Patel**, S.M. Chowdhury, D.L. Chen, Cyclic deformation of magnesium alloys, APMA-AUTO21 Annual Conference and Exhibition, Hamilton, Ontario, May 26-28, 2009 (Poster Presentation at AUTO21 conference).
2. **H.A. Patel**, S.M. Chowdhury, C.Y. Zang, D.L. Chen, S.D. Bhole, Fatigue and reliability of magnesium alloys, APMA-AUTO21 Annual Conference and Exhibition, Windsor, Ontario, Canada, June 7-10, 2010 (Poster Presentation at AUTO21 conference).
3. **H.A. Patel**, D.L. Chen, S.D. Bhole, K. Sadayappan, Fatigue performance of a thixomolded AM60B magnesium alloy, The 22nd Canadian Material Science Conference, Waterloo, Ontario, Canada, June 8-11, 2010 (Poster Presentation at CMSC conference).
4. J. Jordon, M. Horstemeyer, **H. Patel**, D. Chen, S. Bhole, B. Behraves, H. Jahed, S. Lambert, X. Su, Monotonic and Fatigue Behavior of Mg AZ31 in Friction Stir Spot Welds: An International Benchmark Test in the "Magnesium Front End Research and Development" Project, 2011 TMS Annual meeting & Exhibition, Magnesium Technology 2011, Abstract accepted by review committee of the symposium Magnesium Technology 2011.